Analysis of Infinite Arrays of Arbitrarily Shaped Planar Radiating Elements Using a Floquet Mode Based Method of Moments Approach

by

James William LaPean, Jr.

Dissertation submitted to the Faculty of the Virginia Polytechnic Institute and State University in partial fulfillment of the requirements for the degree of

Doctor of Philosophy
in
Electrical Engineering

APPROVED:

Dr. Warren L. Stutzman, Co-advisor

Dr. William A. Davis, Co-advisor

Dr. Tim Pratt

Dr. Ahmad Safaai-Jazi

Dr. Lee W. Johnson

April 29, 1996
Blacksburg, Virginia

Keywords: Antennas, Arrays, Scanning, Radar, Communications

ANALYSIS OF INFINITE ARRAYS OF ARBITRARILY SHAPED PLANAR RADIATING ELEMENTS USING A FLOQUET MODE BASED METHOD OF MOMENTS APPROACH

by

James William LaPean, Jr.

Dr. Warren L. Stutzman, Co-advisor
Dr. William A. Davis, Co-advisor

Bradley Department of Electrical Engineering

Large phased array antennas are theoretically capable of delivering the directive gain of similarly sized aperture antennas while offering electronic beam scanning capabilities and greater operational flexibility. Unfortunately, the high cost associated with large phased antenna arrays has limited their use to highly specialized applications where no other antenna system configuration is possible. The recent development of less expensive microwave active devices has led to a renewed interest in large phased antenna arrays. These devices allow the amplification and signal processing required in phased antenna arrays to be distributed among many identical modules which combine the amplification, feed network, and radiating element sections of traditional antenna arrays. These modules can then be produced at a lower unit cost and result in an antenna system which is more easily integrated and repaired.

The practicality of large phased antenna arrays is still limited by the great difficulty experienced in predicting their performance. Mutual coupling effects between the radiating elements produce significant variations from ideal array theory. The prediction and reduction of these effects requires a characterization approach which is computational rather than experimental. This document presents a new approach which allows the characterization of arbitrarily shaped planar radiating elements printed on a dielectric

support slab backed by a perfect electric conductor ground plane. This analysis approach uses a Method of Moments technique to determine the electric current distribution over a set of bi-triangular sub-domain elements describing a single radiating element. The effects of mutual coupling in the fully active infinite antenna array are included in the analysis by a Floquet mode based Green's function used in the Method of Moments analysis. This characterization technique has been implemented in the computational electromagnetics code ASIA (Analysis Software for Infinite Arrays). The analysis approach presented here is validated by comparison with published input impedance data for two different radiating elements. Finally, preliminary analysis results are shown for a more complex radiating element.

For my parents, Linda Joyce LaPean and James William LaPean, Sr.,

and my sister Amber Denise Kidd.

ACKNOWLEDGMENT

I would like to express my appreciation for the guidance and moral support given me throughout my research in graduate school by my advisor Dr. Warren L. Stutzman. Graduate school would have been a great deal more difficult without the experience and wisdom he provided. I would also like to thank my co-advisor Dr. William A. Davis for his guidance, support, and patience in the preparation of my doctoral research. I have learned a great deal from his deep understanding of electromagnetics. Acknowledgment is due my entire committee for the helpful comments they provided resulting in better research and this document.

I would like to thank my fellow graduate students Gerry Ricciardi and Mike Barts for their friendship and willingness to listen to and discuss explanations of some of the more difficult concepts of this research. Matt Monkevich for the operation of the ASIA code for the research into new radiating elements which provided the support without which this research could not have been performed. Finally, I would like to thank Andrew Predoehl for his assistance with many computer related implementation issues.

The research presented here was supported by reseach funding provided by ITT Gilfillan.

TABLE OF CONTENTS

LIST OF FIGURES

LIST OF TABLES

1. INTRODUCTION

Phased antenna arrays offer communications and remote sensing system designers many potential advantages over aperture antennas of comparable size. Large phased antenna arrays can perform electronic beam steering, aperture reconfiguration, and sophisticated shared-use aperture operation while retaining the high gain commonly associated with reflector antennas. Unfortunately, large phased antenna arrays have been prohibitively expensive for most non-military applications until the recent development of high performance/low cost microwave active devices for amplification, filtering, and phase shifting. The development of these devices will lower the cost of large antenna arrays and increased the realizability of the potential advantages antenna arrays by making distributed amplification and signal processing much more practical. Antenna arrays designed using distributed architecture can be constructed from a large number of identical, self-contained modules which combine the duties of the final amplifier, feed network, and radiating element in traditional antenna arrays. The cost reduction and increased flexibility of operation realized from the use of mass produced array modules has the potential to expand the range of practical applications for phased antenna arrays greatly. This exciting development offers a great challenge to antenna engineering because the many possible applications of large phase antenna arrays large instantaneous bandwidths and electronically selected polarizations while state of the art phased antenna arrays are either limited to a narrow frequency band or are designed to operate at a few spot frequencies.

1.1 Research Motivation

The Antenna Laboratory at Virginia Tech became aware of the increasing interest in the design and operation of large phased antenna arrays during the winter of 1994. Preliminary investigations of design of large phased antenna arrays subsequently led to research contracts for the analysis and design of broadband, dual polarized radiating elements for a multi-functional antenna array. The full antenna array was to be in the 1000 element class and provide arbitrary, orthogonal, dual-linear polarization over the X- and Ku-bands. Discussions with the sponsor determined that a printed radiating element design was highly desirable because printed radiating elements can be made to be highly rugged as well as the advantages discussed above. A study of possible radiating elements for this array found that no existing radiating element could provide the necessary performance.

While an empirical approach to the design of radiating elements is possible, the demanding performance requirements for this antenna made this option infeasible. The complex nature of the resulting antenna array makes the construction of large segments of the array for test purposes extremely difficult. Also, determining the performance of the full antenna array from a small segment of the antenna array is generally not practical. Clearly, the design of this radiating element required the use of an analysis tool which would eliminate the need to construct test articles at step in the design process. While simple ideal antenna array theory is commonly used in preliminary computations, it does not predict the performance of radiating elements in large phased antenna arrays. The presence of mutual coupling between the elements in these arrays causes the radiating element performance to vary significantly from the performance of the radiating element in isolation. Furthermore, the effects of mutual coupling may be extremely fast varying as a

function of beam scanning angle and can produce blind spots into which the array cannot be beam scanned.

These difficulties demanded that a computational electromagnetics (CEM) analysis tool which could characterize the performance of an arbitrarily shaped, planar printed radiating element in the fully active antenna array environment was needed. Commonly available CEM analysis packages, such as NEC and ESP, are not capable of analyzing printed radiating elements in the array environment because the dielectric substrate is not adequately modeled and hardware limitations on the number of electric current unknowns limit the analysis to small segments of the array. Layered media CEM tools, such as SONNET and IE3D, model the dielectric substrate well but are still limited by the number of unknowns available. Fortunately, an approach to the analysis of periodic structures can be formulated using Floquet's theorem [1] to evaluate a single cell of the periodicity rather than the entire structure. Essentially, Floquet's theorem is used to expand the electric current, voltage, and electromagnetic fields in the periodic cell to enforce a constant phase taper across the cell. For antenna array analysis, this phase taper is equal to the phase taper required for the desired beam scanning as determined from ideal array theory. This approach to the analysis of periodic structures requires that the structure be of infinite extent. Research and measurement experience in the literature indicates that large antenna arrays can be adequately modeled as infinite antenna arrays if the large antenna array contains on the order of 100 elements or more [2, 3].

1.2 Organization of the Dissertation

This document describes an infinite antenna array based technique for the characterization of complex planar radiating elements in large antenna arrays This analysis

approach uses a Method of Moments analysis to find the electric current distribution over a set of perfect electric conductor bi-triangular sub-elements which describe the radiating element. This choice of radiating element description allows the analysis of an arbitrarily shaped, planar radiating element. The Green's function used in the Method of Moments analysis is embedded in a Floquet series expansion of the electromagnetic fields in the analysis cell. The Floquet series expansion automatically includes the mutual coupling effects of the fully active, infinite antenna array in the characterization of the single radiating element in the analysis cell including the active input impedance, input power, and aperture efficiency of the arbitrary planar radiating element. The computational electromagnetics code ASIA (Analysis Software for Infinite Arrays) has been developed in the Antenna Laboratory at Virginia Polytechnic Institute and State University using this technique. The ASIA code is unique because it has been designed to allow user-specification of the analysis cell and radiating element geometry through input text files rather than program recompilation.

Chapter 2 of this document presents background information which is necessary to allow the development of the analysis approach and reviews approaches which are currently used to analyze antenna arrays. The development of the new characterization technique for radiating elements in fully active, infinite antenna arrays is presented in Chapter 3. Chapter 4 presents computational results from the ASIA implementation of the new analysis approach including a study of the convergence of the analysis algorithm and validation test cases for the analysis algorithm. The computational results in Chapter 4 conclude with preliminary results for a more complex printed antenna being studied as a possible wideband, dual-polarized radiating element for large phased antenna arrays.

2. ARRAY ANALYSIS BACKGROUND

An antenna array is a collection of several antennas arranged in space and excited together to produce an electromagnetic field which usually cannot be produced by a single antenna [4]. The individual antennas in this antenna array are commonly referred to as radiating elements of the array and may be very simple or quite complex. While the performance of the antenna array can easily be computed for the ideal case when these radiating elements do not interact, the prediction of the behavior of a complete, realizable antenna array is not at all trivial. As mentioned in Chapter 1, this ability to predict the behavior is necessary to allow the construction of even moderate performance antenna arrays. The alternate approach of building and testing many versions of the antenna array would afford only a limited understanding of the electromagnetic effects which affect the behavior and is not palatable due to cost considerations alone. This chapter begins with a discussion of the basic antenna array concepts which are necessary to understand the theory of the analysis approach developed in Chapter 3. The second portion of this chapter presents an overview of existing techniques which allow the characterization of large antenna arrays.

2.1 Basic Antenna Array Concepts

This section will present fundamental antenna array concepts which are required for the theoretical development of Chapter 3. Section 2.1.1 presents a development of the pattern of an antenna array and introduces the concept of pattern multiplication. Section 2.1.1 also develops the requirements for beam scanning in a linear antenna array with uniform spacing. Section 2.1.2 discusses the undesirable effects on antenna array

performance which are present in non-ideal arrays. The presentation in Section 2.1.2 begins with mutual coupling between the radiating elements in antenna arrays and introduces the concept of the active element pattern. Surface waves, a major source of mutual coupling in antenna arrays printed on dielectric substrates, are also discussed in Section 2.1.2. This discussion concludes with the introduction of the concept of infinite array analysis in Section 2.1.3. The applicability of infinite array analysis to large antenna arrays is also discussed in Section 2.1.3.

2.1.1 Principles of Ideal Arrays

The vector magnetic potential, $\overline{A}(\overline{r})$, of an arbitrarily shaped antenna array of N arbitrary sources is given by

$$\overline{A}(\overline{r}) = \int\int\int \sum_{n=1}^{N} \overline{J}_{el_n}(\overline{r}') \frac{e^{-jk_o|\overline{r}-\overline{r}'|}}{4\pi|\overline{r}-\overline{r}'|} dv' \tag{2.1}$$

where $\overline{J}_{el_n}(\overline{r}')$ is the electric current density distribution of the n^{th} radiating element in the array and $\overline{r}$ is the vector from the origin to the observation point. The electric field of this antenna array can be found from

$$\overline{E}(\overline{r}) = \frac{1}{j\omega\epsilon}\left(\nabla \times \overline{H}(\overline{r}) - \sum_{n=1}^{N} \overline{J}_{el_n}(\overline{r})\right) = \frac{1}{j\omega\epsilon}\left(\nabla \times \nabla \times \overline{A}(\overline{r}) - \sum_{n=1}^{N} \overline{J}_{el_n}(\overline{r})\right). \tag{2.2}$$

Substituting (2.1) into (2.2) gives

$$\overline{E}(\overline{r}) = \frac{1}{j\omega\epsilon}\left(\nabla \times \nabla \times \int\int\int \sum_{n=1}^{N} \overline{J}_{el_n}(\overline{r}') \frac{e^{-jk_o|\overline{r}-\overline{r}'|}}{4\pi|\overline{r}-\overline{r}'|} dv' - \sum_{n=1}^{N} \overline{J}_{el_n}(\overline{r})\right) \tag{2.3}$$

which simplifies to

$$\overline{E}(\overline{r}) = \frac{1}{j\omega\epsilon}\nabla \times \nabla \times \int\int\int \sum_{n=1}^{N} \overline{J}_{el_n}(\overline{r}') \frac{e^{-jk_o|\overline{r}-\overline{r}'|}}{4\pi|\overline{r}-\overline{r}'|} dv' \tag{2.4}$$

for the source-free region. By superposition, (2.4) can be rewritten as the sum of the electric fields from each of the N radiating elements which gives

$$\overline{E}(\overline{r}) = \sum_{n=1}^{N} \left(\frac{1}{j\omega\epsilon}\nabla \times \nabla \times \int\int\int \overline{J}_{el_n}(\overline{r}') \frac{e^{-jk_o|\overline{r}-\overline{r}'|}}{4\pi|\overline{r}-\overline{r}'|} dv' \right). \tag{2.5}$$

In the far-field of the array , this expression for the electric field may be simplified to

$$\overline{E}(\overline{r}) = \sum_{n=1}^{N} \left(\frac{1}{j\omega\epsilon}\hat{r} \times \hat{r} \times \int\int\int \overline{J}_{el_n}(\overline{r}') \frac{e^{-jk_o|\overline{r}-\overline{r}'|}}{4\pi|\overline{r}|} dv' \right). \tag{2.6}$$

where $|\overline{r}-\overline{r}'| \approx |\overline{r}|$. For an antenna array of N arbitrary sources which are identical except for electric current density amplitude, (2.5) may be written as

$$\overline{E}(\overline{r}) = \frac{e^{-jk_o|\overline{r}|}}{j\omega\epsilon 4\pi|\overline{r}|} \left(\hat{r} \times \hat{r} \times \int\int\int \overline{j}_{el}(\overline{r}') e^{jk_o\hat{r}\cdot\overline{r}'} dv' \right) \left(\sum_{n=1}^{N} J_{el_n} e^{jk_o\hat{r}\cdot\overline{r}_n} \right) \tag{2.7}$$

where

$$\overline{J}_{el_n}(\overline{r}') = J_{el_n}\overline{j}_{el}(\overline{r}') \tag{2.8}$$

$\overline{r}_n$ is the vector to a reference location on the $n^{\underline{th}}$ radiating element and the integral for the vector magnetic potential of the radiating element normalized electric current distribution, $\overline{j}_{el}(\overline{r}')$, is performed with the reference location of the radiating element at the coordinate system origin.

The unnormalized radiation pattern is given by

$$F(\theta,\phi) = \left| \left(\hat{r} \times \hat{r} \times \int\int\int \overline{j}_{el}(\overline{r}') e^{jk_o\hat{r}\cdot\overline{r}'} dv' \right) \left(\sum_{n=1}^{N} J_{el_n} e^{jk_o\hat{r}\cdot\overline{r}_n} \right) \right| \tag{2.9}$$

which is the final two terms of (2.8) containing only the angular dependence of the

electromagnetic fields. The unnormalized radiation pattern can be factored as

$$F(\theta,\phi) = EP(\theta,\phi)AF(\theta,\phi) \tag{2.10}$$

where

$$EP(\theta,\phi) = \left|\left(\hat{r}\times\hat{r}\times\int\int\int \bar{j}_{el}(\bar{r}')\mathrm{e}^{jk_o\hat{r}\cdot\bar{r}'}\,\mathrm{d}v'\right)\right|, \tag{2.11a}$$

and

$$AF(\theta,\phi) = \left|\left(\sum_{n=1}^{N} J_{el_n}\mathrm{e}^{jk_o\hat{r}\cdot\bar{r}_n}\right)\right|. \tag{2.11b}$$

The term $EP(\theta,\phi)$ in (2.10) is the far-field pattern of an isolated element of the antenna array. The $AF(\theta,\phi)$, or array factor, term in (2.10) is the far-field pattern of the antenna array geometry if the radiating elements are isotropic radiators. The far-field pattern of the array is then the product of the patterns of the radiating element and the array geometry. This ability of the far-field pattern of the antenna array to be factored in this form allows the pattern to be calculated from the element pattern and the array factor by pattern multiplication.

The requirement for beam scanning in ideal antenna arrays can be illustrated using a simple linear array with equally spaced elements. Figure 2.1 shows the geometry of an equally spaced linear array of identical arbitrary elements located along the z-axis. The angular dependence of the array factor is

$$AF(\theta) = J_{el_1}\mathrm{e}^{-jk_o\frac{3s}{2}\cos\theta} + J_{el_2}\mathrm{e}^{-jk_o\frac{s}{2}\cos\theta} + J_{el_3}\mathrm{e}^{jk_o\frac{s}{2}\cos\theta} + J_{el_4}\mathrm{e}^{jk_o\frac{3s}{2}\cos\theta} \tag{2.12}$$

where J_{el_1} through J_{el_4} are the complex amplitudes of the electric current densities on the radiating elements, the interelement spacing of the array is s, and the exponential phase terms are referenced to the center of the array. The complex weight of the $n^{\underline{th}}$ element

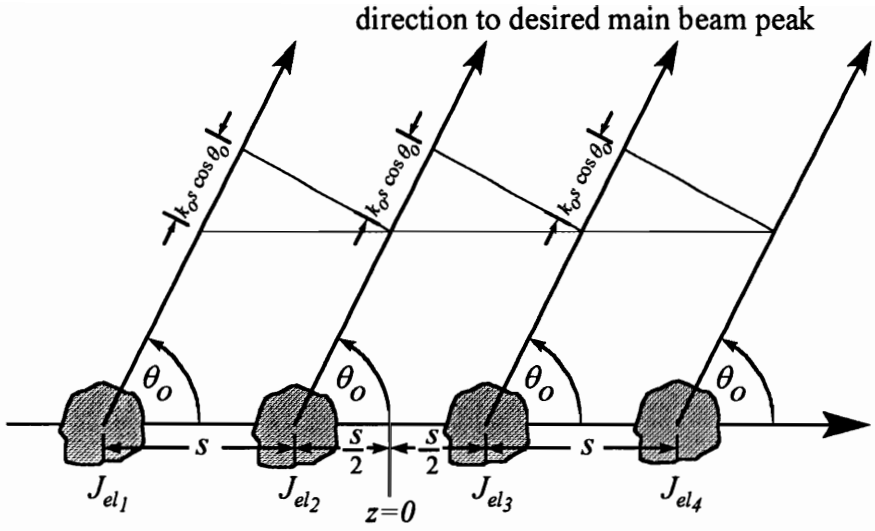

Figure 2.1. Linear array geometry showing the identical arbitrary array elements, the interelement spacing of the array, s, and the angle of scan of the array, θ_o.

can be rewritten as

$$J_{el_n} = |J_{el_n}|e^{j\alpha_n} \tag{2.13}$$

where α_n is the phase angle of the complex weight. Substituting (2.13) into (2.12) gives

$$\begin{aligned} AF(\theta) = {} & |J_{el_1}|e^{j(\alpha_1 - k_o \frac{3s}{2}\cos\theta)} + |J_{el_2}|e^{j(\alpha_2 - k_o \frac{s}{2}\cos\theta)} + \\ & |J_{el_3}|e^{j(\alpha_3 + k_o \frac{s}{2}\cos\theta)} + |J_{el_4}|e^{j(\alpha_4 + k_o \frac{3s}{2}\cos\theta)}. \end{aligned} \tag{2.14}$$

To produce a main beam peak, total constructive interference, in the θ_o direction the arguments in the exponential terms must have the relationship

$$\begin{aligned} \left(\alpha_1 - k_o \frac{3s}{2}\cos\theta_o\right) = \left(\alpha_2 - k_o \frac{s}{2}\cos\theta_o\right) \pm 2\pi m = \\ \left(\alpha_3 + k_o \frac{s}{2}\cos\theta_o\right) \pm 2\pi n = \left(\alpha_4 + k_o \frac{3s}{2}\cos\theta_o\right) \pm 2\pi p \end{aligned} \tag{2.15}$$

where m, n, and p are real integers and are usually zero. It is now apparent that the phase terms α_1 through α_4 can be replaced by $(n-1)\alpha$ because the interelement phase shift

must be uniform for total constructive interference when the antenna array is equally spaced. Making this substitution and setting the 2π phase terms to zero gives

$$\left(-k_o\frac{3s}{2}\cos\theta_o\right) = \left(\alpha - k_o\frac{s}{2}\cos\theta_o\right) = \left(2\alpha + k_o\frac{s}{2}\cos\theta_o\right) = \left(3\alpha + k_o\frac{3s}{2}\cos\theta_o\right) \tag{2.16}$$

which can be solved for interelement phase shift for a main beam scan direction of θ_o of

$$\alpha = -k_o s\cos\theta_o. \tag{2.17}$$

Substituting this value for the phase shift between the elements of the antenna array for a main beam peak in the θ_o direction into (2.15) gives

$$AF(\theta) = |J_1|e^{-jk_o\frac{3s}{2}\cos\theta} + |J_2|e^{-j(k_o s\cos\theta_o + k_o\frac{s}{2}\cos\theta)} + |J_3|e^{-j(2k_o s\cos\theta_o - k_o\frac{s}{2}\cos\theta)} + |J_4|e^{-j(3k_o s\cos\theta_o - k_o\frac{3s}{2}\cos\theta)}. \tag{2.18}$$

If the contributions of all of the radiating elements of the antenna array are in phase for any angle θ other than the angle of the intended main beam, θ_o, this angle is called the grating lobe direction and the lobe of the antenna pattern in that direction is called a grating lobe. For an equally spaced linear array with an interelement spacing of s, the grating lobe is formed fully in the directions which satisfy

$$-k_o\frac{3s}{2}\cos\theta_{gl} = -k_o\left(s\cos\theta_o + \frac{s}{2}\cos\theta_{gl}\right) \pm 2\pi m \tag{2.19}$$

or

$$\theta_{gl} = \operatorname{acos}\left(\cos\theta_o \pm \frac{m\lambda_o}{s}\right) \tag{2.20}$$

where θ_{gl} is in real space.

2.1.2 Non-ideal Arrays

The antenna array analysis approach used in the previous section assumed that the performance of each of the radiating elements was unaffected by the presence of the other radiating elements. This assumption allows the analysis of the behavior of the antenna array to be based on the radiating element input impedance and far-field antenna pattern for an isolated element. Excluding oddities such as radio astronomy antenna arrays of parabolic reflector antennas, the performance of most practical antenna arrays is significantly altered by the coupling of energy between the radiating elements. The coupled energy can alter both the input impedance and the radiated field strength of the radiating element in the antenna array. These effects are generally detrimental to the proper operation of the antenna array and are of extreme significance in phased array antennas because the coupling varies greatly with the relative phase between the radiating elements.

The most significant two effects of the mutual coupling between the radiating elements of the antenna array are the appearance of blind angles to which the main beam of the antenna array cannot be scanned and large, rapid variations in the input impedance of the radiating elements as a function of beam scanning angle. These effects are, in fact, simply different expressions of the same problem. The first possible approach is that the large variation in the active input impedance of the radiating elements of the antenna array near the blind angle of the antenna array cause reflection of the incident power on the elements rather than receiption or transmission. Alternately, the presence of a blind spot prevents the antenna array from receiving or transmitting power in the blind direction.

The effect on array performance of the energy coupled between the radiating elements can be observed by two characterization techniques. The calculation or

measurement of the mutual impedance matrix of the antenna array allows both the input impedance and the radiation performance of the scanned array to be estimated fairly accurately but requires up to N^2 measurement for an N element antenna array. Alternately, the measurement of the active element pattern allows the radiation performance of a large antenna array to be characterized with a single set of pattern measurements but provides only limited information about the input impedance to be expected.

The mutual coupling between the radiating elements of the antenna array can be characterized as either a mutual impedance matrix or a scattering matrix [5]. The mutual impedance matrix expresses the coupling dependence between the radiating elements as

$$\boldsymbol{V} = \boldsymbol{Z}\boldsymbol{I} \tag{2.21}$$

where $\boldsymbol{V}$ is the voltage of the source feeding each radiating element of the array, $\boldsymbol{Z}$ is the mutual impedance matrix, and $\boldsymbol{I}$ is the impressed current on each radiating element at the feed point [4]. The mutual impedance matrix has the form

$$\boldsymbol{Z} = \begin{bmatrix} Z_{11} & Z_{12} & \cdots & Z_{1N} \\ Z_{21} & Z_{22} & \cdots & Z_{2N} \\ \vdots & \vdots & \ddots & \vdots \\ Z_{N1} & Z_{N2} & \cdots & Z_{NN} \end{bmatrix} \tag{2.22}$$

where Z_{mn} is the open circuit voltage at the terminals of the $m^{\underline{th}}$ radiating element due to a unit current on the $n^{\underline{th}}$ radiating element. This gives a relationship for Z_{mn} of

$$Z_{mn} = \left.\frac{V_m}{I_n}\right|_{I_i=0,\, i\neq n}. \tag{2.23}$$

The requirement of $I_i = 0$, $i \neq n$ in (2.23) results from the definition of the measurement of the mutual impedance as the impedance between the $m^{\underline{th}}$ and $n^{\underline{th}}$ radiating elements in isolation. This requirement can be achieved by open circuiting the remaining radiating

elements at the feed points during the measurement. This measurement may be performed for only a pair of elements if the induced currents on the remaining elements are negligible [5]. The possibility that the measurement of the mutual impedance between the $m^{\underline{th}}$ and $n^{\underline{th}}$ radiating elements can be conducted in isolation can greatly simplify the determination of the mutual impedance matrix in a regular array. The mutual coupling for each element spacing and orientation need be measured only once rather than between each of the radiating element pairs with that geometry. The scattering matrix of the antenna array is similar to the mutual impedance matrix but is measured with the other elements terminated in a characteristic impedance [5].

The performance of the antenna array can be estimated once the mutual impedance or scattering matrix is computed from either measured or computational results. The antenna array excitation to be used can be represented in the column vector of the impressed source voltages and the impressed currents on the radiating elements calculated from (2.21). The impressed currents can be used to find the input impedance of each radiating element of the antenna array from

$$Z_{in_n}(\theta_o, \phi_o) = \frac{V_{in_n}(\theta_o, \phi_o)}{I_n(\theta_o, \phi_o)} \tag{2.24}$$

where V_{in_n} is the voltage impressed across the terminals of the radiating element and I_n is the impressed current on the radiating element found from (2.21). The computed impressed currents can also be used as the current weights in the array factor to find the far-field pattern of the antenna array. One of the major limitations on this type of characterization of the antenna array is that it usually assumes that the current distribution on the radiating element is unaffected by the mutual coupling effects.

The active element pattern of an element in the antenna array is the far-field pattern of the radiating element measured when the radiating element is fed by a constant incident power source with the other radiating elements terminated [5]. The impedance of the source and the terminations used at the remaining radiating elements must be the same impedance with which the antenna array will be operated to maintain the same mutual coupling effects as the excited antenna array. This active element pattern directly shows the effect of mutual coupling in the array in the pattern level. The inclusion of the effects of the mutual coupling between the radiating elements of the antenna array is advantageous for two reasons: 1) the active element pattern is the correct element pattern for use in pattern multiplication as discussed in Section 2.1.1, and 2) the magnitude of the active reflection coefficient of the radiating element can be derived from the active element pattern for some classes of radiating elements.

The active input reflection coefficient of the radiating element can be determined as a function of scan angle if the radiating element is part of an equally spaced planar antenna array [5]. This restriction allows the maximum possible gain available from a radiating element in an equally spaced array to be found from

$$g_{max}(\theta_o, \phi_o) = \frac{4\pi A}{\lambda^2}\cos\theta_o = \frac{4\pi ab}{\lambda^2}\cos\theta_o \qquad (2.25)$$

for a rectangular grid array where a and b are the dimensions of the array spacing in the x- and y-directions. The $\cos\theta_o$ factor is the projection of the aperture of the radiating element cell into the (θ_o, ϕ_o) direction. This result, (2.25), is based on the assumption that the antenna array produces no grating lobes in visible space at beam scanning angle (θ, ϕ) and that any losses in the radiating element are negligible. If these assumptions are valid, the active reflection coefficient of the radiating element in the array environment, $\Gamma_a(\theta, \phi)$, can be found from

$$|\Gamma_a(\theta,\phi)| = \sqrt{1 - \frac{g_r(\theta,\phi)\lambda^2}{4\pi ab\cos\theta}} \tag{2.26}$$

where $g_r(\theta,\phi)$ is the measured gain of the active element in the (θ,ϕ) direction [5].

The active element pattern concept for the characterization of antenna arrays contains several assumptions which are often correct but must be considered for each radiating element. First, the pattern multiplication principle can only be applied using the active element pattern and the ideal array factor if the relative current distribution on the radiating element is not a function of beam scanning angle. This assumption has generally been found to be acceptable but will cause errors in the predicted antenna array far-field pattern when the main beam is scanned very close to a null in the active element pattern. These errors are not usually significant because the overall level of the pattern in the blind direction is very low. The second assumption is that the radiating elements are essentially lossless. This assumption is required to use the approach of (2.26) to find the active input reflection coefficient of the radiating element. This assumption is fairly accurate for elements which are not significantly loaded, such as dipoles and monopoles, but is less reliable for dielectrically and especially resistively loaded elements. Finally, the common usage of the active element pattern concept is to measure a typical radiating element which is near the center of the antenna array [5]. The far-field gain pattern of this element is then assumed to be correct for all of the elements of the antenna array, including the radiating elements which are near the edge of the antenna array. This approach is valid for large antenna arrays but requires additional consideration for smaller antenna arrays [6]. It is possible to increase the accuracy of this approach for small antenna arrays by measuring the active element pattern of each of the radiating elements in the antenna array and performing the pattern multiplication explicitly using the form of (2.6) rather than (2.7) [6].

Guided surface wave modes are the most significant source of mutual coupling in the type of antenna arrays which are considered here. The dielectric support structure on which the printed radiating elements rest is capable of supporting surface wave modes which travel in the plane of the antenna array. The surface wave modes consist of a propagating wave traveling along the dielectric slab in the dielectric and an evanescent field above the dielectric slab which decays with increasing height above the air/dielectric interface. These modes are therefore completely guided in the dielectric support structure and carry large amounts of power between the radiating elements of the antenna array. The strong mutual coupling caused by these surface wave modes causes rapid variations in the radiated power of the antenna array and the active input impedance of the radiating elements of the antenna array near the beam scanning locations which will support the surface wave. The dominant surface wave mode in the dielectric slab is the TM_0 mode [7] which has no cutoff frequency in a dielectric slab waveguide [8]. The effective coupling distance between the radiating element is essentially unlimited for the TM_0 mode because the only source of decay for this mode is dielectric loss [8].

The geometry of a dielectric slab which is backed by a perfect electric conducting ground plane is shown in Figure 2.2. The boundary conditions which are required for the surface wave to propagate in the slab are given by

$$k_z^{(d)} \sin\left(k_z^{(d)} d\right) - j\epsilon_r k_z^{(+)} \cos\left(k_z^{(d)} d\right) = 0 \tag{2.27a}$$

for the TM surface wave modes and

$$j k_z^{(+)} \sin\left(k_z^{(d)} d\right) + k_z^{(d)} \cos\left(k_z^{(d)} d\right) = 0 \tag{2.27b}$$

for the TE surface wave modes [9] where the z-directed wavenumbers of the surface wave

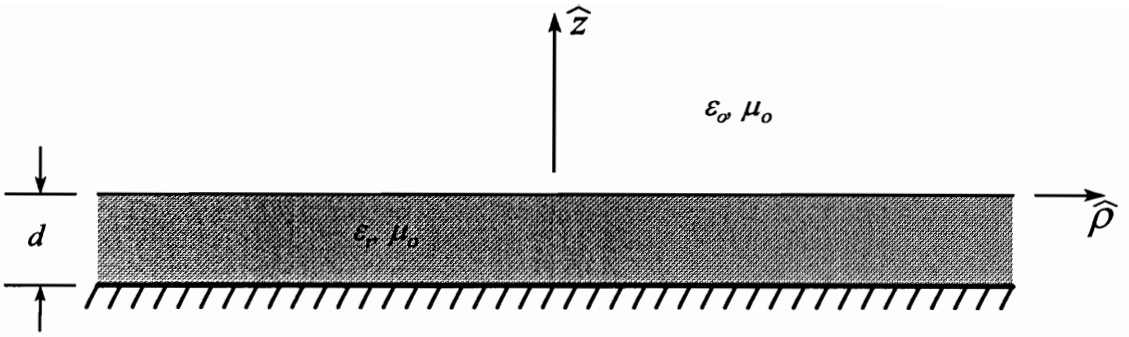

Figure 2.2. Geometry of the dielectric slab which is backed by a perfect electric conducting ground plane showing the depth of the slab, d, and the coordinate system.

modes are given by

$$k_z^{(+)} = \sqrt{k^2 - k_\rho^2} \tag{2.28a}$$

and

$$k_z^{(d)} = \sqrt{\epsilon_r k^2 - k_\rho^2}\,. \tag{2.28b}$$

Both the requirement mentioned previously of a propagating wave in the dielectric slab with an evanescent field above the slab and the j complex multiplier on one term of each of (2.27)

indicate that the transverse wavenumber for the surface wave mode must be in the range

$$k^2 < k_\rho^2 < \epsilon_r k^2. \tag{2.29}$$

The requirement on the transverse wavenumber of the surface wave given by (2.29) indicates that the surface wave is a product of a mode of the antenna array which is outside visible space for the air region above the air/dielectric interface. Bhattacharyya [7] found that the surface wave mode is generally the first mode outside visible space for most practical arrays. The surface wave is then excited in the antenna array if the phase shift

between adjacent radiating elements is such that each radiating element couples to the surface wave in phase with the surface wave. The excitation of the surface wave mode in the dielectric support structure of the antenna array results in extremely high field levels at the radiating element which are in phase with the radiating element for each cell of the antenna array. The TM_0 surface wave mode is, in fact, self-supporting for a lossless dielectric substrate and results in a unity reflection coefficient for each of the radiating elements of the antenna array since the requirement of (2.29) prevents power from radiating away from the antenna array face. Fortunately, a surface wave is only excited in phase at particular angles of beam scanning in the antenna array and therefore presents difficulties only at or near discrete beam scanning directions.

The beam scanning direction at which the surface wave mode is excited in phase at each of the radiating elements of the antenna array can be found from

$$\theta_{sw} = \sin^{-1}\left(\frac{k_{\rho_{sw}}}{k_o} - \frac{\lambda_o}{s}\right) \tag{2.30}$$

where $k_{\rho_{sw}}$ is the transverse wavenumber that satisfies (2.27a) and s is the interelement spacing of the antenna array. This result is based on the assumption that the surface wave exists as the first mode outside visible space as discussed in the previous paragraph and that the dielectric is thin enough to prevent surface wave modes other than the TM_0 surface wave mode from forming [7]. The thickness of the dielectric support substrate at which the first surface wave mode above the TM_0 mode, the TE_1 mode, can form is given by

$$d_{TE_1} = \frac{1}{4\sqrt{\epsilon_r - 1}}. \tag{2.31}$$

This result indicates that the thickness of the dielectric support substrate should be less

than approximately $0.2\lambda_o$ for typical dielectrics used in printed radiating element antenna arrays to prevent higher order surface wave modes from forming [10].

2.1.3 Infinite Array Analysis

Large, but finite, antenna arrays are usually characterized by one of two indirect methods. Either the performance of the large antenna array is characterized by evaluating a small antenna array as its size increases or by determining the performance of an infinite array and including adjustments for edge effects in the large array if necessary. The direct characterization of large antenna arrays is generally not practical due to the extremely large numbers of unknowns which are required in the analysis. The analysis of a large antenna array is generally most easily performed by assuming the antenna array to be infinitely large and accounting for edge effects if necessary [11]. The infinite array approach to large antenna array analysis allows the representation of the antenna array to be simplified by considering a periodic structure of the radiating elements in the array grid.

The periodic structure of the infinite array is used to simplify the analysis computations by using the periodicity to automatically include the effects of all of the radiating elements in the antenna array in the analysis of a single array grid cell [11]. The infinite array analysis approach can be used without accounting for the effects at the edge of the large finite antenna array if the antenna array is sufficiently large that the overwhelming majority of the elements are in the interior of the antenna array away from the edge. This approximation is based on the assumption that all of the interior elements experience the same mutual coupling environment in a large antenna array and the effect of the edge elements, which experience a different, variable mutual coupling environment, on the performance of the antenna array is minimal. As an added benefit, this approach to

the characterization of large antenna arrays presents the effects of the periodicity of the array grid spacing in a directly observable form [11].

The direct approach to the infinite array analysis of a large antenna array uses the periodicity of the array grid to expand the fields in an array grid cell in a Fourier series of modes with an added linear phase taper to account for the Floquet theory walls which separate the analysis cells [12, 1]. The linear phase taper is determined from the desired direction of beam scanning in the analysis. The Floquet walls can be simply described as constant phase shift surfaces between the cells of the array grid which impose this phase taper at the boundaries of the analysis cell. In this work, this series expansion will be referred to as a Floquet series for convenience. The radiating element in the analysis cell can be modeled using conventional Method of Moments (MoM) techniques because the coupling to the other radiating elements in the antenna array is included in the Floquet series expansion of the Green's Function used to couple the electric current density description of the radiating element in the analysis cell to the electric potential description of the radiating element.

The accuracy of the infinite antenna array approximation of large antenna arrays was studied by Wasylkiwskyj and Kahn [2]. Wasylkiwskyj and Kahn compared the aperture efficiency of the radiating element in an infinite array with the aperture efficiency of the radiating element in a partially excited infinite array to develop a measure of the energy coupled to the unexcited elements. In this case, the aperture efficiency of the radiating element is defined to include the effects of power reflected at the radiating element input as well as loss in the radiating element and the aperture taper of the radiating element. The aperture efficiency is given by

$$\eta_{ap}(\theta_o, \phi o) = \left(1 - |\Gamma_a(\theta_o, \phi o)|^2\right) \eta_{diss}(\theta_o, \phi o) \tag{2.32}$$

where $\Gamma_a(\theta_o, \phi o)$ is the active reflection coefficient of the radiating element in the fully active infinite antenna array scanned to $(\theta_o, \phi o)$ and $\eta_{diss}(\theta_o, \phi o)$ is the dissipative loss of the radiating element when the array is scanned to $(\theta_o, \phi o)$. The analysis performed by Waslkiwskyj and Kahn assumes that the radiating element is lossless [2].

Waslkiwskyj and Kahn [2] computed the aperture efficiency of the radiating element for several possible numbers of excited radiating elements in the infinite array environment. They proposed that the validity of the infinite array analysis approach can be estimated by the agreement between the aperture efficiency of the radiating element in the partially excited infinite antenna array of a given number of elements and array grid spacing and the aperture efficiency of the radiating element in the fully excited infinite antenna array of the same geometry. The efficiency of the array was defined as

$$\eta(\boldsymbol{a}) = \frac{\boldsymbol{a}^{\dagger}(I - S^{\dagger}S)\boldsymbol{a}}{\boldsymbol{a}^{\dagger}\boldsymbol{a}} \tag{2.33}$$

where $\boldsymbol{S}$ is the scattering matrix of the antenna array and $\boldsymbol{a}$ is the applied excitation of the antenna array. This definition of the aperture efficiency of the radiating elements of the antenna array is equivalent to the ratio of transmitted power to incident power for lossless radiating elements.

Wasylkiwskyj and Kahn [2] obtained numerical aperture efficiency results for excited portions of a infinite linear antenna array of 3, 7, 27, and all of the radiating elements for slot, dipole, and ideal radiating elements as a function of the interelement phase shift. The ideal element of Wasylkiwskyj and Kahn has a far-field pattern which is defined by

$$f(\theta) = \begin{cases} \cos\theta; & \theta \leq \pi \\ 0; & \pi < \theta \leq 2\pi \end{cases} \tag{2.34}$$

These results showed extremely good agreement between the fully excited infinite array and the 27 excited radiating element infinite array. They reported good agreement between the fully excited infinite array and the 7 excited radiating element infinite array for all cases with less than a 5% error in the aperture efficiency relative to the fully excited infinite array over approximately $\frac{3}{4}$ of the interelement phase shift range. Figure 2.3 shows the efficiency of the ideal radiating element for a planar antenna array with a square grid with 1, 9, 49, 121, 729, and all of the radiating elements in the infinite array excited as a function of interelement spacing for two different interelement phase shifts. These results indicate that the infinite antenna array analysis approach is probably acceptable for planar antenna arrays of ideal elements which are larger than 7×7 radiating elements.

This approach to the validation of the infinite antenna array analysis approximation provides only a preliminary estimate of the range of validity for the approximation. The use of a partially excited infinite antenna array in this analysis rather than a true finite antenna array introduces a source of possible error. Also, the simple element model cannot account for the possible surface wave and other coupling mechanisms which are unique to a dielectric support structure geometry. Deshpande and Bailey [3] addressed these concerns by comparing the active input impedance computed by the infinite antenna array approximation to the active input impedance computed using a mutual coupling matrix analysis approach for finite antenna arrays in a dielectrically supported antenna array geometry. They computed the mutual coupling of an antenna array of probe-fed, circular microstrip patch radiating elements printed on a perfect electric conductor (PEC) ground plane backed dielectric slab using an MoM analysis procedure with a dyadic Green's function to account for the dielectric effects. They characterized square antenna arrays of 9, 25, 49, and 121 elements. Deshpande and Bailey also computed and measured the mutual coupling and active input impedance of an 8 element linear array of

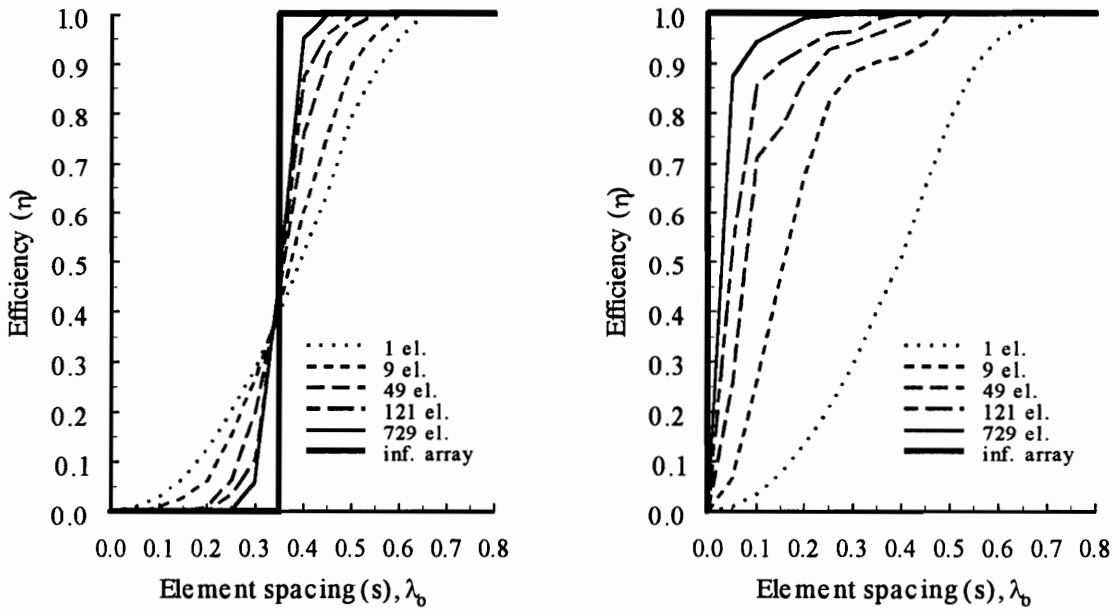

(a) $\frac{\pi}{2}$ interelement phase shift

(b) 0 interelement phase shift

Figure 2.3. Radiating element efficiency of Wasylkiwskyj and Kahn [2] for excited subarrays of 1, 9, 49, 121, 729, and all of the radiating elements in an infinite antenna array as a function of element spacing for two values of interelement phase shift. The infinite antenna array approximation can be considered valid when the efficiency values for the interelement spacing of the antenna array are comparable to the infinite array efficiency.

these radiating elements. These comparisons led to the conclusion that the infinite antenna array analysis approximation is generally valid for printed radiating elements on a ground plane backed dielectric support substrate for antenna arrays which have 7×7 or more elements.

2.2 Analysis Techniques for Radiating Element Characterization

The basic antenna array principles which were discussed in Section 2.1 can be applied by four fundamentally different approaches to characterize a large antenna array. After ideal array theory, the most primitive approach to the characterization of a large antenna array consists of simply analyzing the entire antenna array using a commonly available computational electromagnetics analysis package. This approach can be based on either a fully excited antenna array analysis including the necessary radiating element phasing for each of the desired beam scanning directions or by exciting a single element at a time to develop the set of active element patterns as discussed in Section 2.1.2. The second possible approach to the characterization of a large antenna array infers the behavior of the antenna array from the grating lobe series of the antenna array. This technique provides a good estimate of the location of possible scan blindness for antenna arrays of simple radiating elements but provides only limited input impedance information for more complicated elements. The third approach to the analysis of a large antenna array uses the mutual coupling technique discussed in Section 2.1.2. This approach can be used by computing the mutual coupling with a standard computational electromagnetics analysis tool or a custom software analysis tool for special geometries. Two characterization techniques are based on the infinite array approach to the analysis of large antenna arrays. The first characterization technique of this type is the waveguide simulator model for the large antenna array. Although this approach is not strictly an analysis technique it will be discussed. The second characterization technique which uses an infinite array analysis approach to model large antenna arrays is based on a spatial harmonic series expansion of the array grid. This is the approach used in the theoretical development presented in Chapter 3. These four classes of large antenna array analysis techniques are discussed in this section in the order in which they were introduced.

2.2.1 Existing Computational Electromagnetics Analysis Tools

As mentioned above, a means of characterizing large antenna arrays is necessary for the design of this type of antenna or its radiating elements. The best way to develop this capability is to use a mature computational electromagnetics analysis code. This approach avoids the extensive development and validation time for a custom software analysis tool and increases confidence in the computational results. The probability that a common computational electromagnetics code could accurately analyze large antenna arrays was recognized to be very low but the desirability of this approach led to a survey of the available codes to determine their suitability for this type of analysis. The computational electromagnetics codes which were considered can be divided into two major categories: codes which use a traditional free space kernel or which have a limited dielectric analysis capability and codes which are intended to analyze structures with a multi-layered dielectric structure.

Four computational electromagnetics codes which fall into the first of these categories were considered. These codes were the Numerical Electromagnetics Code (NEC v.4) [13], the Ohio State Electromagnetic Surface Patch code (ESP v.4) [14], the PATCH code [15], and the WIRE code [16], which is an improved variation on the MININEC code [17]. These analysis codes are based on an integral form MoM analysis of a metal structure in either a free-space environment or an infinite PEC ground plane environment. Two of these codes, NEC and ESP, add a limited capability to analyze structures which include dielectric effects.

The NEC code allows the characterization of metal structures composed of both wire and plate electric current elements [13]. These metal structures can be analyzed in a free-space environment or an environment which includes either an infinite PEC ground

plane or a dielectric half-space. The analysis in the presence of the dielectric half-space is formulated to include dielectric loss effects and is primarily useful for the characterization of antennas over a non-perfect ground surface. The analysis of metal structures in the NEC code is based on the evaluation of the magnetic field integral equation (MFIE). This choice of integral equation formulation restricts the use of plate elements in the NEC code to closed surfaces with non-vanishing internal volumes because the MFIE expresses the difference of the current densities on the two sides of the patch element as a function of the total current density on the element. This formulation restricts NEC primarily to the analysis of antenna arrays of wire radiating elements.

The Ohio State ESP code also allows the characterization of metal structures which are composed of both wire and plate electric current elements [14]. The plate electric current elements in the ESP code are described by a bi-quadrilateral electric current density patch description. The ESP code can characterize these structures in the either the free-space environment or in the presence of an infinite PEC ground plane. This code also allows the use of dielectric plate elements but models these elements using a sheet impedance approach which is primarily useful for radar cross section (RCS) analysis. The analysis approach used in the ESP code is based on the electric field integral equation EFIE which is suitable for the analysis of open surface structures unlike the MFIE formulation used in NEC. The main limitations imposed by ESP for the analysis of antenna arrays are the use of a thin wire kernel and the lack of a suitable small plate/wire attachment element. The use of a thin wire kernel in ESP requires that non-connected wire segments be separated by several wire radii. This choice of kernel also restricts the maximum bend in a single wire to approximately 45° at any single point. The lack of a small plate/wire attachment element prevents the use of the plate electric current elements to describe a radiating element because the minimum size of the attachment between wire

and plate electric current elements is approximately $0.2\lambda_o$ and sources can be placed in wire electric current elements only.

The PATCH code was developed for the analysis of structures described by plate electric current elements [15]. This code can characterize these structures in either a free-space environment or in the presence of up to three orthogonal infinite PEC ground-planes. The PATCH plate electric current elements in the PATCH code are bi-triangular electric current density patches. These plate electric current elements can contain a source at the joining edge of the bi-triangular patch element. Analysis in the presence of dielectric materials is not supported by the PATCH code.

The WIRE code was developed as an improved version of the MININEC series of personal computer based NEC codes [16]. The WIRE code can characterize structures composed of wire electric current elements in either a free-space or an infinite PEC ground plane environment. The kernel used for the analysis of wire electric current elements in the WIRE code has been improved from the kernel used in MININEC to model the wire segments correctly as cylindrical PEC shells. This model of the wire segments is still limited to wire radii which are much smaller than λ_o because circumferential variation of the electric current is not allowed.

These four computational electromagnetics codes are useful for the analysis of many antenna and scattering structures but are not appropriate for use in the characterization of radiating elements in large antenna arrays or antennas which are printed on dielectric substrates. Antenna arrays of only moderate size can be analyzed with these computational analysis codes because of the limit on the number of unknowns which can be modeled. On Intel architecture personal computers, the first three of these codes are limited to less than approximately 2000 unknowns for a core memory of 64 MB.

The use of virtual memory has proven to be impractical because the execution speed is much lower when virtual memory is used. The fourth code, WIRE, is presently limited to approximately 160 unknowns by limitations imposed by the source code compiler. These limitations restrict these codes to the analysis of antenna arrays of less than 400 radiating elements for extremely simple radiating elements such as half-wave dipoles. The analysis of antenna arrays using more complex radiating elements such as Archimedean spiral antennas would limit the array size to less than 5 total radiating elements. Finally, the two codes which include dielectric modeling, NEC and ESP, do not use models which are suitable for use in a radiating element structure.

Three computational electromagnetics codes which fall into the second category, that can handle layered dielectrics, were considered. These codes were the Zeland Software code IE3D [18], the Sonnet Software code SONNET [19], and the Boulder Microwave code ENSEMBLE [20]. These computational electromagnetics code can analyze metal structures in a multi-layered dielectric environment which can include multiple infinite ground planes. The IE3D and ENSEMBLE codes were quickly determined to be inappropriate for modeling large antenna arrays of complex radiating elements because of limitations on the practical number of unknowns. At this point the investigation of these two codes was terminated.

The SONNET code is intended to be used to analyze multi-layered microstrip and stripline circuits in a metal enclosure [19]. This analysis package is capable of modeling planar circuits using a rectangular electric current element description of the metallization at each interface between two dielectric layers. The SONNET code also allows vias to be specified between the layers of metallization. The solution technique appears to be MoM based on a cavity type modal expansion of the electromagnetic fields in the analysis box.

These mode weights for these fields are then determined by enforcing boundary conditions in a sampled sense at each of the interfaces between dielectric layers. Both the core memory required and the execution time of the analysis are heavily influenced by the size of the analysis box as well as the number of unknowns used to describe the metallization. This relationship suggests that the software in some way stores large amounts of data for each mode rather than summing the effects of the mode and then reusing the storage space.

The SONNET code can be used to characterize radiating structures although it was not designed for this purpose. The analysis of radiating structures using SONNET is approached specifying the surface impedance of the upper, and lower if desired, sides of the metal analysis cell to match the impedance of free-space. The other sides of the analysis cell are defined as PEC surfaces in the analysis algorithm. The use of the free-space impedance for the upper boundary of the analysis cell is claimed to reasonably approximate an open-ended waveguide geometry with the metal analysis cell. The characterization of an antenna in this environment is essentially the waveguide simulator approach to infinite antenna array analysis which will be discussed in Section 2.2.4 although this is not mentioned in the user's manual. The core memory and analysis execution time requirements discussed above severely limit the ability of SONNET to characterize more complex radiating elements using this approach.

2.2.2 Grating Lobe Series Based Technique

The grating lobe series approach to the analysis of large antenna arrays is based on analyzing the interaction of the radiating element with the higher order modes which represent the stored energy in the antenna array structure as well as with the radiating

mode(s). The higher order modes are based on a series of stored energy modes which represent grating lobes outside visible space for the array grid geometry. This series of grating lobes is expressed by (2.20) for an equally spaced linear array. The grating lobe series is essentially a Floquet series. This approach to the analysis of large antenna arrays is well suited to the characterization of simple radiating elements because it results in a simple analytic description of the input impedance of the radiating element [12].

The grating lobe approach to the characterization of a large antenna array is closely related to the infinite array analysis techniques which are described in Section 2.2.4 but appears to be limited to radiating elements which can be described by a single electric or magnetic current density basis function of a shape which is known *a priori*. This approach to the characterization of large antenna arrays is reported to be applicable to elements such as infinitesimal dipoles, half-wave dipoles and patch elements as well as small slots, half-wave slots, and open ended waveguides by duality [12]. The effects of the mutual coupling throughout the infinite array grid are calculated in the grating lobe series based approach by determining the coupling between the single basis element description of the radiating element and the full set of modes which could be supported by the array grid geometry [21]. The single basis function limitation of the approach reduces its adaptability greatly because the technique cannot be used to characterize complicated elements or account for variations in the current distribution on the radiating element [22]. The surface wave series was shown by Frazita [21] to correctly predict the scan blindness and active reflection coefficient for an antenna array of circular waveguide apertures covered by a dielectric sheet. Frazita reports that this geometry was adequately described by the series of grating lobes out to 24 grating lobes from visible space.

2.2.3 Mutual Coupling Based Technique

The performance of a non-ideal antenna array can be characterized by using the mutual coupling analysis technique described in Section 2.1.2. The mutual coupling between the radiating elements of the antenna array is computed using conventional spatial domain computational electromagnetics analysis [5]. This computational electromagnetics analysis of the finite antenna array can typically be performed using only two elements with an existing code such as those described in Section 2.2.1 or an analysis code developed for the specific geometry of the antenna array. This approach to the characterization of large antenna arrays allows the edge effects in the large antenna array to be included in the analysis [5]. As mentioned in Section 2.1.2, this type of characterization of large antenna arrays is limited because at is usually assumed that the electric current distribution on each radiating element is not affected by the mutual coupling between the radiating elements.

The analysis by Deshpande and Bailey [3] of finite antenna arrays of circular microstrip patch radiating elements used this mutual coupling based characterization approach. The mutual coupling between these radiating elements was computed using a specifically developed MoM analysis code which used a dyadic Green's function to account for the ground plane backed dielectric slab on which the circular patches were printed. Deshpande and Bailey choose circular microstrip patch radiating elements to reduce the computational demands made on this characterization approach for larger antenna arrays. This choice of radiating element also simplified the modeling of the radiating elements because of the high Q of microstrip type antennas allowed the circular microstrip patches to be modeled with a single electric current density basis function for each of the patches. The mutual coupling for the array was computed using a forced

electric current excitation to determine the mutual impedance matrix as discussed in Section 2.1.2. rather than the scattering matrix which is found using a free, constant power excitation [5]. Deshpande and Bailey also performed this analysis for an 8 element linear array of the circular microstrip patch radiating elements. They constructed and measured this antenna array verify the analysis approach. Good agreement was reported between the measured and computed results for this linear antenna array [3].

2.2.4 Infinite Array Based Techniques

Waveguide simulation and Floquet boundary cell analysis are the two approaches to the characterization of large antenna arrays which are entirely dependent on the infinite antenna array approximation. The waveguide simulation approach can be implemented by either analysis or measurement while the Floquet cell analysis approach can only be performed by analysis. Although not strictly an analysis technique, the waveguide simulation approach to the characterization of large antenna arrays is introduced here because of its similarities with the Floquet cell analysis technique. Both of these large antenna array characterization techniques only require the analysis of a single cell of the antenna array geometry which includes a few radiating elements at most. The effects of mutual coupling between the radiating elements of the antenna array are included in each of these types of analysis cell by the careful selection of the boundary conditions at the vertical walls of the analysis cell.

Waveguide Simulation

A waveguide simulator may be constructed by placing a cell of the large antenna array which is to be characterized on a transverse plane of a section of rectangular waveguide [23]. This cell is composed of one or more radiating elements in the antenna

array grid geometry of the infinite antenna array. The cell is usually not the unit cell of the antenna array grid but a larger section of the array. Like the unit cell of the antenna array, this analysis cell can be repetitively placed to represent the antenna array geometry. The cell is chosen such that the waveguide walls are located along planes of symmetry of the radiating elements as well as the antenna array grid. The choice of antenna array cell for the waveguide simulator is determined by the requirement of zero tangential electric field at the waveguide walls.

The waveguide simulator representation of the infinite antenna array is possible because any waveguide mode can be decomposed into either two or four plane waves [23]. The number of plane wave components modeled by each waveguide mode is equal to twice the number of independent directions in which the waveguide mode varies. For instance, the [1,0] and [0,1] modes of the waveguide model two plane waves while the [1,1] mode models four plane waves. The angle between the plane waves is such that the interference of the electromagnetic fields satisfies the waveguide boundary condition of zero tangential electric field at the walls of the waveguide. This requirement on the plane waves indicates that the plane waves which represent the waveguide mode can be viewed as being incident on a transverse plane in the waveguide symmetrically about the waveguide axis. The projection of the propagation vectors and polarization vectors of the component plane wave modes in the waveguide simulator onto the transverse plane is shown for several waveguide modes in Figure 2.4. For any transverse plane in the waveguide the effective angle of incidence, the angle between the longitudinal axis of the waveguide and the plane wave components, of this set of plane waves can be found from

$$\theta_{inc.} = \text{asin}\left(\frac{\lambda_o}{\lambda_c}\right) \tag{2.35}$$

where λ_o is the free space wavelength at the frequency of operation and λ_c is cutoff

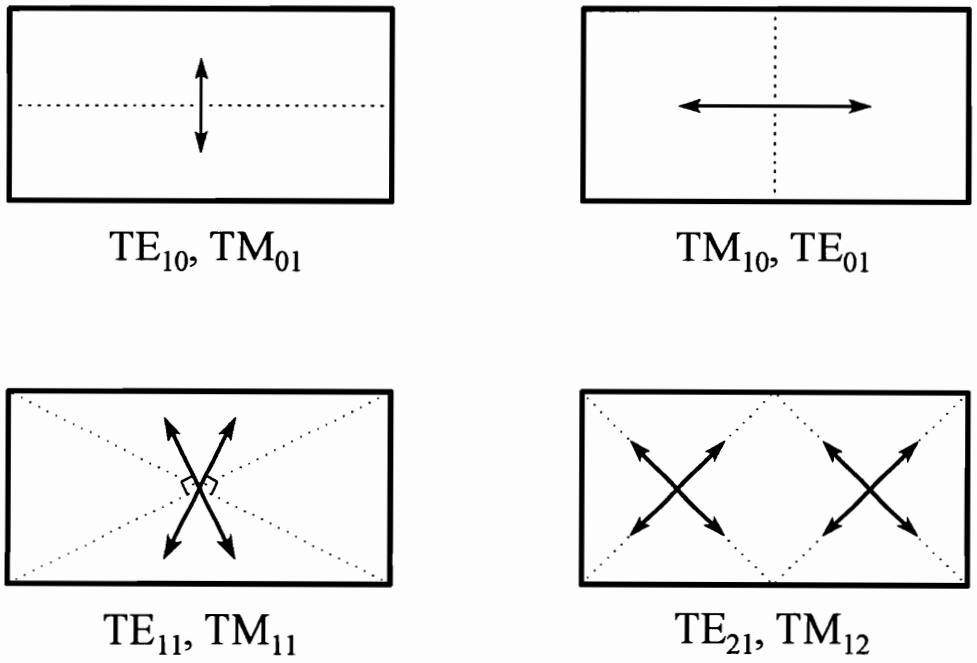

Figure 2.4. Directions of propagation and polarization for the plane waves modeled by several waveguide modes in the waveguide simulator [23]. The dotted lines show the projection of the propagation vectors of the plane wave modes in the simulator onto the transverse plane. The arrows show the polarization vectors of the plane waves projected onto the transverse plane.

wavelength of the waveguide mode which is modeling the plane waves [23]. A waveguide simulator cannot model the broadside scanned antenna array because this would require $\lambda_c = 0$ in (2.35). The simulation of broadside radiation from the antenna array would require an infinitely large waveguide simulator.

The choice of the waveguide mode used in the simulator also controls the polarization of the plane wave components which are effectively incident upon the antenna array. Oliner and Malech [23] defined the simulated plane waves as H-polarized if a magnetic field component lies along the longitudinal axis of the simulator (TE waveguide modes) and E-polarized if a electric field component lies along the longitudinal axis (TM waveguide modes). The direction of the plane of propagation of the plane wave

components determine the polarization of the electromagnetic field relative to the waveguide. The plane of polarization is orthogonal to the plane of propagation of the plane wave components of the waveguide modes in Figure 2.4. While any polarization and incidence angle for the plane wave can be modeled using this approach by using the appropriate waveguide mode, practical considerations, such as spuriously excited waveguide modes limit its usefulness to the lower numbered waveguide modes [23].

The radiating elements are terminated in a known impedance through the feed line which will be used for the element in the full antenna array. The waveguide is then excited by a waveguide mode which will cause this construct to represent a cell of the infinite antenna array under illumination by a plane wave from a given direction. The ratio of the power reflected from the radiating elements to the power illuminating the radiating elements is measured and used to compute the reflection coefficient of the infinite antenna array when excited by this plane wave. The reflection coefficient measured in this manner is identical to the reflection coefficient of the infinite antenna array for a plane wave which is incident on the antenna array from the direction given by (2.35) since all of the illuminating power must either be reflected (indicating mismatch in the radiating elements) or absorbed (transmission in the radiating elements). This relationship can be shown by considering the waveguide mode to be the superposition of the set of plane waves described above. The input impedance of the radiating elements can then be found from the known terminations of the radiating elements and the reflection coefficient. Alternately, the input impedance of the radiating elements in the waveguide simulator can be measured using standard techniques by feeding the elements with the correct phase progression for the beam scanning direction which the simulator was designed and measuring the input impedance directly. This direct measurement of the input impedance requires that the waveguide section comprising the simulator be properly terminated.

Floquet Series Analysis

The analysis algorithm developed in Chapter 3 is based on the Floquet cell approach to the characterization of large antenna arrays. Like the waveguide simulation approach, the Floquet cell approach is based on the infinite antenna array approximation to the large antenna array. The Floquet cell approach is more advantageous for computational analysis than the waveguide simulation approach because Floquet cell analysis requires only a single unit cell of the antenna array grid geometry to be analyzed. As discussed above, the waveguide simulation approach can require the analysis or measurement of several unit cells of the antenna array grid geometry to generate the symmetry required by the boundary conditions at the waveguide walls. The Floquet cell approach is also advantageous because it allows a full range of beam scanning for the same analysis cell. The single major disadvantage of the Floquet cell approach is that, unlike the waveguide simulator, the Floquet cell cannot be physically constructed because of the boundary conditions which are required at the vertical walls of the cell. A brief survey of previous uses of the Floquet cell approach to the characterization of large antenna arrays is given here. The theory of this approach is developed in detail in Chapter 3 and will not be discussed in this section.

There are three different ways in which the Floquet cell approach to the characterization of large antenna arrays can be applied: single basis function descriptions of the radiating element, multiple whole-domain descriptions of the radiating element, and multiple sub-domain descriptions of the radiating element. The simplest form of large antenna array characterization using the Floquet analysis cell approach uses only a single basis function to describe the electric current or aperture fields of the radiating element. This approach to the characterization of large antenna arrays is essentially the same as the grating lobe series approach discussed in Section 2.2.2 in that it ignores the possibility that

the current or field distribution may be affected by the mutual coupling. This type of Floquet cell analysis was used by Munk, Kouyoumjian, and Peters [24] to study periodic planar sheets of strip dipoles. In this study, the reflection of plane waves from the array was analyzed. Pozar [25] used this technique to determine the performance of an antenna array composed of vertical monopoles embedded in a dielectric slab backed by a ground plane. Pozar modeled these monopoles with a single filamentary pulse basis function. The main purpose of this study was to determine the effects of probe feeds, modeled by these monopoles, on a rectangular antenna array of probe-fed microstrip patches.

An approach to more accurate Floquet cell analysis is to use multiple whole-domain basis functions to describe the radiating element. This approach is usually used for antenna arrays of relatively simple radiating elements such as open-ended waveguide, microstrip patch, or dipole elements. Farrell and Kuhn [22] used this approach to study the effect of mutual coupling on an infinite planar antenna array of rectangular waveguide horns. The fields in the aperture of the waveguide horn in the Floquet analysis cell were modeled by the sum of 25 weighted waveguide modes. Farrell and Kuhn noted that the grating lobe approach to the characterization of large antenna arrays is incapable of predicting mutual coupling effects which alter the field or current distribution on the radiating element. This approach was reported to yield excellent results including the accurate prediction of a 32 dB null in the far-field pattern of the antenna array. This null is also predicted by the grating lobe analysis but the location of the null is predicted less accurately [22].

Pozar and Schaubert [10] used multiple whole-domain basis functions to describe an antenna array of rectangular microstrip patches. The effects of the feed-probes on the patch were accounted for as lumped element inductances. They found good agreement

with measured results for the input impedance of the radiating elements in a waveguide simulator for thin dielectric substrates but it was suggested that a better probe model is required for thicker support substrates. Hall and Mittra [26] used this technique to characterize the scattering of plane waves from periodically spaced strips of resistive material. The results of this study show noticeable dips in the reflection coefficient for the plane wave incident upon the strip grating at approximately the spacings where grating lobes of the reflected wave would enter visible space. Hall and Mittra reported that the Q of the structure at resonance was reduced compared to a PEC strip grating.

Zavosh and Aberle [27] combined the use of multiple whole-domain basis functions and a single whole-domain basis function over different sections of the radiating element. This approach can be considered as a hybrid between a whole-domain modal description of the radiating element and a sub-domain description of the radiating element. Zavosh and Aberle used this technique to study the effects of mutual coupling on beam scanning performance in an antenna array of cavity-backed circular patches. The geometry of a cross-section of a portion of this antenna array is shown in Figure 2.5. The gap around the perimeter of the patch was replaced by a magnetic current density in the gap which was modeled using a series of whole-domain modal basis functions. The electric current density on the probe feed of the patch element was modeled using a single whole-domain pulse basis function because the length of the probe feed was much less than one wavelength. Zavosh and Aberle reported improvements in the beam scanning performance for this antenna array as compared to a conventional antenna array of microstrip patch elements [27].

The use of a sub-domain basis function description allows the analysis of antenna arrays of complicated radiating elements. This approach to Floquet cell characterization

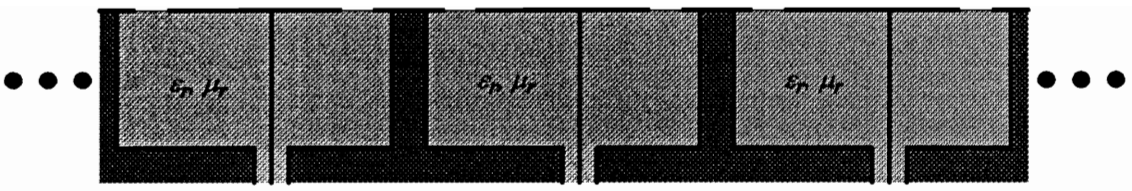

Figure 2.5. Cross-sectional view of a portion of the antenna array of cavity-backed circular patches analyzed by Zavosh and Aberle [27]

has been used by Pozar and Schaubert [28], Chu [29], and Bayard [30] to analyze the performance of large antenna arrays with dipole radiating elements. Rectangular piecewise sinusoidal sub-domain basis functions were used in each of these studies to describe the electric current density distribution on dipole radiating elements. Pozar and Schaubert studied the beam scanning performance of an infinite antenna array of strip dipole elements printed on dielectric substrate supports of different thickness. The sub-domain basis function in this study included only the electric current density which was directed along the axis of the dipole. The analysis found that the blind spots of these antenna arrays corresponded to the beam scanning locations of the surface waves supported by a dielectric slab with the same geometry.

Chu analyzed an antenna array of strip dipoles which was printed on a dielectric substrate backed by a ground plane covered with radar absorbing material [29]. This antenna array was also covered by a three dielectric layer radome structure. They modeled the dipole elements using a piecewise sinusoidal sub-domain basis function. Chu also constructed a waveguide simulator for a simple geometry with a single radome dielectric and reported good agreement between the computed and measured results.

Bayard used the sub-domain basis function description of the radiating element in the Floquet cell characterization technique to investigate the beam scanning performance

of dipoles printed on dielectric fences protruding from the ground plane [30]. These dipole elements were fed by a microstrip line printed on reverse side of the dielectric fences. His approach can also include analyze the performance effects of a planar dielectric radome laid across the fences. Figure 2.6 shows the geometry of a section of a single dielectric fence in this array structure including the possible radome. Bayard used a two-dimensional rectangular piecewise sinusoidal electric current density basis function to describe these radiating elements. His computed results found that scan blindness occurs at approximately $\theta_o = 25°$ in the E-plane for dipoles on a $0.5\lambda_o$ array grid when located on a dielectric fence $0.3\lambda_o$ high for $\epsilon_r = 2.2$.

This characterization approach is also suitable for more complicated structures. Pozar [31] analyzed an infinite antenna array of aperture coupled microstrip patches. A series of modal, whole-domain basis functions was used to describe the electric current density on the microstrip patch in this analysis. The electric field in the aperture was described by a single piecewise sinusoidal basis function. The microstrip feed network was assumed to be an insignificant contributor to the mutual coupling effects in this antenna array and was therefore not modeled directly in the analysis. Pozar constructed a waveguide simulator for beam scanning in the H-plane of this antenna array and reported good agreement between measured and calculated results.

Finally, Schuman, Pflug, and Thompson [32] developed an approach which allows the analysis of wire radiating elements of arbitrary shape in an infinite planar antenna array. The wire radiating element is described by a set of sub-domain electric current wire basis functions. These basis functions are defined as pulse electric current basis functions. This development includes a modification to the MoM technique which allows the wire radiating element to be bent out of the plane of the antenna array grid. The input

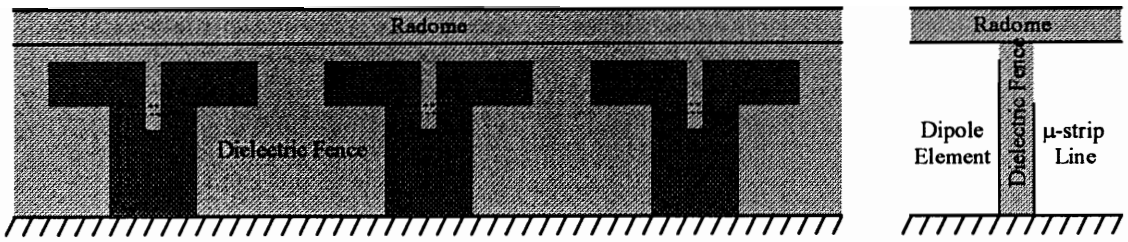

Figure 2.6. Geometry of a section of a single dielectric fence for the array of dipole elements analyzed by Bayard [30]. The dipole element is fed by the μ-strip line printed on the reverse side of the fence.

impedance computed for a dipole antenna array using this analysis approach was reported to compare well to results for a 37 element antenna array computed using an unspecified spatial domain MoM code [32].

3. THEORETICAL DEVELOPMENT

This chapter presents the theoretical development of the Method of Moments (MoM) analysis of infinite arrays of arbitrarily shaped, planar radiating elements which are printed on a dielectric support substrate which is backed by a perfect electric conducting ground plane. The chosen solution technique includes the effects of the full infinite array in the analysis of a single rectangular cell of the array by using a Floquet modal description of the electromagnetic fields to couple the electric current density to the electric potential on the sub-domain basis functions which describe the radiating element. This chapter begins with a brief discussion of overall analysis approach in Section 3.1. The Method of Moments approach is introduced in Section 3.2. The radiating element is modeled with a set of bi-triangular patches described in Section 3.3. The description of the electromagnetic fields in the analysis cell is discussed in Section 3.4. Sections 3.5 and 3.6 develop the calculation of the elements of the impedance matrix used in the MoM analysis. The source model and the filling of the impedance matrix are discussed in Section 3.7. The chapter concludes in Section 3.8 with a discussion of the approach used to calculate the antenna properties which are derived from the electric current density distribution found in Section 3.7.

3.1 Overview of the Analysis Approach

The analysis approach used here for the characterization of the arbitrarily shaped, planar printed radiating element is the Method of Moments [33]. The Method of Moments allows the integral or differential formulations used in electromagnetics to be replaced by a system of linear equations. This substitution simplifies the solution of the electromagnetic

system but requires that the structure be described by weighted sets of basis and testing functions. The coefficients of these linear equations, the coupling between the normalized basis and testing functions, are determined by finding the response of the unity testing functions to each of the unity basis functions. The resulting set of linear equations can then be solved for known weights of the testing functions to find the unknown basis function weights. In this analysis approach sub-domain basis functions are used to describe the electric current density on the radiating element while the testing functions are used to describe the electric potential across each of the sub-domain basis functions. The basis functions used here are in the form of bi-triangular patches of linearly varying electric current density. The testing functions are pulse integrals over the electric field tangential to each of the basis functions. The coupling between the basis and testing functions, the matrix of mutual and self-impedances of the sub-domain basis functions, is determined be satisfying Maxwell's equations for the electromagnetic fields caused by the unity basis functions.

Floquet's theorem for periodic structures is used to allow the characteristics of the radiating element in the fully active infinite antenna array to be determined from the analysis of single rectangular cell of the array. The analysis cell is open above the radiating element and closed by a dielectric substrate backed by a ground plane beneath the radiating element. The electromagnetic fields in this analysis cell are defined in a Floquet series expansion. This expansion is essentially a Fourier expansion with the addition of a constant phase taper across the analysis cell equal to the phase taper required scan the main beam in the direction of desired beam scanning, (θ_o, ϕ_o). The fields at opposite Floquet side walls of the analysis cell have a relative phase of the interelement phase shift required for the beam scanning since any location in adjacent cells must have this phase shift. The fields are described by $TE^{(z)}$ and $TM^{(z)}$ Floquet modes where the (z)

superscript indicates that the modes is polarized transverse to the z-axis. These modes are traveling in the $+z$-direction in the air region above the radiating element and standing wave modes in the dielectric substrate below the radiating element. The Floquet modes are orthogonal in the analysis cell allowing the boundary conditions at the walls of the analysis cell and at the air/dielectric interface where the radiating element is printed to be enforced mode-wise. The boundary conditions can be used to define a coupling dyadic from the electromagnetic fields for each of the modes. This dyadic describes the coupling between each normalized electric current density basis function and each electric potential testing function in a mode-wise sense.

The modal weights of each sub-domain basis function are then found in a manner similar to the determination of the weights of a Fourier series. These weights describe the whole domain electric current density basis function for each Floquet mode equivalent to the sub-domain electric current density basis function for that particular Floquet mode. The modal form of the electric potential testing functions are found by simply integrating the tangential fields over the each sub-domain basis function for each Floquet mode. The mutual and self-impedance matrix for the Method of Moments analysis can then be filled for a given Floquet mode from the inner products of the modal testing function with the coupling dyadic with the modal basis function. Because the Floquet modes are orthogonal, the impedance matrix contributions for each mode can be summed to find the full mutual and self-impedance matrix for the sub-domain basis functions.

The system of linear equations developed from the Method of Moments analysis can be solved once the mutual and self-impedance matrix is known and the electric potential across each sub-domain element is specified. In this analysis the sub-domain element is defined as an infinitely thin sheet of perfect electric conductor so the element

voltage is zero except where a source is connected. The electric potential of sub-domain element containing sources is the source voltage. The system of linear equations is solved using an LU-decomposition for the weights of the sub-domain electric current density basis functions. The input impedance and power of the radiating element in the fully excited infinite array environment is then found from the electric current and potential at each source location. Finally, the radiation characteristics of the radiating element are found by integrating the propagating modes, $\mathrm{Re}\{k_z\} > 0$, over the analysis cell.

3.2 The Method of Moments [33]

Any electromagnetic system can be characterized by determining the electric current density distribution which is required to the satisfy boundary conditions including the effects of the impressed source. In principle, the problem can be approached by finding the magnetic vector potential, $\overline{A}(\overline{r})$, from

$$\overline{A}(\overline{r}) = \int_{v'} \overline{\overline{G}}(\overline{r}, \overline{r}') \cdot \overline{J}(\overline{r}') \mathrm{d}v' \tag{3.1}$$

where $\overline{J}(\overline{r}')$ is the electric current density distribution and $\overline{\overline{G}}(\overline{r}, \overline{r}')$ is the appropriate dyadic Green's function [34] for the piece-wise homogenous geometry under consideration. The vector magnetic potential, $\overline{A}(\overline{r})$, is then used to find the magnetic and electric field, $\overline{H}(\overline{r})$ and $\overline{E}(\overline{r})$, from

$$\begin{aligned} \overline{H}(\overline{r}) &= \nabla \times \overline{A}(\overline{r}) \\ \overline{E}(\overline{r}) &= \frac{1}{j\omega\epsilon}\left(\nabla \times \overline{H}(\overline{r}) - \overline{J}(\overline{r})\right) \\ &= \frac{1}{j\omega\epsilon}\left(k^2 \overline{A} + \nabla\left(\nabla \cdot \overline{A}\right)\right) \end{aligned} \tag{3.2}$$

where $\overline{J}(\overline{r})$ is the electric current density in the system and is zero except over the source

region, V. The boundary conditions are then enforced on the magnetic and electric fields, $\overline{H}(\overline{r})$ and $\overline{E}(\overline{r})$, to find the electric current density distribution, $\overline{J}(\overline{r}')$, over the source. Once the electric current density distribution is known, (3.1) and (3.2) may be used to determine the field characteristics of the system. The input characteristics of the system can be found from the relationship between the electric current density distribution, $\overline{J}(\overline{r}')$, at the source and the voltage impressed by the source as

$$Z_{source} = \frac{V_{source}}{\int_{l'} \overline{J}(\overline{r}')\, \mathrm{d}l'} \tag{3.3}$$

where l' is the cross section of the source surface patch.

The closed form approach to the solution of the electromagnetic system with a completely unknown electric current density distribution is generally not practical. The Method of Moments (MoM) is a numerical technique which replaces the analysis of the arbitrary electric current density distribution of (3.1) with a much more easily solved set of linear equations. In the MoM, the current density distribution is expressed as a weighted summation of known current distributions represented by a set of current density basis functions, $\overline{j}_n(\overline{\rho})$. The boundary conditions are either automatically enforced by the choice of the electromagnetic field expansion or are enforced in a sampled sense through the use of a set of testing functions, $\overline{v}_n$. The set of linear equations obtained by the MoM process can then be solved to obtain the current weights which represent the current density distribution. It is worth noting at this point that the Method of Moments is identical to the Method of Weighted Residuals commonly used in Engineering Mechanics when applied to differential equations.

The electric current density distribution in this analysis is represented by a weighted sum of bi-triangular basis functions to be described in Section 3.3.1. The

boundary conditions of the magnetic and electric fields at the sides, top, and bottom of the analysis cell described in Section 3.4.1, are enforced automatically by the choice of Floquet field expansions described in Section 3.4.2. The boundary conditions of the magnetic and electric field at the dielectric/air interface in the analysis cell is enforced by the linking of the fields in the air and in the dielectric with the electric current density basis set as described in Section 3.5.2 and Section 3.5.3. Finally, the electric field boundary condition is forced to zero over the elements of the perfect electric conductor (PEC) electric current density basis set as described in Section 3.3.2.

The field expansions used here replace the integral over the volume in (3.1) with a double infinite summation over the x- and y-directed Floquet modes in the analysis cell. The integrals over the basis and testing set elements may then be performed analytically instead of numerically. This approach results in a set of linear equations given by

$$\boldsymbol{V} = \boldsymbol{Z}\boldsymbol{J} \tag{3.4}$$

where $\boldsymbol{V}$ is the column vector of the source voltages impressed at center of each bi-triangular electric current density basis function, $\boldsymbol{Z}$ is the normalized impedance matrix which defines the coupling between the electric current density in each bi-triangular basis function and the voltage which results across each of the pulse testing functions, and $\boldsymbol{J}$ is the column vector of the weights of each of the bi-triangular electric current density basis functions. This set of linear equations is solved to determine the correct electric current density weights.

3.3 Spatial Sub-Domain Element Description

The metallization of the radiating element is modeled in this analysis by a weighted set of sub-domain basis functions. This approach to the radiating element model was

chosen to allow a radiating element with a totally unknown shape and electric current density distribution to be modeled without requiring changes to the analysis algorithm. The basis functions are described over the bi-triangular patch sub-element [35] shown in Figure 3.1. As shown, the n^{th} bi-triangular patch sub-domain element is defined by a shared edge, the line segment $(\overline{\rho}_{n1}, \overline{\rho}_{n2})$, and two outside vertices, $\overline{\rho}_{n3}$ and $\overline{\rho}_{n4}$. The bi-triangular patch sub-elements are modeled as infinitely thin perfect electric conductors lying on the air/dielectric interface in the analysis cell. The basis set for the MoM analysis is developed from the electric current density across the bi-triangular patch sub-domain elementdescribed in Section 3.3.1. The testing set for the MoM analysis is based on a relaxed electric field boundary condition at the PEC sheet which comprises the sub-domain element. This development is described in Section 3.3.2.

3.3.1 The Sub-Domain Electric Current Density Basis Function

The electric current density distribution for each of the sub-domain basis functions is defined over the bi-triangular patch sub-domain element of that function and zero elsewhere in the analysis cell. The electric current on the n^{th} sub-element flows radially from the vertex $\overline{\rho}_{n3}$, increasing linearly in density with distance from this vertex, flows across the edge, and decreases linearly in density while flowing radially into the other outside vertex, $\overline{\rho}_{n4}$. The electric current density inside the basis function over the

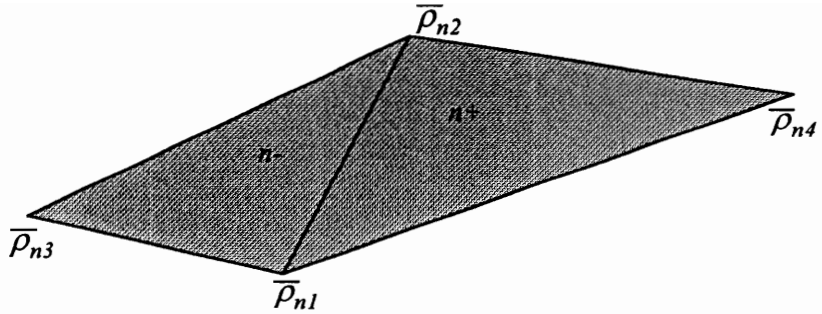

Figure 3.1. Geometry of the bi-triangular patch sub-domain basis function.

triangle which contains $\overline{\rho}_{n3}$ is given by

$$\overline{J}_{n-}(\overline{\rho}) = \frac{|\overline{\rho}_{n2} - \overline{\rho}_{n1}|}{\widehat{z} \cdot (\overline{\rho}_{n1} - \overline{\rho}_{n3}) \times (\overline{\rho}_{n2} - \overline{\rho}_{n1})} (\overline{\rho} - \overline{\rho}_{n3})\, J_n = J_n\, \overline{\overline{j}}_{n-}(\overline{\rho}) \qquad (3.5a)$$

and over the triangle which contains $\overline{\rho}_{n4}$ by

$$\overline{J}_{n+}(\overline{\rho}) = \frac{|\overline{\rho}_{n2} - \overline{\rho}_{n1}|}{\widehat{z} \cdot (\overline{\rho}_{n1} - \overline{\rho}_{n4}) \times (\overline{\rho}_{n2} - \overline{\rho}_{n1})} (\overline{\rho} - \overline{\rho}_{n4})\, J_n = J_n\, \overline{\overline{j}}_{n+}(\overline{\rho}) \qquad (3.5b)$$

where J_n is the weight of the electric current density at the joining edge of the $n^{\underline{th}}$ sub-domain element and $\overline{\rho}$ is the vector from the coordinate origin to a point in the $n^{\underline{th}}$ sub-domain element. The electric current density for the $n^{\underline{th}}$ electric current density function is zero over the analysis cell outside the bi-triangular basis function area. The direction and density of the electric current flowing on the $n^{\underline{th}}$ bi-triangular sub-domain element are shown in Figure 3.2.

The dotted rooftop shape above the bi-triangular sub-domain element shows the electric current density from the basis function description of (3.5). The radially directed electric current flowing from and into the two external vertices of the bi-triangular sub-domain element, $\overline{\rho}_{n3}$ and $\overline{\rho}_{n4}$, is shown by the thin arrow lines connecting these external vertices to the joining edge, $(\overline{\rho}_{n1}, \overline{\rho}_{n2})$, of the bi-triangular sub-domain element patch.

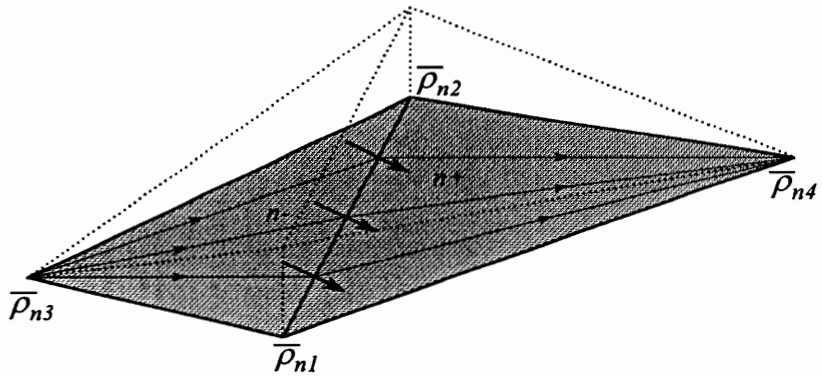

Figure 3.2. Geometry of the bi-triangular patch sub-domain basis function showing the density and direction of the electric current as defined by (3.5). The magnitude of the electric current density is shown by the dotted rooftop structure. The direction of the electric current is shown by the thin arrows. The uniform electric current flowing across the joining edge is shown by the heavy arrows.

The heavier arrows on the joining edge of the bi-triangular sub-domain element patch show the direction and density of the electric current flowing across this edge, specifically the electric current density component normal to the joining edge.

As shown in Figure 3.2, the electric current density description used for the sub-domain basis function set results in a constant electric current of density J_n flowing across the joining edge of the bi-triangular patch sub-domain element. This electric current flows perpendicular to the joining edge of the triangles. The total electric current density for the $n^{\underline{th}}$ bi-triangular patch sub-domain element is given by

$$\overline{J}_n(\rho) = \begin{cases} \overline{J}_{n-}(\overline{\rho}) \text{ over } n\text{-} \\ \overline{J}_{n+}(\overline{\rho}) \text{ over } n\text{+} \end{cases} . \tag{3.6}$$

Substituting (3.5) into (3.6) and evaluating just off the joining edge in the half of the bi-triangular patch sub-domain element which contains $\overline{\rho}_{n3}$ gives

$$\overline{J}_n\Big|_{edge} = \overline{J}_{n-}(\overline{\rho}) = |\overline{\rho}_{n2} - \overline{\rho}_{n1}|\, J_n \frac{(\overline{\rho} - \overline{\rho}_{n3})}{\widehat{z} \cdot (\overline{\rho}_{n1} - \overline{\rho}_{n3}) \times (\overline{\rho}_{n2} - \overline{\rho}_{n1})} \tag{3.7a}$$

and in the half of the bi-triangular patch sub-domain element which contains $\overline{\rho}_{n4}$ gives

$$\overline{J}_n\Big|_{edge} = \overline{J}_{n+}(\overline{\rho}) = |\overline{\rho}_{n2} - \overline{\rho}_{n1}|\, J_n \frac{(\overline{\rho} - \overline{\rho}_{n4})}{\widehat{z} \cdot (\overline{\rho}_{n1} - \overline{\rho}_{n4}) \times (\overline{\rho}_{n2} - \overline{\rho}_{n1})}. \tag{3.7b}$$

The vector to a point on the joining edge of the bi-triangular sub-domain element, $(\overline{\rho}_{n1}, \overline{\rho}_{n2})$, is given by

$$\overline{\rho} = (\overline{\rho}_{n2} - \overline{\rho}_{n1})\, s + \overline{\rho}_{n1} \tag{3.8}$$

where s is the distance along the joining edge from $\overline{\rho}_{n1}$ to $\overline{\rho}_{n2}$. Substituting (3.8) into (3.7a) and (3.7b) gives the current flowing across the joining edge in terms of the location along the joining edge as

$$\overline{J}_{n-}(s) = |\overline{\rho}_{n2} - \overline{\rho}_{n1}|\, J_n \frac{(\overline{\rho}_{n2} - \overline{\rho}_{n1})\, s + \overline{\rho}_{n1} - \overline{\rho}_{n3}}{\widehat{z} \cdot (\overline{\rho}_{n1} - \overline{\rho}_{n3}) \times (\overline{\rho}_{n2} - \overline{\rho}_{n1})} \tag{3.9a}$$

and

$$\overline{J}_{n+}(s) = |\overline{\rho}_{n2} - \overline{\rho}_{n1}|\, J_n \frac{(\overline{\rho}_{n2} - \overline{\rho}_{n1})\, s + \overline{\rho}_{n1} - \overline{\rho}_{n4}}{\widehat{z} \cdot (\overline{\rho}_{n1} - \overline{\rho}_{n4}) \times (\overline{\rho}_{n2} - \overline{\rho}_{n1})}. \tag{3.9b}$$

The current which is flowing across this edge can now be found from

$$J_{n_\perp}(s) = \frac{-1}{|\overline{\rho}_{n2} - \overline{\rho}_{n1}|} \widehat{z} \cdot (\overline{\rho}_{n2} - \overline{\rho}_{n1}) \times \overline{J}_n(s). \tag{3.10}$$

Substituting (3.9a) and (3.9b) into (3.10) gives

$$J_{n-_\perp}(s) = \left(\frac{-\widehat{z} \cdot (\overline{\rho}_{n2} - \overline{\rho}_{n1}) \times (\overline{\rho}_{n2} - \overline{\rho}_{n1})\, s}{\widehat{z} \cdot (\overline{\rho}_{n1} - \overline{\rho}_{n3}) \times (\overline{\rho}_{n2} - \overline{\rho}_{n1})} - \frac{\widehat{z} \cdot (\overline{\rho}_{n2} - \overline{\rho}_{n1}) \times (\overline{\rho}_{n1} - \overline{\rho}_{n3})}{\widehat{z} \cdot (\overline{\rho}_{n1} - \overline{\rho}_{n3}) \times (\overline{\rho}_{n2} - \overline{\rho}_{n1})} \right) J_n \tag{3.11a}$$

and

$$J_{n+_\perp}(s) = \left(\frac{-\hat{z} \cdot (\overline{\rho}_{n2} - \overline{\rho}_{n1}) \times (\overline{\rho}_{n2} - \overline{\rho}_{n1})\, s}{\hat{z} \cdot (\overline{\rho}_{n1} - \overline{\rho}_{n4}) \times (\overline{\rho}_{n2} - \overline{\rho}_{n1})} - \frac{\hat{z} \cdot (\overline{\rho}_{n2} - \overline{\rho}_{n1}) \times (\overline{\rho}_{n1} - \overline{\rho}_{n4})}{\hat{z} \cdot (\overline{\rho}_{n1} - \overline{\rho}_{n4}) \times (\overline{\rho}_{n2} - \overline{\rho}_{n1})} \right) J_n. \tag{3.11b}$$

The first terms in each of these equations, (3.11), can be removed because

$$(\overline{\rho}_{n2} - \overline{\rho}_{n1}) \times (\overline{\rho}_{n2} - \overline{\rho}_{n1}) \equiv 0. \tag{3.12}$$

This simplification give the results

$$J_{n-_\perp}(s) = \frac{-\hat{z} \cdot (\overline{\rho}_{n2} - \overline{\rho}_{n1}) \times (\overline{\rho}_{n1} - \overline{\rho}_{n3})}{\hat{z} \cdot (\overline{\rho}_{n1} - \overline{\rho}_{n3}) \times (\overline{\rho}_{n2} - \overline{\rho}_{n1})} J_n = J_n \tag{3.13a}$$

and

$$J_{n+_\perp}(s) = \frac{-\hat{z} \cdot (\overline{\rho}_{n2} - \overline{\rho}_{n1}) \times (\overline{\rho}_{n1} - \overline{\rho}_{n4})}{\hat{z} \cdot (\overline{\rho}_{n1} - \overline{\rho}_{n4}) \times (\overline{\rho}_{n2} - \overline{\rho}_{n1})} J_n = J_n \tag{3.13b}$$

since

$$\overline{A} \times \overline{B} = -\overline{B} \times \overline{A}. \tag{3.14}$$

So the current which crosses the joining edge of the bi-triangular patch sub-domain element is of uniform density J_n.

3.3.2 The Sub-domain Electric Potential Testing Function

The electric potential testing function for the MoM analysis is defined over each of the bi-triangular sub-domain basis functions as a pulse-weighted integral over the electric field between the centroids of each of the triangles. This pulse testing function is accomplished by integrating the electric field from the centroid of the triangle which contains $\overline{\rho}_{n3}$, located at $\overline{c}_{n-}$, to the center of the joining edge, located at $\overline{b}_n$, to the centroid of the triangle which contains $\overline{\rho}_{n4}$, located at $\overline{c}_{n+}$. The electric potential testing

function for the $n^{\underline{th}}$ bi-triangular sub-domain element is shown in Figure 3.3. The vector from the cooridinate origin to the centroids of the triangular halves of the bi-triangular patch sub-domain element are found from basic plane geometry as

$$\bar{c}_{n-} = \frac{\bar{\rho}_{n1} + \bar{\rho}_{n2} + \bar{\rho}_{n3}}{3} \tag{3.15a}$$

and

$$\bar{c}_{n+} = \frac{\bar{\rho}_{n1} + \bar{\rho}_{n2} + \bar{\rho}_{n4}}{3}. \tag{3.15b}$$

The vector to the center of the joining edge of the two halves of the bi-triangular sub-domain element is given by

$$\bar{b}_n = \frac{\bar{\rho}_{n1} + \bar{\rho}_{n2}}{2}. \tag{3.16}$$

Using these definitions, the pulse weighted integral which defines the testing function on the $n^{\underline{th}}$ sub-domain element is

$$V_n = -\int_{\bar{c}_{n-}}^{\bar{b}_n} \overline{E}(\bar{\rho}) \cdot \mathrm{d}\bar{l}_1 - \int_{\bar{b}_n}^{\bar{c}_{n+}} \overline{E}(\bar{\rho}) \cdot \mathrm{d}\bar{l}_2 \tag{3.17}$$

where $\overline{E}(\bar{\rho})$ is the electric field in the analysis cell at the air/dielectric interface and $\bar{l}_1$ and $\bar{l}_2$ are the two portions of the integration path as shown in Figure 3.3.

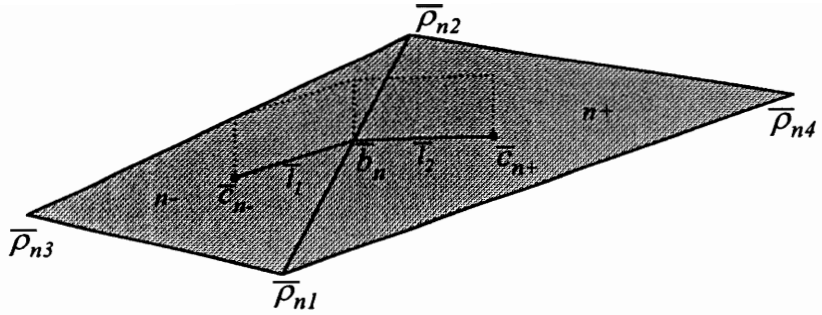

Figure 3.3. Geometry of the bi-triangular patch sub-domain basis function showing the weight and integration path of the electric potential testing function defined by (3.21). The weighting of the electric field in the integral is shown by the dotted ridge the integration path shown by the solid line.

3.4 Electromagnetic Field Description

The electromagnetic fields in the analysis cell can be expanded in a weighted series of $TE^{(z)}$ and $TM^{(z)}$ Floquet modes where the (z) superscript indicates that the modes are transverse with respect to the z-axis. As will be discussed in Section 3.4.2, the Floquet expansion of the fields is derived from the ideal array material which was presented in Section 2.1.1. The expansion of the electromagnetic fields in the analysis cell in Floquet modes allows the effects of the full infinite array to be included in the analysis of a single cell of the array.

The definition of the analysis cell geometry used in this work is described in Section 3.4.1. The definition of the beam scanning angle and the phase progression which is required across the analysis cell to generate an array beam at this angle are presented in this section. The Floquet expansion of the electromagnetic fields in the analysis cell is presented in Section 3.4.2. The field expansion is developed from the choice of potential function used to generate the mode description for the general case $TE^{(z)}$ and $TM^{(z)}$

modes and the TEM$^{(z)}$ special case. Finally, the ability of this Floquet mode representation to properly represent the electromagnetic fields in the analysis cell will be discussed.

3.4.1 The Floquet Analysis Cell

The geometry of the Floquet analysis cell is shown in Figure 3.4. This analysis cell is defined to be a rectangular cell of dimension a in the x-direction and b in the y-direction. The analysis cell is bounded at the $z = -d$ plane by a perfect electric conducting ground plane. The unbounded upper portion of the cell is treated as free space in the analysis. The coordinate origin is located on the air/dielectric interface at the center of the rectangular analysis cell. The dielectric slab of thickness d which lies on the ground plane has a relative permittivity of ϵ_r which may be complex to allow dielectric loss effects to be considered. The direction of the desired scanned array beam is determined as shown in Figure 3.4. This direction is specified by the angle from the $+z$-axis, θ_o, and the angle from the $+x$-axis toward the $+y$-axis generated by the projection of the scan direction to the xy-plane, ϕ_o.

As discussed in Section 2.1.1, an interelement phase shift of

$$\Phi = k_o \, s \sin\theta_o \tag{3.18}$$

where k_o is the free-space wavenumber and s is the interelement spacing of the linear array is required for a linear array to generate a beam in the θ_o direction. This result can

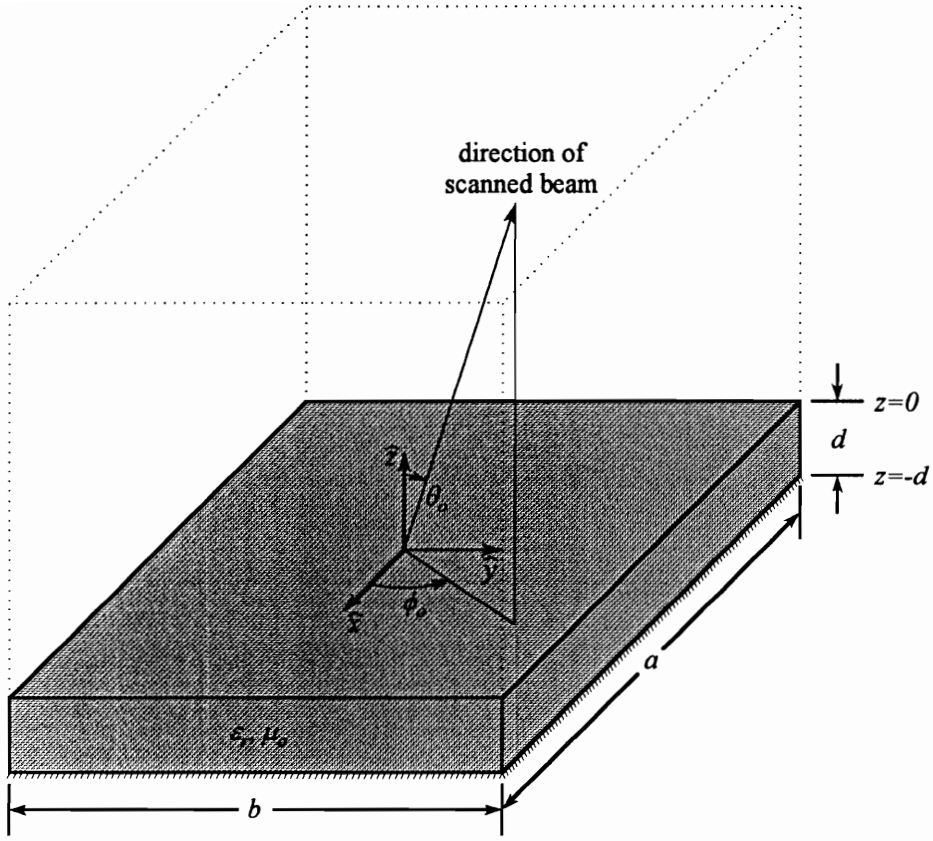

Figure 3.4. Floquet Analysis cell geometry showing the coordinate system and the definition of the angles for a scanned beam.

be expanded for a planar array to

$$\Phi_x = k_o \, s_x \sin\theta_o \cos\phi_o \tag{3.19a}$$

in the x-direction and

$$\Phi_y = k_o \, s_y \sin\theta_o \sin\phi_o \tag{3.19b}$$

in the y-direction where s_x and s_y are the interelement spacings in the x- and y-directions. This interelement phase shift is the basis for the Floquet mode expansion of the electromagnetic fields. The phase shifts given by (3.19) are the boundary conditions required for the side walls of the analysis cell to ensure the phase shift between adjacent

point elements in the ideal array is identical to the phase shift between the identical points in any two adjacent cells for the full infinite array analysis.

Expressing (3.19) in vector wavenumber form as

$$\overline{k}_{\rho 00} = \hat{x}\overline{k}_{x_0} + \hat{y}\overline{k}_{y_0} = \hat{x}k_o \sin\theta_o \cos\phi_o + \hat{y}k_o \sin\theta_o \sin\phi_o \tag{3.20}$$

gives the required transverse wavenumber for the base mode in the Floquet analysis cell [1]. Unless grating lobes are present in real space, only this base mode is used in the case of an ideal array where the effects of coupling between the elements are ignored. The use of the full Floquet expansion of the electromagnetic fields in the cell leads to a mode structure which is similar to a Fourier expansion. The ρ-directed wavenumbers for the Floquet expansion are given by

$$\overline{k}_{\rho_{pq}} = \hat{x}\left(k_o \sin\theta_o \cos\phi_o + \frac{2\pi p}{a}\right) + \hat{y}\left(k_o \sin\theta_o \sin\phi_o + \frac{2\pi q}{b}\right), \tag{3.21}$$

where $\overline{k}_{\rho_{pq}}$ is the wavenumber in the plane of the array face for the $pq^{\underline{th}}$ mode, which is analogous to a two-dimensional Fourier expansion with added phase progression terms. It is also interesting to note that the form of the Floquet expansion is similar to the standard TE and TM modes in rectangular waveguide but contains only the modes which would be the $TE_{2p\,2q}$ and $TM_{2p\,2q}$ modes in the rectangular waveguide structure. This difference is required by the presence of side walls which require a constant phase shift plus an integer number of full-wave progressions between the side walls rather than conducting side walls which require only half-wave progressions to establish the required electric field nulls.

The full wavenumber for each mode also requires a z-component. This component of the wavenumber is determined from the relationship

$$\sqrt{k_x^2 + k_y^2 + k_z^2} = k. \tag{3.22}$$

For the air region of the analysis cell above the air/dielectric interface, the z-directed wavenumber for the $pq^{\underline{th}}$ mode is

$$k_{z_{pq}}^{(+)} = \sqrt{k_o^2 - \overline{k}_{\rho_{pq}} \cdot \overline{k}_{\rho_{pq}}} \tag{3.23}$$

where the $(+)$ superscript indicates the air region. The full vector wavenumber in the air region is then

$$\overline{k}_{pq}^{(+)} = \overline{k}_{\rho_{pq}} + k_{z_{pq}}^{(+)}\hat{z}. \tag{3.24}$$

Similarly, for the dielectric region of the analysis cell, the z-directed wavenumber for the $pq^{\underline{th}}$ mode is

$$\overline{k}_{z_{pq}}^{(d)} = \sqrt{\epsilon_r k_o^2 - \overline{k}_{\rho_{pq}} \cdot \overline{k}_{\rho_{pq}}} \tag{3.25}$$

where the (d) superscript indicates the dielectric region and ϵ_r is the relative permittivity of the dielectric. The full vector wavenumber for the dielectric region is

$$\overline{k}_{pq}^{(d)} = \overline{k}_{\rho_{pq}} + k_{z_{pq}}^{(d)}\hat{z}. \tag{3.26}$$

It is important to note that the vector wavenumbers in the air and dielectric regions are identical except for the z-component. This relationship is critical to the satisfaction of the tangential electric field boundary condition presented in Section 3.6.

3.4.2 The Modal Field Description

The $\text{TE}^{(z)}$, $\text{TM}^{(z)}$, and $\text{TEM}^{(z)}$ mode electromagnetic fields in the Floquet analysis cell are derived from potential functions which satisfy the requirements discussed in the previous section. These potential functions must also satisfy the boundary conditions at the other two boundaries of the cell: the PEC ground plane at $z = -d$ and bounded

fields at $z = +\infty$. The potential functions are developed separately for the two distinct regions in the analysis cell, air and dielectric. The air region of the analysis cell requires three potential function forms: one for the $TE^{(z)}$ and $TM^{(z)}$ modes and two for the $TEM^{(z)}$ modes, which are developed as special cases of the $TM^{(z)}$ modes here. The field expansion in the dielectric region of the analysis cell is more complicated because of the presence of the PEC ground plane. The dielectric region requires a separate potential function for the $TE^{(z)}$ and for the $TM^{(z)}$ modes as well as another pair of potential function for the $TEM^{(z)}$ modes.

The $TE^{(z)}$ and $TM^{(z)}$ potential function form for the air filled region above the air/dielectric interface is

$$\Psi_{pq}^{(TE+,TM+)} = \mathrm{e}^{-j\bar{k}_{pq}^{(+)}\cdot\bar{r}} \tag{3.27}$$

where $\bar{r}$ is a position vector for any location in the air region of the Floquet analysis cell. The $TM^{(z)}$ modes can now be found from

$$\bar{h}_{pq}^{(TM)} = \nabla \times \hat{z}\Psi_{pq}(\bar{r}) \tag{3.28a}$$

for the magnetic field and

$$\bar{e}_{pq}^{(TM)} = \frac{1}{j\omega\epsilon}\nabla \times h_{pq}^{(TM)} = \frac{1}{j\omega\epsilon}\nabla \times \nabla \times \hat{z}\Psi_{pq} \tag{3.28b}$$

for the electric field. Substituting (3.27) into (3.28) gives the magnetic and electric fields for the $pq^{\underline{th}}$ $TM^{(z)}$ mode in the air region as

$$\bar{h}_{pq}^{(TM+)} = -j\left(k_{y_q}\,\hat{x} - k_{x_p}\,\hat{y}\right)\mathrm{e}^{-j\bar{k}_{pq}^{(+)}\cdot\bar{r}} \tag{3.29a}$$

and

$$\bar{e}_{pq}^{(TM+)} = \frac{-1}{j\omega\epsilon_o}\left[k_{z_{pq}}^{(+)}\left(k_{x_p}\,\hat{x} + k_{y_q}\,\hat{y}\right) + \left(k_{z_{pq}}^{(+)^2} - k_o^2\right)\hat{z}\right] \mathrm{e}^{-j\bar{k}_{pq}^{(+)}\cdot\bar{r}}. \tag{3.29b}$$

The TE$^{(z)}$ modes are found from

$$\bar{e}_{pq}^{(TE)} = -\nabla \times \hat{z}\Psi_{pq} \tag{3.30a}$$

for the electric field and

$$\bar{h}_{pq}^{(TE)} = \frac{-1}{j\omega\mu}\nabla \times \bar{e}_{pq}^{(TE)} = \frac{1}{j\omega\mu}\nabla \times \nabla \times \hat{z}\Psi_{pq} \tag{3.30b}$$

for the magnetic field. Substituting (3.27) into (3.30) gives the electric and magnetic fields for the $pq^{\underline{th}}$ TE$^{(z)}$ mode in the air region as

$$\bar{e}_{pq}^{(TE+)}(\bar{r}) = j\left(k_{y_q}\,\hat{x} - k_{x_p}\,\hat{y}\right) \mathrm{e}^{-j\bar{k}_{pq}^{(+)}\cdot\bar{r}} \tag{3.31a}$$

and

$$\bar{h}_{pq}^{(TE+)} = \frac{-1}{j\omega\mu_o}\left[k_{z_{pq}}^{(+)}\left(k_{x_p}\,\hat{x} + k_{y_q}\,\hat{y}\right) + \left(k_{z_{pq}}^{(+)^2} - k_o^2\right)\hat{z}\right] \mathrm{e}^{-j\bar{k}_{pq}^{(+)}\cdot\bar{r}}. \tag{3.31b}$$

The TEM$^{(z)}$ modes in the air region require two potential functions in order to account for the two components of the TEM$^{(z)}$ field. These potential functions are chosen to provide two TEM$^{(z)}$ modes which are orthogonal. The potential functions are given by

$$\Psi^{(TEM_x+)} = x\mathrm{e}^{-j\,k_o\,z} \tag{3.32a}$$

for the x-directed TEM$^{(z)}$ electric field component and

$$\Psi^{(TEM_y+)} = y e^{-j k_o z} \tag{3.32b}$$

for the y-directed TEM$^{(z)}$ electric field component. The magnetic and electric fields which result from these potential functions are found by substituting (3.32) into (3.28) using a magnetic vector potential form. This substitution gives

$$\overline{h}_{pq}^{(TEM_x+)} = -\hat{y} e^{-jk_o z} \tag{3.33a}$$

and

$$\overline{e}_{pq}^{(TEM_x+)} = \frac{-k_o}{\omega \epsilon_o} \hat{x} e^{-jk_o z} \tag{3.33b}$$

for the x-directed electric field mode and

$$\overline{h}_{pq}^{(TEM_y+)} = \hat{x} e^{-jk_o z} \tag{3.34a}$$

and

$$\overline{e}_{pq}^{(TEM_y+)} = \frac{-k_o}{\omega \epsilon_o} \hat{y} e^{-jk_o z} \tag{3.34b}$$

for the y-directed electric field mode.

The dielectric filled region below the air/dielectric interface requires two different potential functions for the TE$^{(z)}$ and TM$^{(z)}$ modes. Each of these two potential functions must be chosen to force the tangential electric field to zero at the $z = -d$ PEC ground plane. The potential function for the TM$^{(z)}$ modes in the dielectric is

$$\Psi_{pq}^{(TMd)} = e^{-j\overline{k}_{pq}^{(d)} \cdot \overline{\rho}} \cos\left[k_{z_{pq}}^{(d)}(z+d)\right]. \tag{3.35}$$

Substituting (3.35) into (3.28) gives the $TM^{(z)}$ mode magnetic and electric fields in the dielectric region as

$$\overline{h}_{pq}^{(TMd)} = -j\left(k_{y_q}\,\hat{x} - k_{x_p}\,\hat{y}\right) e^{-j\overline{k}_{pq}^{(d)}\cdot\overline{\rho}} \cos\left[k_{z_{pq}}^{(d)}(z+d)\right] \tag{3.36a}$$

and

$$\overline{e}_{pq}^{(TMd)} = \frac{1}{j\omega\epsilon_o\epsilon_r}\left[jk_{z_{pq}}^{(d)}\left(k_{x_p}\,\hat{x} + k_{y_q}\,\hat{y}\right)\sin\left[k_{z_{pq}}^{(d)}(z+d)\right] + \left(\epsilon_r k_o^2 - k_{z_{pq}}^{(d)^2}\right)\cos\left[k_{z_{pq}}^{(d)}(z+d)\right]\hat{z}\right] e^{-j\overline{k}_{pq}^{(d)}\cdot\overline{\rho}} \tag{3.36b}$$

which satisfies the requirement of zero tangential electric field at the ground plane since

$$\sin\left[k_{z_{pq}}^{(d)}(z+d)\right]\Big|_{z=-d} = 0. \tag{3.37}$$

The potential function for the $TE^{(z)}$ modes in the dielectric is

$$\Psi_{pq}^{(TEd)} = e^{-j\overline{k}_{pq}^{(d)}\cdot\overline{\rho}} \sin\left[k_{z_{pq}}^{(d)}(z+d)\right]. \tag{3.38}$$

Substituting (3.38) into (3.30) gives the $TE^{(z)}$ mode electric and magnetic fields in the dielectric region as

$$\overline{e}_{pq}^{(TEd)} = j\left(k_{y_q}\,\hat{x} - k_{x_p}\,\hat{y}\right) e^{-j\overline{k}_{pq}^{(d)}\cdot\overline{\rho}} \sin\left[k_{z_{pq}}^{(d)}(z+d)\right] \tag{3.39a}$$

and

$$\overline{h}_{pq}^{(TEd)} = \frac{1}{j\omega\mu_o}\left[-jk_{z_{pq}}^{(d)}\left(k_{x_p}\,\hat{x} + k_{y_q}\,\hat{y}\right)\cos\left[k_{z_{pq}}^{(d)}(z+d)\right] + \left(\epsilon_r k_o^2 - k_{z_{pq}}^{(d)^2}\right)\sin\left[k_{z_{pq}}^{(d)}(z+d)\right]\hat{z}\right] e^{-j\overline{k}_{pq}^{(d)}\cdot\overline{\rho}}. \tag{3.39b}$$

This choice for the $TE^{(z)}$ modes also satisfies the tangential electric field boundary condition at the PEC ground plane.

The TEM$^{(z)}$ modes in the dielectric filled region require two potential functions as did the TEM$^{(z)}$ modes in the air region. Again, the two potential functions are chosen to account for the two x- and y-directed components of the TEM$^{(z)}$ electromagnetic fields based on a magnetic vector potential form. The potential functions chosen for the TEM$^{(z)}$ modes in the dielectric region must additionally enforce the boundary condition of zero tangential electric field at the PEC ground plane at $z = -d$. The potential functions for the TEM$^{(z)}$ modes in the dielectric are

$$\Psi^{(TEM_x d)} = x \cos\left[\sqrt{\epsilon_r}\, k_o (z+d)\right] \tag{3.40a}$$

for the x-directed TEM$^{(z)}$ electric field component and

$$\Psi^{(TEM_y d)} = y \cos\left[\sqrt{\epsilon_r}\, k_o (z+d)\right] \tag{3.40b}$$

for the y-directed TEM$^{(z)}$ electric field component. The magnetic and electric fields which result from these potential functions are found by substituting (3.40) into (3.28). This substitution gives

$$\overline{h}_{pq}^{(TEM_x d)} = -\hat{y} \cos\left[\sqrt{\epsilon_r}\, k_o (z+d)\right] \tag{3.41a}$$

and

$$\overline{e}_{pq}^{(TEM_x d)} = \frac{-k_o}{j\omega\epsilon_o\sqrt{\epsilon_r}}\, \hat{x} \sin\left[\sqrt{\epsilon_r}\, k_o (z+d)\right] \tag{3.41b}$$

for the x-directed electric field TEM$^{(z)}$mode in the dielectric and

$$\overline{h}_{pq}^{(TEM_y d)} = \hat{x} \cos\left[\sqrt{\epsilon_r}\, k_o (z+d)\right] \tag{3.42a}$$

and

$$\overline{e}_{pq}^{(TEM_y d)} = \frac{-k_o}{j\omega\epsilon_o\sqrt{\epsilon_r}}\hat{y}\sin\left[\sqrt{\epsilon_r}k_o(z+d)\right] \tag{3.42b}$$

for the y-directed electric field TEM$^{(z)}$mode in the dielectric. As for the TE$^{(z)}$ and TM$^{(z)}$ modes in the dielectric, these choices for the TEM$^{(z)}$ mode fields in the dielectric region satisfy the zero tangential electric field boundary condition at the PEC ground plane because of the $\sin\left[\sqrt{\epsilon_r}k_o(z+d)\right]$ term in both of the electric field expressions.

The complete description of the electromagnetic fields in each region of the Floquet analysis cell is a weighted sum of the TE$^{(z)}$ and TM$^{(z)}$ mode fields in that region. The TEM$^{(z)}$ mode fields represent special cases of the TM$^{(z)}$ modes and are substituted for the general mode field description if the mode is TEM. The electric field described by the weighted sum of modes for the air region of the analysis cell is

$$\overline{E}^{(+)}(\overline{\rho}) = \sum_{p=-\infty}^{\infty}\sum_{q=-\infty}^{\infty}\left(A_{pq}^{(+)}\overline{e}_{pq}^{(TM+)} + B_{pq}^{(+)}\overline{e}_{pq}^{(TE+)}\right) \tag{3.43a}$$

where $A_{pq}^{(+)}$ and $B_{pq}^{(+)}$ are the weights of the TM$^{(z)}$ and TE$^{(z)}$ modes in the air region of the Floquet analysis cell. Similarly, the magnetic field in the air region of the analysis cell is given by

$$\overline{H}^{(+)}(\overline{\rho}) = \sum_{p=-\infty}^{\infty}\sum_{q=-\infty}^{\infty}\left(A_{pq}^{(+)}\overline{h}_{pq}^{(TM+)} + B_{pq}^{(+)}\overline{h}_{pq}^{(TE+)}\right). \tag{3.43b}$$

The electric and magnetic fields in the dielectric region of the analysis cell are given by

$$\overline{E}^{(d)}(\overline{\rho}) = \sum_{p=-\infty}^{\infty}\sum_{q=-\infty}^{\infty}\left(A_{pq}^{(d)}\overline{e}_{pq}^{(TMd)} + B_{pq}^{(d)}\overline{e}_{pq}^{(TEd)}\right) \tag{3.44a}$$

and

$$\overline{H}^{(d)}(\overline{\rho}) = \sum_{p=-\infty}^{\infty} \sum_{q=-\infty}^{\infty} \left(A_{pq}^{(d)} \overline{h}_{pq}^{(TMd)} + B_{pq}^{(d)} \overline{h}_{pq}^{(TEd)} \right) \tag{3.44b}$$

where $A_{pq}^{(d)}$ and $B_{pq}^{(d)}$ are the mode weights for the $TM^{(z)}$ and $TE^{(z)}$ modes in the dielectric region of the Floquet analysis cell.

The ability of a Floquet series of $TE^{(z)}$ and $TM^{(z)}$ modes to describe the electromagnetic fields in the analysis cell is based on two distinct principles. First, the Floquet series must converge over the region of the analysis cell as the number of modes included in the series approaches infinity. This property of the Floquet sequence will not be discussed except to note that the Floquet series is based on the Fourier series which is well known to be suitably convergent [12]. The only difference between these two series is the inclusion of a fixed phase taper in the Floquet series which is not usually included in the Fourier series. Second, the $TE^{(z)}$ and $TM^{(z)}$ modes chosen must be able to represent the arbitrary electromagnetic field of the *pq* mode of the Floquet series. This requirement is more central to the discussion and will be demonstrated.

An arbitrary electromagnetic field in three dimensions has only two independent components because all electromagnetic fields must satisfy Gauss' Law,

$$\nabla \cdot \epsilon \overline{E} = \rho_e \tag{3.45}$$

where ρ_e is the electric charge density. The existence of only two independent components of an arbitrary electromagnetic field allows the field to be represented by any combination of two independent electromagnetic fields which are valid over the region in which the arbitrary field exists. The ability of $TE^{(z)}$ and $TM^{(z)}$ Floquet modes to describe an arbitrary Floquet mode electromagnetic field can be demonstrated by showing that the $TE^{(z)}$ Floquet mode is independent of the $TM^{(z)}$ Floquet mode. The independence of the

$TE^{(z)}$ and $TM^{(z)}$ Floquet modes can be shown by considering the inner products of the electric and magnetic fields of the $TE^{(z)}$ and $TM^{(z)}$ Floquet modes [36].

The inner product of the electromagnetic fields of the $TE^{(z)}$ and $TM^{(z)}$ modes in the Floquet analysis cell for the electric fields is given by

$$\int\int \overline{e}^{(TM)} \cdot \overline{e}^{(TE)^*} \mathrm{d}s \tag{3.46a}$$

and for the magnetic fields by

$$\int\int \overline{h}^{(TM)} \cdot \overline{h}^{(TE)^*} \mathrm{d}s \tag{3.46b}$$

where the integration is performed over any xy-plane in the analysis cell. Substituting (3.28b) and (3.30a) into (3.46a) to find the electric field inner product,

$$\int\int \overline{e}^{(TM)} \cdot \overline{e}^{(TE)^*} \mathrm{d}s = \int\int \left(\frac{1}{j\omega\epsilon} \nabla \times \nabla \times \hat{z}\Psi_e \right) \cdot \left(- \nabla \times \hat{z}\Psi_h \right)^* \mathrm{d}s \tag{3.47}$$

which can be modified to

$$\int\int \overline{e}^{(TM)} \cdot \overline{e}^{(TE)^*} \mathrm{d}s = \frac{-1}{j\omega\epsilon} \int\int (\nabla \times \hat{z} \times \nabla\Psi_e) \cdot (\hat{z} \times \nabla\Psi_h)^* \mathrm{d}s \tag{3.48}$$

by using the vector identity

$$\nabla \times (u\overline{A}) = u\nabla \times \overline{A} - \overline{A} \times \nabla u. \tag{3.49}$$

Using the vector identity

$$\nabla \times (\overline{A} \times \overline{B}) = (\overline{B} \cdot \nabla)\overline{A} - \overline{B}(\nabla \cdot \overline{A}) - (\overline{A} \cdot \nabla)\overline{B} + \overline{A}(\nabla \cdot \overline{B}), \tag{3.50}$$

equation (3.48) can be rewritten as

$$\begin{aligned} \int\int \overline{e}^{(TM)} \cdot \overline{e}^{(TE)^*} \mathrm{d}s = \frac{-1}{j\omega\epsilon} \int\int \Big[& (\nabla\Psi_e \cdot \nabla)\hat{z} - \nabla\Psi_e(\nabla \cdot \hat{z}) \\ & - (\hat{z} \cdot \nabla)\nabla\Psi_e + \hat{z}(\nabla \cdot \nabla\Psi_e) \Big] \cdot (\hat{z} \times \nabla\Psi_h)^* \mathrm{d}s \end{aligned} \tag{3.51}$$

or

$$\int\int \overline{e}^{(TM)} \cdot \overline{e}^{(TE)^*} \mathrm{d}s = \frac{1}{j\omega\epsilon} \int\int \nabla \frac{\partial}{\partial z} \Psi_h \cdot (\hat{z} \times \nabla \Psi_h)^* \mathrm{d}s \tag{3.52}$$

since

$$\begin{aligned} &(\nabla \overline{A} \cdot \nabla)\hat{z} = 0, \\ &(\nabla \cdot \hat{z}) = 0, \\ &(\hat{z} \cdot \nabla) = \frac{\partial}{\partial z}, \text{ and} \\ &\hat{z}\overline{A} \cdot (\hat{z} \times \overline{B}) = 0. \end{aligned} \tag{3.53}$$

All Floquet modes have potential functions of the form

$$\Psi = \mathrm{e}^{-j\overline{k}_{\rho pq} \cdot \overline{\rho}} f(z) \tag{3.54}$$

for the $pq^{\underline{th}}$ mode where $\overline{k}_{\rho pq} = \hat{x}\left(k_o \sin\theta_o \cos\phi_o + \frac{2\pi p}{a}\right) + \hat{y}\left(k_o \sin\theta_o \sin\phi_o + \frac{2\pi q}{b}\right)$ is the transverse wavenumber required for the mode to be a valid Floquet mode [1]. Setting

$$\Psi_h = \mathrm{e}^{-j\overline{k}_{\rho pq} \cdot \overline{\rho}} f(z) \tag{3.55}$$

and

$$\Psi_e = \mathrm{e}^{-j\overline{k}_{\rho rs} \cdot \overline{\rho}} g(z) \tag{3.56}$$

and substituting (3.55) and (3.56) into (3.52) gives

$$\begin{aligned} \int\int \overline{e}^{(TM)} \cdot \overline{e}^{(TE)^*} \mathrm{d}s = \frac{1}{j\omega\epsilon} \int\int \nabla \frac{\partial}{\partial z} \mathrm{e}^{-j\overline{k}_{\rho pq} \cdot \overline{\rho}} f(z) \cdot \\ \left(\hat{z} \times \nabla \mathrm{e}^{j\overline{k}_{\rho rs} \cdot \overline{\rho}} g^*(z)\right) \mathrm{d}s. \end{aligned} \tag{3.57}$$

After evaluation, (3.57) simplifies to

$$\int\int \overline{e}^{(TM)} \cdot \overline{e}^{(TE)^*} \mathrm{d}s = \frac{\frac{\partial f(z)}{\partial z} g^*(z)}{j\omega\epsilon} \int\int \mathrm{e}^{j(\overline{k}_{\rho rs} - \overline{k}_{\rho pq}) \cdot \overline{\rho}} \overline{k}_{\rho pq} \cdot \left(\hat{z} \times \overline{k}_{\rho rs}\right) \mathrm{d}s \tag{3.58}$$

which reduces to

$$\int\int \overline{e}^{(TM)} \cdot \overline{e}^{(TE)^*} ds = 0. \tag{3.59}$$

This zero property is easily seen when the $TE^{(z)}$ and $TM^{(z)}$ Floquet modes have the same transverse wavenumber because $\overline{k}_{\rho_{pq}} \cdot \hat{z} \times \overline{k}_{\rho_{rs}} = 0$. When the $TE^{(z)}$ and $TM^{(z)}$ Floquet modes have different transverse wavenumbers the equality is true because the integral of $e^{j(\overline{k}_{\rho rs} - \overline{k}_{\rho pq}) \cdot \overline{\rho}}$ over the analysis cell is identically zero.

These results show that the $TE_{pq}^{(z)}$ and $TM_{rs}^{(z)}$ Floquet modes are orthogonal and therefore independent regardless of the selection of pq and rs. This analysis may be repeated for the magnetic fields and the $TEM^{(z)}$ modes as well but it is not necessary due to duality and the special case nature of the $TEM^{(z)}$ mode fields. Thus, the $TE^{(z)}$ and $TM^{(z)}$ Floquet modes constitute two independent electromagnetic fields and can therefore represent any arbitrary Floquet mode electromagnetic field in the analysis cell.

The orthogonality of the full $pq^{\underline{th}}$ and $rs^{\underline{th}}$ Floquet modes can be further demonstrated by considering the inner product of the electric fields of these two modes. Substituting the $pq^{\underline{th}}$ and $rs^{\underline{th}}$ Floquet mode electric fields given by (3.28b) and (3.30b) into a modified form of (3.46a) gives

$$\begin{aligned} \int\int \overline{e}_{pq} \cdot \overline{e}_{rs}^{*} ds = \int\int & \left[\left(\frac{1}{j\omega\epsilon} \nabla \times \nabla \times \hat{z} \Psi_{h_{pq}} \right) + \left(- \nabla \times \hat{z} \Psi_{e_{pq}} \right) \right] \cdot \\ & \left[\left(\frac{1}{j\omega\epsilon} \nabla \times \nabla \times \hat{z} \Psi_{h_{rs}} \right) + \left(- \nabla \times \hat{z} \Psi_{e_{rs}} \right) \right]^{*} ds. \end{aligned} \tag{3.60}$$

As shown above, these field will have dependencies over the integration surface of exponential terms of the form $e^{-j\overline{k}_{\rho pq} \cdot \overline{\rho}}$ for the $pq^{\underline{th}}$ Floquet mode and $e^{j\overline{k}_{\rho rs} \cdot \overline{\rho}}$ for the $rs^{\underline{th}}$ Floquet mode. Expanding the inner product will then result in four integrals of the form

$$\int\int e^{-j\overline{k}_{\rho pq} \cdot \overline{\rho}} e^{j\overline{k}_{\rho rs} \cdot \overline{\rho}} ds \tag{3.61}$$

or

$$\int\int e^{-j\bar{k}_{\rho 00}\cdot\rho} e^{-j(\hat{x}\frac{2\pi p}{a}+\hat{y}\frac{2\pi q}{b})\cdot\bar{\rho}} e^{j\bar{k}_{\rho 00}\cdot\rho} e^{j(\hat{x}\frac{2\pi r}{a}+\hat{y}\frac{2\pi s}{b})\cdot\bar{\rho}} ds, \tag{3.62}$$

after expanding the wavenumbers into the base and modal components from (3.21), which will simplify to

$$\int\int e^{-j(\hat{x}\frac{2\pi p}{a}+\hat{y}\frac{2\pi q}{b})\cdot\bar{\rho}} e^{j(\hat{x}\frac{2\pi r}{a}+\hat{y}\frac{2\pi s}{b})\cdot\bar{\rho}} ds. \tag{3.63}$$

As before, the integration over the analysis cell forces all four of the integrals on the right-hand side of (3.60) to zero when $p \neq r$ or $q \neq s$. These results suggest that the Floquet modes provide a complete orthogonal basis for the electromagnetic fields in the analysis cell.

3.5 Development of the Coupling Dyadic

The coupling dyadic defines the coupling between the electric current density at the air/dielectric interface and the tangential electric field at the air/dielectric interface. The coupling between these quantities is used to fill the elements of the impedance matrix described in Section 3.2. The coupling dyadic has the form

$$\overline{\overline{C}} = \begin{bmatrix} C_{xx} & C_{xy} \\ C_{yx} & C_{yy} \end{bmatrix} \tag{3.64}$$

where the coefficient C_{xy} is the coupling between the x-directed electric current density and the y-directed electric field. The coupling dyadic found in this section is multiplied by the modal description of the sub-domain element described in Section 3.6 to fill the impedance matrix elements.

The choice of field expansion made in Section 3.4.2 automatically satisfies the boundary conditions imposed at all of the edges of the analysis cell by the analysis cell geometry. The Floquet mode expansion inherently contains the $k_{\rho_{pq}}$ transverse wavenumber which is required to satisfy the phase shift boundary condition at the side walls of the analysis cell. The potential functions chosen for the air region of the analysis cell ensure that the fields are bounded at $z = \infty$. Finally, the potential functions chosen for the dielectric region enforce the boundary condition of zero tangential electric field at the ground plane.

There are two boundary conditions which must still be satisfied to couple the Floquet modes in the two regions of the analysis cell. First, the electric field must be continuous at the air/dielectric interface. This continuity of the electric field is required over the entire plane of the interface including the regions which are covered by the PEC metallization which represents the radiating element. The tangential electric field must additionally be zero over the region which is covered by the metallization. Second, the magnetic field must be discontinuous by the electric current density at the air/dielectric interface. These two boundary conditions will be used to determine the coupling between the modes in the two regions of the analysis cell and between the modes and the electric current density distribution used to specify the radiating element.

3.5.1 Continuity of Electric Field at the Air/Dielectric Interface

The electric field boundary condition at the air/dielectric interface requires that

$$\hat{z} \times \left(\overline{E}^{(+)}(\overline{\rho}) - \overline{E}^{(d)}(\overline{\rho}) \right) \Big|_{z=0} \equiv 0 \tag{3.65}$$

where $\overline{E}^{(+)}(\overline{\rho})$ is the total electric field at the upper surface of the air/dielectric interface

given by (3.43a) and $\overline{E}^{(d)}(\overline{\rho})$ is the total electric field at the lower surface of the air/dielectric interface given by (3.44a). This boundary condition can be satisfied in a mode-wise sense due to the orthogonality between Floquet modes as discussed in Section 3.4.2.

Substituting (3.29b) and (3.36b) into (3.65) to satisfy the electric field boundary condition for the $pq^{\underline{th}}$ $\mathrm{TM}^{(z)}$ mode gives

$$\begin{aligned}\widehat{z}\times\Bigg[&\frac{-A_{pq}^{(+)}}{j\omega\epsilon_o}\Big[k_{z_{pq}}^{(+)}\big(k_{x_p}\widehat{x}+k_{y_q}\widehat{y}\big)+\Big(k_{z_{pq}}^{(+)^2}-k_o^2\Big)\widehat{z}\Big]\mathrm{e}^{-j\overline{k}_{pq}^{(+)}\cdot\overline{r}}-\\&\frac{A_{pq}^{(d)}}{j\omega\epsilon_o\epsilon_r}\Big[jk_{z_{pq}}^{(d)}\big(k_{x_p}\widehat{x}+k_{y_q}\widehat{y}\big)\sin\big[k_{z_{pq}}^{(d)}(z+d)\big]+\\&\Big(\epsilon_r k_o^2-k_{z_{pq}}^{(d)^2}\Big)\cos\big[k_{z_{pq}}^{(d)}(z+d)\big]\widehat{z}\Big]\mathrm{e}^{-jk_{pq}^{(d)}\cdot\overline{\rho}}\Bigg]\Bigg|_{z=0}=0,\end{aligned}\tag{3.66}$$

which simplifies to

$$\begin{aligned}\Bigg[&\frac{A_{pq}^{(+)}}{j\omega\epsilon_o}\big[k_{z_{pq}}^{(+)}\big(k_{y_q}\widehat{x}-k_{x_p}\widehat{y}\big)\big]\mathrm{e}^{-j\overline{k}_{pq}^{(+)}\cdot\overline{\rho}}+\\&\frac{A_{pq}^{(d)}}{j\omega\epsilon_o\epsilon_r}\Big[jk_{z_{pq}}^{(d)}\big(k_{y_q}\widehat{x}-k_{x_p}\widehat{y}\big)\sin\big(k_{z_{pq}}^{(d)}d\big)\Big]\mathrm{e}^{-jk_{pq}^{(d)}\cdot\overline{\rho}}\Bigg]=0\end{aligned}\tag{3.67}$$

or

$$k_{z_{pq}}^{(+)}A_{pq}^{(+)}\big(k_{y_q}\widehat{x}-k_{x_p}\widehat{y}\big)=\frac{-jk_{z_{pq}}^{(d)}}{\epsilon_r}A_{pq}^{(d)}\big(k_{y_q}\widehat{x}-k_{x_p}\widehat{y}\big)\sin\big(k_{z_{pq}}^{(d)}d\big).\tag{3.68}$$

The exponential terms cancel because

$$\overline{k}_{pq}^{(+)}\cdot\overline{\rho}=\overline{k}_{pq}^{(d)}\cdot\overline{\rho}.\tag{3.69}$$

For either component of (3.68) the electric field boundary condition results in

$$k_{z_{pq}}^{(+)} A_{pq}^{(+)} = \frac{-jk_{z_{pq}}^{(d)}}{\epsilon_r} A_{pq}^{(d)} \sin\left(k_{z_{pq}}^{(d)} d\right) \tag{3.70}$$

or

$$A_{pq}^{(d)} = \frac{j\epsilon_r k_{z_{pq}}^{(+)}}{k_{z_{pq}}^{(d)} \sin\left(k_{z_{pq}}^{(d)} d\right)} A_{pq}^{(+)}. \tag{3.71}$$

Substituting (3.31a) and (3.39a) with the appropriate Floquet mode weights into (3.65) to satisfy the electric field boundary condition for the $pq^{\underline{th}}$ $\mathrm{TE}^{(z)}$ mode gives

$$\begin{aligned} \hat{z} \times \Bigg[& jB_{pq}^{(+)} \left(k_{y_q} \hat{x} - k_{x_p} \hat{y}\right) \mathrm{e}^{-j\bar{k}_{pq}^{(+)} \cdot \bar{r}} - \\ & jB_{pq}^{(d)} \left(k_{y_q} \hat{x} - k_{x_p} \hat{y}\right) \mathrm{e}^{-j\bar{k}_{pq}^{(d)} \cdot \bar{\rho}} \sin\left[k_{z_{pq}}^{(d)} (z+d)\right] \Bigg] \Bigg|_{z=0} = 0 \end{aligned} \tag{3.72}$$

which reduces to

$$jB_{pq}^{(+)} \left(k_{x_p} \hat{x} + k_{y_q} \hat{y}\right) - jB_{pq}^{(d)} \left(k_{x_p} \hat{x} + k_{y_q} \hat{y}\right) \sin\left(k_{z_{pq}}^{(d)} d\right) = 0, \tag{3.73}$$

requiring that

$$B_{pq}^{(d)} = \frac{B_{pq}^{(+)}}{\sin\left(k_{z_{pq}}^{(d)} d\right)}. \tag{3.74}$$

Finally, substituting (3.33a) and (3.41a) into (3.65) to satisfy the electric field boundary condition for the x-directed electric field $\mathrm{TEM}^{(z)}$ mode gives

$$\begin{aligned} \hat{z} \times \Bigg[& A_{TEM}^{(+)} \frac{-k_o}{\omega\epsilon_o} \hat{x} \mathrm{e}^{-jk_o z} - \\ & A_{TEM}^{(d)} \frac{-k_o}{j\omega\epsilon_o \sqrt{\epsilon_r}} \hat{x} \sin[\epsilon_r k_o (z+d)] \Bigg] \Bigg|_{z=0} = 0 \end{aligned} \tag{3.75}$$

which reduces to

$$A_{TEM}^{(d)} = \frac{j\sqrt{\epsilon_r}\,A_{TEM}^{(+)}}{\sin\left(\sqrt{\epsilon_r}\,k_o d\right)}. \tag{3.76}$$

This results is also applicable to the y-directed electric field TEM$^{(z)}$ mode because these two modes have exactly the same form. Applying (3.65) to the y-directed electric field TEM$^{(z)}$ mode results in

$$B_{TEM}^{(d)} = \frac{j\sqrt{\epsilon_r}\,B_{TEM}^{(+)}}{\sin\left(\sqrt{\epsilon_r}\,k_o d\right)}. \tag{3.77}$$

3.5.2 Continuity of Magnetic Field at the Air/Dielectric Interface

The magnetic field boundary condition at the air/dielectric interface requires that the total magnetic fields in the two regions of the analysis cell be discontinuous by the electric current density at the air/dielectric interface. This boundary condition is expressed as

$$\hat{z} \times \left(\overline{H}^{(+)}(\overline{\rho}) - \overline{H}^{(d)}(\overline{\rho})\right)\Big|_{z=0} = \overline{J}(\overline{\rho}) \tag{3.78}$$

where $\overline{J}(\overline{\rho})$ is the current density distribution at the air/dielectric interface. This magnetic field boundary condition defines the coupling between the weighted set of electric current density basis functions which model the radiating element and the electromagnetic fields in the analysis cell.

A modal description of the electric current density distribution is needed in order to solve (3.78) in a mode-wise sense. This modal description of the electric current density is obtained by computing the $pq^{\underline{th}}$ Floquet mode coefficient for the electric current density distribution. This mode coefficient is found from

$$\overline{J}_{pq} = \frac{1}{ab} \int_{x=-\frac{a}{2}}^{\frac{a}{2}} \int_{y=-\frac{b}{2}}^{\frac{b}{2}} \overline{J}(\overline{\rho}) e^{j\overline{k}_{\rho pq} \cdot \overline{\rho}} dx dy \tag{3.79}$$

which differs from a two-dimensional Fourier series coefficient only by the $\overline{k}_{\rho_0}$ constant phase term in $\overline{k}_{\rho_{pq}}$. The Floquet mode coefficient for the electric current density distribution is developed in Section 3.5.3.

The spatially defined electric current density distribution in (3.78) can now be replace by the double summation over the modal expression for the electric current density. After this substitution, (3.78) becomes

$$\hat{z} \times \left(\overline{H}^{(+)}(\overline{\rho}) - \overline{H}^{(d)}(\overline{\rho}) \right) \Big|_{z=0} = \sum_{p=-\infty}^{\infty} \sum_{q=-\infty}^{\infty} \overline{J}_{pq} e^{-j\overline{k}_{\rho pq} \cdot \overline{\rho}} \tag{3.80}$$

which can be solved in a mode-wise sense. Restricting (3.80) to the single $pq^{\underline{th}}$ mode and substituting the expressions for the magnetic fields, (3.29a), (3.31b), (3.36a), and (3.39b) into (3.80) gives

$$\begin{aligned} \hat{z} \times \Bigg[& - jA_{pq}^{(+)} \left(k_{y_q} \hat{x} - k_{x_p} \hat{y} \right) e^{j\overline{k}_{\rho pq} \cdot \overline{r}} + \\ & \frac{-B_{pq}^{(+)}}{j\omega\mu_o} \left[k_{z_{pq}}^{(+)} \left(k_{x_p} \hat{x} + k_{y_q} \hat{y} \right) + \left(k_{z_{pq}}^{(+)2} - k_o^2 \right) \hat{z} \right] e^{j\overline{k}_{\rho pq} \cdot \overline{r}} - \\ & - jA_{pq}^{(d)} \left(k_{y_q} \hat{x} - k_{x_p} \hat{y} \right) e^{-j\overline{k}_{pq}^{(d)} \cdot \overline{\rho}} \cos\left[k_{z_{pq}}^{(d)} (z+d) \right] - \\ & \frac{B_{pq}^{(d)}}{j\omega\mu_o} \Bigg[- jk_{z_{pq}}^{(d)} \left(k_{x_p} \hat{x} + k_{y_q} \hat{y} \right) \cos\left[k_{z_{pq}}^{(d)} (z+d) \right] + \\ & \left(\epsilon_r k_o^2 - k_{z_{pq}}^{(d)2} \right) \sin\left[k_{z_{pq}}^{(d)} (z+d) \right] \hat{z} \Bigg] e^{-j\overline{k}_{pq}^{(d)} \cdot \overline{\rho}} \Bigg] \Bigg|_{z=0} = \overline{J}_{pq}. \end{aligned} \tag{3.81}$$

Equation (3.81) simplifies to

$$\hat{z}\times\Bigg[-jA_{pq}^{(+)}\left(k_{y_q}\hat{x}-k_{x_p}\hat{y}\right)+$$
$$\frac{-B_{pq}^{(+)}}{j\omega\mu_o}\left[k_{z_{pq}}^{(+)}\left(k_{x_p}\hat{x}+k_{y_q}\hat{y}\right)+\left(k_{z_{pq}}^{(+)^2}-k_o^2\right)\hat{z}\right]-$$
$$-jA_{pq}^{(d)}\left(k_{y_q}\hat{x}-k_{x_p}\hat{y}\right)\cos\left(k_{z_{pq}}^{(d)}d\right)- \tag{3.82}$$
$$\frac{B_{pq}^{(d)}}{j\omega\mu_o}\Bigg[-jk_{z_{pq}}^{(d)}\left(k_{x_p}\hat{x}+k_{y_q}\hat{y}\right)\cos\left(k_{z_{pq}}^{(d)}d\right)+$$
$$\left(\epsilon_r k_o^2-k_{z_{pq}}^{(d)^2}\right)\sin\left(k_{z_{pq}}^{(d)}d\right)\hat{z}\Bigg]\Bigg]=\overline{J}_{pq}.$$

Separating (3.82) into x- and y-components gives

$$-jk_{x_p}A_{pq}^{(+)}+\frac{k_{z_{pq}}^{(+)}k_{y_q}B_{pq}^{(+)}}{j\omega\mu_o}+$$
$$jk_{x_p}A_{pq}^{(d)}\cos\left(k_{z_{pq}}^{(d)}d\right)-\frac{k_{z_{pq}}^{(d)}k_{y_q}B_{pq}^{(d)}}{\omega\mu_o}\cos\left(k_{z_{pq}}^{(d)}d\right)=J_{pq_x} \tag{3.83a}$$

for the x-components and

$$-jk_{y_q}A_{pq}^{(+)}-\frac{k_{z_{pq}}^{(+)}k_{x_p}B_{pq}^{(+)}}{j\omega\mu_o}+$$
$$jk_{y_q}A_{pq}^{(d)}\cos\left(k_{z_{pq}}^{(d)}d\right)+\frac{k_{z_{pq}}^{(d)}k_{x_p}B_{pq}^{(d)}}{\omega\mu_o}\cos\left(k_{z_{pq}}^{(d)}d\right)=J_{pq_y} \tag{3.83b}$$

for the y-components. Collecting the terms of (3.83) to determine the coupling between the pq^{th} mode current density and the $\mathrm{TM}_{pq}^{(z)}$ and $\mathrm{TE}_{pq}^{(z)}$ magnetic fields gives

$$A_{pq}^{(+)}-A_{pq}^{(d)}\cos\left(k_{z_{pq}}^{(d)}d\right)=\frac{j\left(k_{x_p}J_{pq_x}+k_{y_q}J_{pq_y}\right)}{k_{x_p}^2+k_{y_q}^2}=\frac{j\overline{k}_{\rho_{pq}}\cdot\overline{J}_{pq}}{k_{x_p}^2+k_{y_q}^2} \tag{3.84a}$$

for the $\mathrm{TM}_{pq}^{(z)}$ modes and

$$-jk_{z_{pq}}^{(+)}B_{pq}^{(+)}-k_{z_{pq}}^{(d)}B_{pq}^{(d)}\cos\left(k_{z_{pq}}^{(d)}d\right)=\frac{\omega\mu_o\left(k_{y_q}J_{pq_x}-k_{x_p}J_{pq_y}\right)}{k_{x_p}^2+k_{y_q}^2}$$
$$=\frac{-\omega\mu_o\hat{z}\times\overline{k}_{\rho_{pq}}\cdot\overline{J}_{pq}}{k_{x_p}^2+k_{y_q}^2} \tag{3.84b}$$

for the $\mathrm{TE}_{pq}^{(z)}$ modes.

These results for the coupling between the Floquet mode current density and the magnetic fields of the $pq^{\underline{th}}$ mode can be simplified by substituting the coupling results of the electric field boundary condition at the air/dielectric interface into (3.84). This substitution will define the magnetic fields of the $pq^{\underline{th}}$ mode in terms of the $pq^{\underline{th}}$ mode electric current density using only the the magnetic field in the air region of the analysis cell. Substituting (3.71) into (3.84a) gives

$$A_{pq}^{(+)}-\frac{j\epsilon_r k_{z_{pq}}^{(+)}}{k_{z_{pq}}^{(d)}\sin\left(k_{z_{pq}}^{(d)}d\right)}A_{pq}^{(+)}\cos\left(k_{z_{pq}}^{(d)}d\right)=\frac{j\overline{k}_{\rho_{pq}}\cdot\overline{J}_{pq}}{k_{x_p}^2+k_{y_q}^2} \tag{3.85}$$

which simplifies to

$$A_{pq}^{(+)}\left[1-\frac{j\epsilon_r k_{z_{pq}}^{(+)}}{k_{z_{pq}}^{(d)}\sin\left(k_{z_{pq}}^{(d)}d\right)}\cos\left(k_{z_{pq}}^{(d)}d\right)\right]=\frac{j\overline{k}_{\rho_{pq}}\cdot\overline{J}_{pq}}{k_{x_p}^2+k_{y_q}^2} \tag{3.86}$$

or

$$A_{pq}^{(+)}=\frac{jk_{z_{pq}}^{(d)}\sin\left(k_{z_{pq}}^{(d)}d\right)}{k_{z_{pq}}^{(d)}\sin\left(k_{z_{pq}}^{(d)}d\right)-j\epsilon_r k_{z_{pq}}^{(+)}\cos\left(k_{z_{pq}}^{(d)}d\right)}\frac{\overline{k}_{\rho_{pq}}\cdot\overline{J}_{pq}}{k_{x_p}^2+k_{y_q}^2} \tag{3.87}$$

for the $\mathrm{TM}_{pq}^{(z)}$ modes. Substituting (3.74) into (3.84a) gives

$$-jk_{z_{pq}}^{(+)}B_{pq}^{(+)}-k_{z_{pq}}^{(d)}\frac{B_{pq}^{(+)}}{\sin\left(k_{z_{pq}}^{(d)}d\right)}\cos\left(k_{z_{pq}}^{(d)}d\right)=\frac{-\omega\mu_o\hat{z}\times\overline{k}_{\rho_{pq}}\cdot\overline{J}_{pq}}{k_{x_p}^2+k_{y_q}^2} \tag{3.88}$$

which simplifies to

$$B_{pq}^{(+)} = \frac{\omega\mu_o \sin\left(k_{z_{pq}}^{(d)} d\right)}{jk_{z_{pq}}^{(+)} \sin\left(k_{z_{pq}}^{(d)} d\right) + k_{z_{pq}}^{(d)} \cos\left(k_{z_{pq}}^{(d)} d\right)} \frac{\hat{z} \times \overline{k}_{\rho_{pq}} \cdot \overline{J}_{pq}}{k_{x_p}^2 + k_{y_q}^2} \tag{3.89}$$

for the $TE_{pq}^{(z)}$ modes.

The coupling between the $TEM^{(z)}$ Floquet mode electric current density and the $TEM^{(z)}$ Floquet mode magnetic fields must still be determined. Restricting (3.80) to the $TEM^{(z)}$ Floquet mode and substituting the expressions for the $TEM^{(z)}$ Floquet mode magnetic fields, (3.33a), (3.34a), (3.41a), and (3.42a) into (3.80) gives

$$\begin{aligned} \hat{z} \times \Big[& -\hat{y} A_{TEM}^{(+)} + \hat{x} B_{TEM}^{(+)} + \\ & \hat{y} A_{TEM}^{(d)} \cos\left(\sqrt{\epsilon_r}\, k_o d\right) - \hat{x} B_{TEM}^{(d)} \cos\left(\sqrt{\epsilon_r}\, k_o d\right) \Big] = \overline{J}_{TEM} \end{aligned} \tag{3.90}$$

or

$$\hat{x} A_{TEM}^{(+)} + \hat{y} B_{TEM}^{(+)} - \hat{x} A_{TEM}^{(d)} \cos\left(\sqrt{\epsilon_r}\, k_o d\right) - \hat{y} B_{TEM}^{(d)} \cos\left(\sqrt{\epsilon_r}\, k_o d\right) = \overline{J}_{TEM}, \tag{3.91}$$

which has a much simpler structure than (3.82) since each mode coefficient is associated with only one component of the $TEM^{(z)}$ Floquet mode magnetic field. The coupling between the $TEM^{(z)}$ Floquet mode magnetic field coefficients and the $TEM^{(z)}$ Floquet mode electric current density vector components is given by

$$\begin{aligned} A_{TEM}^{(+)} - A_{TEM}^{(d)} \cos\left(\sqrt{\epsilon_r}\, k_o d\right) &= J_{TEMx} \\ B_{TEM}^{(+)} - B_{TEM}^{(d)} \cos\left(\sqrt{\epsilon_r}\, k_o d\right) &= J_{TEM_y}. \end{aligned} \tag{3.92}$$

Including the results of the electric field boundary condition by substituting (3.76) and (3.77) into (3.92) gives

$$A_{TEM}^{(+)} - \frac{j\sqrt{\epsilon_r}A_{TEM}^{(+)}}{\sin\left(\sqrt{\epsilon_r}k_o d\right)}\cos\left(\sqrt{\epsilon_r}k_o d\right) = J_{TEMx}$$
$$B_{TEM}^{(+)} - \frac{j\sqrt{\epsilon_r}B_{TEM}^{(+)}}{\sin\left(\sqrt{\epsilon_r}k_o d\right)}\cos\left(\sqrt{\epsilon_r}k_o d\right) = J_{TEM_y}. \tag{3.93}$$

which simplify to

$$A_{TEM}^{(+)} = \frac{\sin\left(\sqrt{\epsilon_r}k_o d\right)}{\sin\left(\sqrt{\epsilon_r}k_o d\right) - j\sqrt{\epsilon_r}\cos\left(\sqrt{\epsilon_r}k_o d\right)}J_{TEMx}$$
$$B_{TEM}^{(+)} = \frac{\sin\left(\sqrt{\epsilon_r}k_o d\right)}{\sin\left(\sqrt{\epsilon_r}k_o d\right) - j\sqrt{\epsilon_r}\cos\left(\sqrt{\epsilon_r}k_o d\right)}J_{TEM_y}. \tag{3.94}$$

It is interesting to observe that (3.94) are simple special cases of (3.87) as might be expected.

The coupling defined by (3.87) and (3.89) between the $pq^{\underline{th}}$ Floquet mode electric current density and the $\mathrm{TM}_{pq}^{(z)}$ and $\mathrm{TE}_{pq}^{(z)}$ Floquet mode magnetic fields contains two possible singularities. These singularities occur in the $\mathrm{TM}_{pq}^{(z)}$ Floquet mode when

$$k_{z_{pq}}^{(d)}\sin\left(k_{z_{pq}}^{(d)}d\right) - j\epsilon_r k_{z_{pq}}^{(+)}\cos\left(k_{z_{pq}}^{(d)}d\right) = 0 \tag{3.95}$$

and in the $\mathrm{TE}_{pq}^{(z)}$ Floquet mode when

$$jk_{z_{pq}}^{(+)}\sin\left(k_{z_{pq}}^{(d)}d\right) + k_{z_{pq}}^{(d)}\cos\left(k_{z_{pq}}^{(d)}d\right) = 0. \tag{3.96}$$

These singularities indicate the presence of a surface wave mode which is propagating in the dielectric region transverse to the z-axis and evanescent in the air region. The possible presence of surface waves in the electromagnetic model for the coupling between the electric current density and magnetic fields is an undesirable but expected modeling result because surface waves are known to propagate in dielectric slabs. This aspect of the performance of planar antenna array radiating elements printed on dielectric support structures will be discussed in Section 4.2. The inclusion of a realistic loss tangent in the

relative permittivity of the dielectric support is sufficient to assure that the numerical model is well defined where the surface wave occurs by avoiding these singular points.

3.5.3 Completion of the Coupling Dyadic

The computation of the coupling between the electric current density and the tangential electric field at the air/dielectric interface can be completed by substituting the results from enforcing the electric and magnetic field continuity conditions at the air/dielectric interface given by (3.65) and (3.78) into the electric field boundary description of (3.17). This substitution will complete the coupling dyadic and, with the modal description of the sub-domain elements, allows the calculation of the impedance matrix discussed in Section 3.2. Only the amplitude of the tangential electric field need be included in the coupling dyadic because the modal evaluation of the electric potential testing function will account for the integration of the tangetial electric field over the electric potential testing function. There are two distinct cases for the coupling dyadic which must be calculated: the general case for $\overline{k}_{\rho_{pq}} \neq 0$ and the TEM$^{(z)}$ special case of $\overline{k}_{\rho_{pq}} = 0$.

For the non-TEM$^{(z)}$ general case, the coupling dyadic is found by substituting (3.87) and (3.89) into the electric field form in the air region of the analysis cell described by (3.43a) and selecting the tangential components of the $pq^{\underline{th}}$ mode of the result. Using the expressions for the modal electric fields for the $pq^{\underline{th}}$ Floquet mode in the air region of the analysis cell, (3.29b) and (3.31a), the amplitude of the electric field in the air region of the analysis cell is given by

$$\overline{E}_{pq}^{(+)} = A_{pq}^{(+)} \frac{-1}{j\omega\epsilon_o}\left[k_{z_{pq}}^{(+)}\left(k_{x_p}\,\hat{x} + k_{y_q}\,\hat{y}\right) + \left(k_{z_{pq}}^{(+)^2} - k_o^2\right)\hat{z}\right] + B_{pq}^{(+)} j\left(k_{y_q}\,\hat{x} - k_{x_p}\,\hat{y}\right) \tag{3.97}$$

for the $pq^{\underline{th}}$ Floquet mode. Thus, the amplitude of the tangential electric field at the air/dielectric interface as defined by (3.97) is

$$\overline{E}_{pq_t}^{(+)}\Big|_{z=0} = A_{pq}^{(+)} \frac{-1}{j\omega\epsilon_o} k_{z_{pq}}^{(+)}\left(k_{x_p}\,\hat{x} + k_{y_q}\,\hat{y}\right) + B_{pq}^{(+)} j\left(k_{y_q}\,\hat{x} - k_{x_p}\,\hat{y}\right) \tag{3.98}$$

where $A_{pq}^{(+)}$ is defined in (3.87) and $B_{pq}^{(+)}$ is defined in (3.89). The coupling dyadic can now be found by separating (3.98) into the x- and y-directed components of the electric field. This separation gives

$$\overline{E}_{pq_x}^{(+)}\Big|_{z=0} = \left(A_{pq}^{(+)} \frac{-1}{j\omega\epsilon_o} k_{z_{pq}}^{(+)} k_{x_p} + B_{pq}^{(+)} j k_{y_q}\right) \tag{3.99a}$$

for the x-directed electric field amplitude and

$$\overline{E}_{pq_y}^{(+)}\Big|_{z=0} = \left(A_{pq}^{(+)} \frac{-1}{j\omega\epsilon_o} k_{z_{pq}}^{(+)} k_{y_q} - B_{pq}^{(+)} j k_{x_p}\right) \tag{3.99b}$$

for the y-directed electric field amplitude. The C_{xx} and C_{xy} terms of the coupling dyadic given by (3.64) will be found from (3.99a) and the C_{yx} and C_{yy} terms from (3.99b).

Substituting (3.87) and (3.89) into (3.99) for the x-directed electric field amplitude at the air/dielectric interface gives

$$E_{pq_x}^{(+)}\Big|_{z=0} = \frac{-k_{x_p} k_{z_{pq}}^{(+)} k_{z_{pq}}^{(d)} \sin\left(k_{z_{pq}}^{(d)} d\right)}{\omega\epsilon_o\left(k_{x_p}^2 + k_{y_q}^2\right)\left[k_{z_{pq}}^{(d)} \sin\left(k_{z_{pq}}^{(d)} d\right) - j\epsilon_r k_{z_{pq}}^{(+)} \cos\left(k_{z_{pq}}^{(d)} d\right)\right]} \overline{k}_{\rho_{pq}} \cdot \overline{J}_{pq} + \frac{j k_{y_q} \omega\mu_o \sin\left(k_{z_{pq}}^{(d)} d\right)}{\left(k_{x_p}^2 + k_{y_q}^2\right)\left[j k_{z_{pq}}^{(+)} \sin\left(k_{z_{pq}}^{(d)} d\right) + k_{z_{pq}}^{(d)} \cos\left(k_{z_{pq}}^{(d)} d\right)\right]} \hat{z} \times \overline{k}_{\rho_{pq}} \cdot \overline{J}_{pq} \tag{3.100a}$$

and for the y-directed electric field amplitude at the air/dielectric interface gives

$$E_{pq_y}^{(+)}\Big|_{z=0} = \frac{-k_{y_q}k_{z_{pq}}^{(+)}k_{z_{pq}}^{(d)}\sin\left(k_{z_{pq}}^{(d)}d\right)}{\omega\epsilon_o\left(k_{x_p}^2+k_{y_q}^2\right)\left[k_{z_{pq}}^{(d)}\sin\left(k_{z_{pq}}^{(d)}d\right)-j\epsilon_r k_{z_{pq}}^{(+)}\cos\left(k_{z_{pq}}^{(d)}d\right)\right]}\overline{k}_{\rho_{pq}}\cdot\overline{J}_{pq} - \frac{jk_{x_p}\omega\mu_o\sin\left(k_{z_{pq}}^{(d)}d\right)}{\left(k_{x_p}^2+k_{y_q}^2\right)\left[jk_{z_{pq}}^{(+)}\sin\left(k_{z_{pq}}^{(d)}d\right)+k_{z_{pq}}^{(d)}\cos\left(k_{z_{pq}}^{(d)}d\right)\right]}\widehat{z}\times\overline{k}_{\rho_{pq}}\cdot\overline{J}_{pq}. \tag{3.100b}$$

It is useful to define $\mathrm{TM}^{(z)}$ and $\mathrm{TE}^{(z)}$ coefficients as

$$C_{TM} = \frac{k_{z_{pq}}^{(+)}k_{z_{pq}}^{(d)}\sin\left(k_{z_{pq}}^{(d)}d\right)}{\omega\epsilon_o\left(k_{x_p}^2+k_{y_q}^2\right)\left[k_{z_{pq}}^{(d)}\sin\left(k_{z_{pq}}^{(d)}d\right)-j\epsilon_r k_{z_{pq}}^{(+)}\cos\left(k_{z_{pq}}^{(d)}d\right)\right]} \tag{3.101a}$$

and

$$C_{TE} = \frac{j\omega\mu_o\sin\left(k_{z_{pq}}^{(d)}d\right)}{\left(k_{x_p}^2+k_{y_q}^2\right)\left[jk_{z_{pq}}^{(+)}\sin\left(k_{z_{pq}}^{(d)}d\right)+k_{z_{pq}}^{(d)}\cos\left(k_{z_{pq}}^{(d)}d\right)\right]} \tag{3.101b}$$

to simplify the electric field amplitudes for the x-directed electric field amplitude at the air/dielectric interface to

$$E_{pq_x}^{(+)}\Big|_{z=0} = \left(-k_{x_p}C_{TM}\overline{k}_{\rho_{pq}} + k_{y_q}C_{TE}\widehat{z}\times\overline{k}_{\rho_{pq}}\right)\cdot\overline{J}_{pq} \tag{3.102a}$$

and for the y-directed electric field amplitude at the air/dielectric interface to

$$E_{pq_y}^{(+)}\Big|_{z=0} = \left(-k_{y_q}C_{TM}\overline{k}_{\rho_{pq}} - k_{x_p}C_{TE}\widehat{z}\times\overline{k}_{\rho_{pq}}\right)\cdot J_{pq}. \tag{3.102b}$$

Performing the cross-multiplication in (3.102) and expanding the terms in the parentheses gives

$$E_{pq_x}^{(+)}\Big|_{z=0} = \left[-\widehat{x}\left(k_{x_p}^2C_{TM}+k_{y_q}^2C_{TE}\right)+\widehat{y}k_{x_p}k_{y_q}(C_{TE}-C_{TM})\right]\cdot\overline{J}_{pq} \tag{3.103a}$$

for the x-directed electric field amplitude at the air/dielectric interface and

$$E_{pq_y}^{(+)}\Big|_{z=0} = \left[\hat{x}k_{x_p}k_{y_q}(C_{TE} - C_{TM}) - \hat{y}\left(k_{y_q}^2 C_{TM} + k_{x_p}^2 C_{TE}\right)\right] \cdot \overline{J}_{pq} \qquad (3.103b)$$

for the y-directed electric field amplitude at the air/dielectric interface. The terms of the coupling dyadic are clearly visible in (3.103) as the two terms of each of the electric field component amplitudes prior to the dot multiplication with the modal electric current density. The four terms in the coupling dyadic for the non-TEM$^{(z)}$ general case are

$$\begin{aligned} C_{xx} &= \left(k_{x_p}^2 C_{TM} + k_{y_q}^2 C_{TE}\right) \\ C_{xy} &= k_{x_p}k_{y_q}(C_{TE} - C_{TM}) \\ C_{yx} &= C_{xy} \\ C_{yy} &= \left(k_{y_q}^2 C_{TM} + k_{x_p}^2 C_{TE}\right) \end{aligned} \qquad (3.104)$$

where C_{TM} and C_{TE} are given by (3.101).

For the TEM$^{(z)}$ special case, the coupling dyadic is found by substituting (3.94) into the amplitude of the total electric field in the air region of the analysis cell described by (3.43a) and selecting the tangential components of the TEM$^{(z)}$ mode of the result. Using the expressions for the modal electric fields for the TEM$^{(z)}$ Floquet mode in the air region of the analysis cell, (3.33b) and (3.34b), the amplitude of the the TEM$^{(z)}$ Floquet mode electric field in the air region of the analysis cell is given by

$$\overline{E}_{TEM}^{(+)} = A_{TEM}^{(+)} \frac{-k_o}{\omega\epsilon_o}\hat{x}\mathrm{e}^{-jk_o z} + B_{TEM}^{(+)} \frac{-k_o}{\omega\epsilon_o}\hat{y}\mathrm{e}^{-jk_o z}. \qquad (3.105)$$

The amplitude of the tangential electric field at the air/dielectric interface as defined by (3.105) is

$$\overline{E}_{TEM}^{(+)}\Big|_{z=0} = A_{TEM}^{(+)} \frac{-k_o}{\omega\epsilon_o}\hat{x} + B_{TEM}^{(+)} \frac{-k_o}{\omega\epsilon_o}\hat{y} \qquad (3.106)$$

where $A_{TEM}^{(+)}$ and $B_{TEM}^{(+)}$ are defined in (3.94). Substituting (3.94) into (3.106) gives

$$\overline{E}^{(+)}_{TEM}\Big|_{z=0} = \frac{-k_o \sin\left(\sqrt{\epsilon_r}k_o d\right)}{\omega\epsilon_o\left[\sin\left(\sqrt{\epsilon_r}k_o d\right) - j\sqrt{\epsilon_r}\cos\left(\sqrt{\epsilon_r}k_o d\right)\right]} J_{TEM_x}\widehat{x} + \frac{-k_o \sin\left(\sqrt{\epsilon_r}k_o d\right)}{\omega\epsilon_o\left[\sin\left(\sqrt{\epsilon_r}k_o d\right) - j\sqrt{\epsilon_r}\cos\left(\sqrt{\epsilon_r}k_o d\right)\right]} J_{TEM_y}\widehat{y}. \tag{3.107}$$

The elements of the coupling dyadic for the TEM$^{(z)}$ Floquet mode can now be written as

$$\begin{aligned} C_{xx} &= C_{TEM} \\ C_{xy} &= 0 \\ C_{yx} &= C_{xy} \\ C_{yy} &= C_{TEM} \end{aligned} \tag{3.108}$$

where

$$C_{TEM} = \frac{-k_o \sin\left(\sqrt{\epsilon_r}k_o d\right)}{\omega\epsilon_o\left[\sin\left(\sqrt{\epsilon_r}k_o d\right) - j\sqrt{\epsilon_r}\cos\left(\sqrt{\epsilon_r}k_o d\right)\right]}. \tag{3.109}$$

3.6 Modal Sub-domain Element Description

The dyadic which defines the coupling between the modal descriptions of the electric current basis functions and the electric potential testing functions was defined in Section 3.5. The modal descriptions of the bi-triangular patch sub-elements must still be obtained for the electric current density basis function and the electric potential testing function. The modal description of the electric current density basis function is found in a manner which is similar to the determination of the mode coefficients of a Fourier series. In a similar manner, the modal description of the electric potential testing function is simply the integral over the tangential electric field at the air/dielectric interface along the integration path discussed in Section 3.3.2. The impedance matrix can be filled once these modal descriptions have been found.

3.6.1 The Modal Electric Current Density Basis Function Description

The need for a Floquet modal description of the electric current density distribution was discussed in Section 3.5.2. This modal description of the electric current density was defined as

$$\overline{J}(\overline{\rho}) = \sum_{p=-\infty}^{\infty} \sum_{q=-\infty}^{\infty} \overline{J}_{pq} e^{-j\overline{k}_{\rho pq}\cdot\overline{\rho}} \tag{3.110}$$

where the modal electric current density coefficient is given by

$$\overline{J}_{pq} = \frac{1}{ab} \int_{x=-\frac{a}{2}}^{\frac{a}{2}} \int_{y=-\frac{b}{2}}^{\frac{b}{2}} \overline{J}(\overline{\rho}) e^{j\overline{k}_{\rho pq}\cdot\overline{\rho}} dx dy. \tag{3.111}$$

This definition allowed the mode-wise solution of the magnetic field boundary condition at the air/dielectric interface to find the coupling between the electric current density and the magnetic fields in the analysis cell. A modal description of the current of each bi-triangular patch sub-domain element is necessary to allow the elements of the impedance matrix for the MoM analysis to be defined.

The total spatial electric current density distribution has been modeled by a weighted set of sub-domain electric current density basis functions to allow the use of a MoM solution technique. The spatial electric current density distribution in terms of the weighted set of basis functions is given by

$$\overline{J}(\overline{\rho}) = \sum_{n=1}^{N} J_n \overline{j}_n(\overline{\rho}) \tag{3.112}$$

where $J_n \overline{j}_n(\rho)$ is defined by (3.6). Substituting (3.112) into (3.111) gives the total modal electric current density coefficient for the $pq^{\underline{th}}$ Floquet mode as

$$\overline{J}_{pq} = \frac{1}{ab} \int_{x=-\frac{a}{2}}^{\frac{a}{2}} \int_{y=-\frac{b}{2}}^{\frac{b}{2}} \sum_{n=1}^{N} \overline{J}_n(\overline{\rho}) e^{j\overline{k}_{\rho pq} \cdot \overline{\rho}} dx dy. \tag{3.113}$$

Moving the summation inside the integral gives

$$\overline{J}_{pq} = \sum_{n=1}^{N} \frac{1}{ab} \int_{x=-\frac{a}{2}}^{\frac{a}{2}} \int_{y=-\frac{b}{2}}^{\frac{b}{2}} \overline{J}_n(\overline{\rho}) e^{j\overline{k}_{\rho pq} \cdot \overline{\rho}} dx dy. \tag{3.114}$$

This relationship allows the sub-domain element modal electric current density coefficient to be defined as

$$\overline{J}_{pq_n} = \frac{1}{ab} \int_{x=-\frac{a}{2}}^{\frac{a}{2}} \int_{y=-\frac{b}{2}}^{\frac{b}{2}} \overline{J}_n(\overline{\rho}) e^{j\overline{k}_{\rho pq} \cdot \overline{\rho}} dx dy \tag{3.115}$$

for the $n^{\underline{th}}$ electric current density basis function. Substituting (3.5) into (3.115) and limiting the integration to the regions occupied by each half of the electric current density basis function results in

$$\begin{aligned} \overline{J}_{pq_n} = & \frac{|\overline{\rho}_{n2} - \overline{\rho}_{n1}| J_n}{ab} \\ & \left[\frac{1}{\hat{z} \cdot (\overline{\rho}_{n1} - \overline{\rho}_{n3}) \times (\overline{\rho}_{n2} - \overline{\rho}_{n1})} \int_{n-} \int (\overline{\rho} - \overline{\rho}_{n3}) e^{j\overline{k}_{\rho pq} \cdot \overline{\rho}} ds_{n-} + \right. \\ & \left. \frac{1}{\hat{z} \cdot (\overline{\rho}_{n1} - \overline{\rho}_{n4}) \times (\overline{\rho}_{n2} - \overline{\rho}_{n1})} \int_{n+} \int (\overline{\rho} - \overline{\rho}_{n4}) e^{j\overline{k}_{\rho pq} \cdot \overline{\rho}} ds_{n+} \right]. \end{aligned} \tag{3.116}$$

The arbitrary orientation of the electric current density basis function greatly increases the difficulty of performing this integration over the bi-triangular patch sub-domain element in a conventional xy form. This increase in the complexity of the integration occurs because of the difficulty in defining the upper and lower limits of

integration for the first integration performed on each term of (3.111). This challenge can be overcome by integrating over the bi-triangular patch sub-domain element in a coordinate system which is referenced to the patch geometry rather than the analysis cell geometry.

The coordinate system selected in this development is based on the orientation of the joining edge of the bi-triangular sub-domain element. Two coordinate directions which lie in the plane of the air/dielectric interface can be defined in terms of the end points of the joining edge. These coordinate directions are

$$\hat{t} = \frac{\overline{\rho}_{n2} - \overline{\rho}_{n1}}{|\overline{\rho}_{n2} - \overline{\rho}_{n1}|} \tag{3.117}$$

which lies along the joining edge, $(\overline{\rho}_{n1}, \overline{\rho}_{n2})$, and

$$\hat{\mathrm{n}} = \hat{t} \times \hat{z} = -\hat{z} \times \frac{\overline{\rho}_{n2} - \overline{\rho}_{n1}}{|\overline{\rho}_{n2} - \overline{\rho}_{n1}|} \tag{3.118}$$

which is normal to the joining edge. The development of the modal electric current density description for the $n^{\underline{th}}$ electric current density basis functions will be shown for only the half of the sub-domain element which contains $\overline{\rho}_{n3}$, $\bar{\mathrm{J}}_{pq_{n-}}$. The results for the other half of the sub-domain element, $\bar{\mathrm{J}}_{pq_{n+}}$, can be found by substituting $\overline{\rho}_{n4}$ for $\overline{\rho}_{n3}$ in all occurrences.

Rewriting the first term of (3.103) in this newly defined coordinate system gives

$$\bar{j}_{pq_{n-}} = \frac{\mathrm{e}^{j\bar{k}_{\rho pq}\cdot\overline{\rho}_{n3}}}{ab} \int_{n=0}^{h} \int_{t=t_1\frac{n}{h}}^{t_2\frac{n}{h}} \frac{n\hat{\mathrm{n}} + t\hat{t}}{h}\, \mathrm{e}^{jk_t t}\mathrm{e}^{jk_n n}\mathrm{d}t\mathrm{d}n \tag{3.119}$$

where

$$\begin{aligned} h &= \hat{\mathrm{n}} \cdot (\overline{\rho}_{n2} - \overline{\rho}_{n3}), \\ t_1 &= \hat{t} \cdot (\overline{\rho}_{n1} - \overline{\rho}_{n3}), \\ t_2 &= \hat{t} \cdot (\overline{\rho}_{n2} - \overline{\rho}_{n3}), \\ k_n &= \hat{\mathrm{n}} \cdot \overline{k}_{\rho_{pq}}, \text{ and} \\ k_t &= \hat{t} \cdot \overline{k}_{\rho_{pq}}. \end{aligned} \tag{3.120}$$

There are two possible case for the integration with respect to t of (3.119): $k_t = 0$ and $k_t \neq 0$. For the case $k_t = 0$, (3.119) integrates to

$$\overline{\dot{j}}_{pq_{n-}} = \frac{\mathrm{e}^{j\overline{k}_{\rho_{pq}} \cdot \overline{\rho}_{n3}}}{jabk_n^3} \left[\frac{(t_2 - t_1)\hat{\mathrm{n}}}{h^2} + \frac{(t_2^2 - t_1^2)\hat{t}}{2h^3} \right] \left[\left(k_n^2 h^2 + 2jk_n h - 2\right)\mathrm{e}^{jk_n h} + 2 \right] \tag{3.121}$$

when $k_n \neq 0$. For the TEM$^{(z)}$ case, $k_t = 0$ and $k_n = 0$, (3.119) integrates to

$$\overline{\dot{j}}_{pq_{n-}} = \frac{(t_2 - t_1)}{3ab} \left(\frac{\overline{\rho}_{n2} + \overline{\rho}_{n1}}{2} - \overline{\rho}_{n3} \right). \tag{3.122}$$

For the general case, where $k_t \neq 0$, $\overline{k}_{\rho_{pq}} \cdot \overline{\rho}'_{n1} \neq 0$, and $\overline{k}_{\rho_{pq}} \cdot \overline{\rho}'_{n2} \neq 0$, (3.119) integrates to

$$\begin{aligned} \overline{\dot{j}}_{pq_{n-}} = \frac{\mathrm{e}^{j\overline{k}_{\rho_{pq}} \cdot \overline{\rho}_{n3}}}{jabk_t} \Bigg[& \overline{\rho}'_{n2} \frac{\left[1 - j\overline{k}_{\rho_{pq}} \cdot \overline{\rho}'_{n2}\right]\mathrm{e}^{j\overline{k}_{\rho_{pq}} \cdot \overline{\rho}'_{n2}} - 1}{\left(\overline{k}_{\rho_{pq}} \cdot \overline{\rho}'_{n2}\right)^2} - \\ & \overline{\rho}'_{n1} \frac{\left[1 - j\overline{k}_{\rho_{pq}} \cdot \overline{\rho}'_{n1}\right]\mathrm{e}^{j\overline{k}_{\rho_{pq}} \cdot \overline{\rho}'_{n1}} - 1}{\left(\overline{k}_{\rho_{pq}} \cdot \overline{\rho}'_{n1}\right)^2} + \\ & \frac{\hat{t}}{k_t} \left(\frac{\mathrm{e}^{j\overline{k}_{\rho_{pq}} \cdot \overline{\rho}'_{n2}} - 1}{\overline{k}_{\rho_{pq}} \cdot \overline{\rho}'_{n2}} - \frac{\mathrm{e}^{j\overline{k}_{\rho_{pq}} \cdot \overline{\rho}'_{n1}} - 1}{\overline{k}_{\rho_{pq}} \cdot \overline{\rho}'_{n1}} \right) \Bigg] \end{aligned} \tag{3.123}$$

where

$$\overline{\rho}' = \overline{\rho} - \overline{\rho}_{n3}. \tag{3.124}$$

The remaining two cases correspond to constant phase terms along either outside edge of this half of the bi-triangular patch sub-domain element. If $k_{\rho_{pq}} \cdot \overline{\rho}'_{n2} = 0$, (3.114) integrates to

$$\overline{j}_{pq_{n-}} = \frac{e^{j\overline{k}_{\rho_{pq}} \cdot \overline{\rho}_{n3}}}{jabk_t} \left[\frac{\overline{\rho}'_{n2}}{2} - \overline{\rho}'_{n1} \frac{\left[1 - j\overline{k}_{\rho_{pq}} \cdot \overline{\rho}'_{n1}\right] e^{j\overline{k}_{\rho_{pq}} \cdot \overline{\rho}'_{n1}} - 1}{\left(\overline{k}_{\rho_{pq}} \cdot \overline{\rho}'_{n1}\right)^2} + \frac{\widehat{t}}{k_t} \left(j - \frac{e^{j\overline{k}_{\rho_{pq}} \cdot \overline{\rho}'_{n1}} - 1}{\overline{k}_{\rho_{pq}} \cdot \overline{\rho}'_{n1}} \right) \right]. \tag{3.125}$$

Similarly, if $k_{\rho_{pq}} \cdot \overline{\rho}'_{n2} = 0$, (3.114) integrates to

$$\overline{j}_{pq_{n-}} = \frac{e^{j\overline{k}_{\rho_{pq}} \cdot \overline{\rho}_{n3}}}{jabk_t} \left[\overline{\rho}'_{n2} \frac{\left[1 - j\overline{k}_{\rho_{pq}} \cdot \overline{\rho}'_{n2}\right] e^{j\overline{k}_{\rho_{pq}} \cdot \overline{\rho}'_{n2}} - 1}{\left(\overline{k}_{\rho_{pq}} \cdot \overline{\rho}'_{n2}\right)^2} - \frac{\overline{\rho}'_{n1}}{2} + \frac{\widehat{t}}{k_t} \left(\frac{e^{j\overline{k}_{\rho_{pq}} \cdot \overline{\rho}'_{n2}} - 1}{\overline{k}_{\rho_{pq}} \cdot \overline{\rho}'_{n2}} - j \right) \right]. \tag{3.126}$$

As discussed above, the results of (3.121), (3.122), (3.123), (3.125), and (3.126) are applicable to the half of the sub-domain element which contains $\overline{\rho}_{n4}$ by replacing $\overline{\rho}_{n3}$ with $\overline{\rho}_{n4}$ throughout the term. The complete description of the modal electric current density basis function is found by adding the contributions of each half of the bi-triangular patch electric current density basis function. The result of this addition gives the modal electric current density basis function description which is used to determine the impedance matrix.

3.6.2 The Modal Electric Potential Testing Function Description

The modal description of the electric potential testing function is found by integrating the tangential modal electric field at the air/dielectric interface along the integration path described in Section 3.3.2. The impedance matrix can be filled once the

modal electric potential testing function description is defined. The other quantities which are necessary to fill the matrix, the coupling dyadic and the modal electric current density basis function description, were found in Section 3.5 and 3.6.1. The integral for the modal electric potential testing function description has two cases: the general case when the phase of the electric field varies along the integration path, $\overline{k}_{\rho_{pq}} \cdot \bar{l} \neq 0$, and a special case when the electric field has constant phase along the integration path, $\overline{k}_{\rho_{pq}} \cdot \bar{l} = 0$. The general case will be developed here first, then the special TEM$^{(z)}$ case.

The modal description of the electric potential testing function for the general case is found from

$$\overline{V}_{pq_m} = -\int_{\bar{c}_{m-}}^{\bar{b}_m} \overline{E}_{pq}^{(+)}(\overline{\rho}) \cdot \mathrm{d}\bar{l}_1 - \int_{\bar{b}_m}^{\bar{c}_{m+}} \overline{E}_{pq}^{(+)}(\overline{\rho}) \cdot \mathrm{d}\bar{l}_2 \tag{3.127}$$

where $\bar{b}_m$, $\bar{c}_{m-}$, and $\bar{c}_{m+}$ are the position vectors to the center of the joining edge, $(\overline{\rho}_{n1}, \overline{\rho}_{n2})$, and the centroids of the halves of the sub-domain element by substituting in the tangential electric field description from (3.43a) for a single Floquet mode. Substituting this description into (3.127) gives

$$\overline{V}_{pq_m} = \overline{v}_{pq_m} \cdot \overline{E}_{pq}^{(+)} \tag{3.128}$$

where $\overline{E}_{pq}^{(+)}$ is the complex vector tangential electric field amplitude for the $pq^{\underline{th}}$ Floquet mode and $\overline{v}_{pq_m}$, the basis testing function for the $m^{\underline{th}}$ sub-domain element, is given by

$$\overline{v}_{pq_m} = -\int_{\bar{c}_{m-}}^{\bar{b}_m} \mathrm{e}^{-j\overline{k}_{\rho pq}\cdot\overline{\rho}} \mathrm{d}\bar{l}_1 + -\int_{\bar{b}_m}^{\bar{c}_{m+}} \mathrm{e}^{-j\overline{k}_{\rho pq}\cdot\overline{\rho}} \mathrm{d}\bar{l}_2. \tag{3.129}$$

The integration path $\bar{l}_1$ is from the centroid of the sub-domain element half which contains $\overline{\rho}_{n3}$, $\bar{c}_{m-}$, to the center of the joining edge of the bi-triangular sub-domain element, $\bar{b}_m$.

The integration path $\bar{l}_2$ is from the center of the joining edge of the bi-triangular sub-domain element, $\bar{b}_m$, to the centroid of the sub-domain element half which contains $\bar{\rho}_{n4}$, $\bar{c}_{m+}$. The position vectors from the coordinate system origin to the centroids and the center of the joining edge are found from

$$\begin{aligned} \bar{c}_{m-} &= \frac{\bar{\rho}_{m1} + \bar{\rho}_{m2} + \bar{\rho}_{m3}}{3}, \\ \bar{c}_{m+} &= \frac{\bar{\rho}_{m1} + \bar{\rho}_{m2} + \bar{\rho}_{m4}}{3}, \text{ and} \\ \bar{b}_m &= \frac{\bar{\rho}_{m1} + \bar{\rho}_{m2}}{2}. \end{aligned} \tag{3.130}$$

For the general case, (3.129) integrates to

$$\begin{aligned} \bar{v}_{pq_m} = \Delta\bar{\rho}_{m1} e^{-j\bar{k}_{\rho pq}\cdot\bar{c}_{m-}} \frac{e^{-j\bar{k}_{\rho pq}\cdot\Delta\bar{\rho}_{m1}} - 1}{j\bar{k}_{\rho_{pq}} \cdot \Delta\bar{\rho}_{m1}} - \\ \Delta\bar{\rho}_{m2} e^{-j\bar{k}_{\rho pq}\cdot\bar{c}_{m+}} \frac{e^{-j\bar{k}_{\rho pq}\cdot\Delta\bar{\rho}_{m2}} - 1}{j\bar{k}_{\rho_{pq}} \cdot \Delta\bar{\rho}_{m2}} \end{aligned} \tag{3.131}$$

where

$$\begin{aligned} \Delta\bar{\rho}_{m1} &= \bar{c}_{m-} - \bar{b}_m \\ \Delta\bar{\rho}_{m2} &= \bar{c}_{m+} + \bar{b}_m. \end{aligned} \tag{3.132}$$

For the special case when the electric field has constant phase along the integration path, that is $\bar{k}_{\rho_{pq}} \cdot \bar{l} = 0$, the integration which contains the special case simplifies to

$$e^{-j\bar{k}_{\rho pq}\cdot\bar{c}_{m-}} \int_{\bar{c}_{m-}}^{\bar{b}_m} d\bar{l}_1 = \Delta\bar{\rho}_{m1} e^{-j\bar{k}_{\rho pq}\cdot\bar{c}_{m-}} \tag{3.133a}$$

for the portion of the integration path $\bar{l}_1$ and

$$e^{-j\bar{k}_{\rho pq}\cdot\bar{c}_{m+}}\int_{\bar{b}_m}^{\bar{c}_{m+}} d\bar{l}_2 = \Delta\bar{\rho}_{m2}e^{-j\bar{k}_{\rho pq}\cdot\bar{c}_{m+}} \tag{3.133b}$$

for the portion of the integration path $\bar{l}_2$.

3.7 Completion of the Method of Moments Analysis

At this point all of the components necessary for the MoM analysis of an arbitrarily shaped, planar array have been introduced. The model of the radiating element was presented in Section 3.3. The representation of the electromagnetic fields in the analysis cell was developed in Section 3.4. This representation was used to determine the coupling dyadic in Section 3.5. Finally, the modal representations of the radiating element model electric current density and electric potential were developed in Section 3.6. There are three steps remaining to complete the MoM analysis: the impedance matrix must be filled, the excitation of the radiating element must be modeled, and the resulting system of linear equations must be solved for the unknown electric current basis function weights.

The impedance matrix for the MoM analysis is filled by summing the contributions to the elements of the matrix for each of the Floquet modes. This summing process results in a representation for a matrix element of

$$Z_{mn} = \sum_{p=-\infty}^{\infty}\sum_{q=-\infty}^{\infty} \bar{v}_{pq_m}\cdot\bar{\bar{C}}_{pq}\cdot\bar{j}_{pq_n} \tag{3.134}$$

where the modal representation of the electric potential testing function for the $pq^{\underline{th}}$ Floquet mode, $\bar{v}_{pq_m}$, is defined in Section 3.6.2, the coupling dyadic for the $pq^{\underline{th}}$ Floquet mode, $\bar{\bar{C}}_{pq}$, is defined in Section 3.5.4, and the modal representation of the electric current density basis function, $\bar{j}_{pq_n}$, is defined in Section 3.6.1. While the summations in (3.134)

are infinite, practical experience using this algorithm indicates that they need be continued only to where the highest order mode changes phase 2π over the smallest dimension of the smallest element of the sub-domain basis set. This condition is given by

$$|\overline{k}_{\rho_{pmaxqmax}}| = 2\pi/\min\Big[|\overline{\rho}_{n1}-\overline{\rho}_{n2}|, |\overline{\rho}_{n1}-\overline{\rho}_{n3}|, |\overline{\rho}_{n1}-\overline{\rho}_{n4}|, |\overline{\rho}_{n2}-\overline{\rho}_{n3}|, |\overline{\rho}_{n2}-\overline{\rho}_{n4}|, |\overline{\rho}_{n3}-\overline{\rho}_{n4}|\Big] \tag{3.135}$$

This result corresponds to the spatial Nyquist criterion over the sub-domain basis set in the analysis cell. For simplicity, the Nyquist wavenumber defined by (3.135) is used as both the x- and y-directed maximum wavenumbers rather than determining the required maximum wavenumber in each direction. The number of Floquet modes defined as meeting the Nyquist criteria in each direction for this choice is defined by

$$\begin{aligned} P_{Nyq} &= \frac{a}{|\overline{k}_{\rho_{pmaxqmax}}|} \\ Q_{Nyq} &= \frac{a}{|\overline{k}_{\rho_{pmaxqmax}}|}. \end{aligned} \tag{3.136}$$

Input impedance results computed with the double summation truncated at P_{Nyq}, Q_{Nyq} has been found to introduce only slight variation from input impedance results computed with the double summation truncated at $9P_{Nyq}, 9Q_{Nyq}$. These results are presented in Section 4.1. The convergence of the solution will be discussed more fully in Section 4.1

The radiating element is excited at K feed locations in the set of sub-domain elements used to describe the radiating element by K Thèvenin equivalent sources which are in series with the two halves of the sub-domain basis functions which contain the sources. The configuration of the source model is shown in Figure 3.5 This model of the source includes an input voltage and a source impedance. The source is modeled as V_s volts peak with a source impedance of $R_s + jX_s$ ohms.

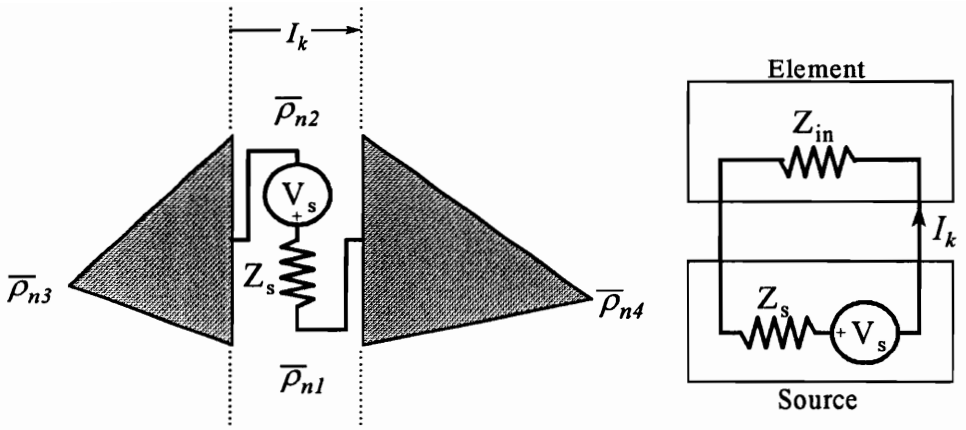

Figure 3.5. Thèvenin equivalent source model used for the excitation of the radiating element showing the source voltage and impedance. The source model is shown in the element and in the network representation of the radiating element.

The radiating element excitation is included in the MoM analysis in both the impedance matrix and the sub-domain element voltage column vector. The source impedance is simply added to the impedance matrix element Z_{mm_k}, where the source is the $k^{\underline{th}}$ source in the $m^{\underline{th}}$ sub-domain element. The source impedance must be scaled by the length of the joining edge of the $m^{\underline{th}}$ electric current density basis function, $|\overline{\rho}_{m2} - \overline{\rho}_{m1}|$, because the impedance matrix was developed from the current densities of the elements rather than the total current flowing across the joining edge of the sub-domain element. This scaling results in a self-impedance term for the $m^{\underline{th}}$ sub-domain element of

$$Z_{mm_k} = \sum_{p=-\infty}^{\infty} \sum_{q=-\infty}^{\infty} \overline{v}_{pq_m} \cdot \overline{\overline{C}}_{pq} \cdot \overline{j}_{pq_m} + |\overline{\rho}_{m2} - \overline{\rho}_{m1}| Z_{s_k} \qquad (3.137)$$

where the first term is due to the electromagnetic coupling.

The column vector of sub-domain element voltages is filled with the source voltage of the sub-domain elements. The source voltage is V_s only for the sub-domain elements which contain sources and zero for the remaining sub-domain elements. This column

vector and the impedance matrix are the known portions of the system of linear equations defined in (3.4). The remaining step in the computation of the unknown weights of the electric current density basis set is the solution of the this system of linear equations. An LU-decomposition/backsolving matrix solution technique [37] was used for the solution of the system of linear equations for the unknown electric current density weights.

3.8 Radiating Element Characterization

There are four measures of antenna performance which can be found once the electric current density distribution on the radiating element has been computed using the MoM analysis technique. These performance measures are the input impedance of the radiating element in the array environment, the power delivered to the radiating element by the source(s), the power radiated by the radiating element, and the electric field in the analysis cell. The approach which is used to find these measures will be discussed in this section. The input impedance and power of the radiating element will be discussed in Section 3.8.1. The generation of the sampled electric field, useful for diagnosis and physical explanation of the radiating element performance, on an xy-grid in the analysis cell will be discussed in Section 3.8.2. Finally, the radiated power of the radiating element and the relationship between the radiated power and the antenna pattern of the radiating element will be discussed in Section 3.8.3.

3.8.1 Radiating Element Input Impedance and Power

The input impedance of the radiating element can be computed as the effective input impedance at each of the source points. The electric current density basis function weights and the known voltage and impedance of the source are used in this computation.

As discussed in Section 3.7, the sources which are exciting the radiating element are modeled as Thèvenin equivalent sources in series with the sub-domain element containing the source. The total current flowing on the $m^{\underline{th}}$ sub-domain element of the electric current density basis set at the location of the $k^{\underline{th}}$ source is found from

$$I_k = |\overline{\rho}_{m2} - \overline{\rho}_{m1}| J_m \tag{3.138}$$

where J_m is the current density weight found from the MoM analysis. The input impedance at the $k^{\underline{th}}$ sub-domain element is found from

$$Z_{in_k} = \frac{V_{s_k}}{I_k} - Z_{s_k} \tag{3.139}$$

where Z_{s_k} is the source impedance at the $m^{\underline{th}}$ sub-domain element of the $k^{\underline{th}}$ source and V_{s_k} is the voltage impressed across the $m^{\underline{th}}$ sub-domain element and the source impedance of the Thèvenin equivalent source given in Section 3.7.

The power input to the radiating element at the $m^{\underline{th}}$ sub-domain element can be found from the total current flowing on the $m^{\underline{th}}$ sub-domain element and the input impedance of the radiating element at the $m^{\underline{th}}$ sub-domain element. This power delivered to the radiating element at the $m^{\underline{th}}$ sub-domain element by the $k^{\underline{th}}$ source is given by

$$P_{in_k} = \frac{1}{2}\mathrm{Re}[I_m I_m^* Z_{in_k}]. \tag{3.140}$$

The total power which is input to the radiating element by all of the sources can be found by summing the contributions from all of the K sources.

3.8.2 The Sampled Electric Field in the Analysis Cell

The electric field in the analysis cell can be found from the summation of the contributions of each of the Floquet mode $\mathrm{TM}^{(z)}$ and $\mathrm{TE}^{(z)}$ electric fields. The electric

field is found in this analysis approach by finding the Floquet mode $TM^{(z)}$ and $TE^{(z)}$ field weights for each of the weighted electric current density basis functions for a single pq mode. The contributions to the mode weights for each of the electric current density basis functions are then summed to determine the total Floquet mode $TM^{(z)}$ and $TE^{(z)}$ field weights for the current mode. These mode weights are used to find the x-, y-, and z-components of the electric field at each of the desired sample points from (3.43a) and (3.44a). The three components of the electric field are then summed over the Floquet modes which were used in the generation of the impedance matrix for the MoM analysis.

3.8.3 Radiated Power and the Active Element Pattern

The Floquet modes which have a real longitudinal wavenumber in the air region of the analysis cell, $k_{z_{pq}}^{(+)} > 0$, are radiating modes which transport power away from the radiating element. The total power radiated by the radiating element is the power in the analysis cell from the total electromagnetic fields generated by these radiating modes. The radiated power can be calculated more easily for each of the radiating $TM^{(z)}$ and $TE^{(z)}$ mode independently and then summed because of the orthogonalities between the $TM^{(z)}$ and $TE^{(z)}$ modes and between modes of different transverse wavenumber, $\overline{k}_{\rho_{pq}}$, discussed in Section 3.4.2.

The total power in the $pq^{\underline{th}}$ Floquet mode is found from

$$P_{r_{pq}} = \frac{1}{2} \int_{x=\frac{-a}{2}}^{\frac{a}{2}} \int_{y=\frac{-b}{2}}^{\frac{b}{2}} \overline{E}_{pq}^{(+)}(\overline{\rho}) \times \left[\overline{H}_{pq}^{(+)}(\overline{\rho})\right]^{*} \cdot \hat{z}\, \mathrm{d}x\mathrm{d}y \tag{3.141}$$

which can be rewritten as

$$P_{r_{pq}} = \frac{1}{2}\left|\sum_{m=1}^{M} A_{pq}^{(+)} J_m\right|^2 \mathrm{Re}\left\{\int_{x=\frac{-a}{2}}^{\frac{a}{2}}\int_{y=\frac{-b}{2}}^{\frac{b}{2}} \overline{e}_{pq}^{(TM+)}(\overline{\rho}) \times \left[\overline{h}_{pq}^{(TM+)}(\overline{\rho})\right]^* \cdot \widehat{z}\,\mathrm{d}x\mathrm{d}y\right\} + \frac{1}{2}\left|\sum_{m=1}^{M} B_{pq}^{(+)} J_m\right|^2 \mathrm{Re}\left\{\int_{x=\frac{-a}{2}}^{\frac{a}{2}}\int_{y=\frac{-b}{2}}^{\frac{b}{2}} \overline{e}_{pq}^{(TE+)}(\overline{\rho}) \times \left[\overline{h}_{pq}^{(TE+)}(\overline{\rho})\right]^* \cdot \widehat{z}\,\mathrm{d}x\mathrm{d}y\right\}. \tag{3.142}$$

Substituting the expressions for the mode electric and magnetic fields from (3.29) and (3.31) into (3.142) gives

$$\begin{aligned} P_{r_{pq}} = \frac{1}{2}\left|\sum_{m=1}^{M} A_{pq}^{(+)} J_m\right|^2 \mathrm{Re}\Bigg\{ & \int_{x=\frac{-a}{2}}^{\frac{a}{2}}\int_{y=\frac{-b}{2}}^{\frac{b}{2}} \frac{-1}{j\omega\epsilon_o}\Big[k_{z_{pq}}^{(+)}\left(k_{x_p}\,\widehat{x} + k_{y_q}\,\widehat{y}\right) + \left(k_{z_{pq}}^{(+)2} - k_o^2\right)\widehat{z}\Big]\mathrm{e}^{-j\overline{k}_{pq}^{(+)}\cdot\overline{r}} \times \\ & \Big[-j\left(k_{y_q}\,\widehat{x} - k_{x_p}\,\widehat{y}\right)\mathrm{e}^{-j\overline{k}_{pq}^{(+)}\cdot\overline{r}}\Big]^* \cdot \widehat{z}\,\mathrm{d}x\mathrm{d}y\Bigg\} + \\ \frac{1}{2}\left|\sum_{m=1}^{M} B_{pq}^{(+)} J_m\right|^2 \mathrm{Re}\Bigg\{ & \int_{x=\frac{-a}{2}}^{\frac{a}{2}}\int_{y=\frac{-b}{2}}^{\frac{b}{2}} j\left(k_{y_q}\,\widehat{x} - k_{x_p}\,\widehat{y}\right)\mathrm{e}^{-j\overline{k}_{pq}^{(+)}\cdot\overline{r}} \times \\ & \left[\frac{-1}{j\omega\mu_o}\Big[k_{z_{pq}}^{(+)}\left(k_{x_p}\,\widehat{x} + k_{y_q}\,\widehat{y}\right) + \left(k_{z_{pq}}^{(+)2} - k_o^2\right)\widehat{z}\Big]\mathrm{e}^{-j\overline{k}_{pq}^{(+)}\cdot\overline{r}}\right]^* \cdot \widehat{z}\,\mathrm{d}x\mathrm{d}y\Bigg\} \end{aligned} \tag{3.143}$$

which reduces to

$$P_{r_{pq}} = \left|\sum_{m=1}^{M} A_{pq}^{(+)} J_m\right|^2 \frac{abk_{x_p}k_{y_q}k_{z_{pq}}^{(+)}}{\omega\epsilon_o} + \left|\sum_{m=1}^{M} B_{pq}^{(+)} J_m\right|^2 \frac{ab\left(k_{x_p}^2 + k_{y_q}^2\right)k_{z_{pq}}^{(+)}}{\omega\mu_o}. \tag{3.144}$$

The power in the $\mathrm{TEM}^{(z)}$ Floquet mode is found from

$$P_{r_{pq}} = \frac{1}{2}\mathrm{Re}\left\{ \int_{x=\frac{-a}{2}}^{\frac{a}{2}} \int_{y=\frac{-b}{2}}^{\frac{b}{2}} \frac{-k_o}{\omega\epsilon_o} \left[\left(\sum_{m=1}^{M} A_{TEM}^{(+)} J_m \right) \hat{x} + \left(\sum_{m=1}^{M} B_{TEM}^{(+)} J_m \right) \hat{y} \right] \mathrm{e}^{-jk_o z} \right. \tag{3.145}$$
$$\left. \times \left\{ \left[\left(\sum_{m=1}^{M} B_{TEM}^{(+)} J_m \right) \hat{x} - \left(\sum_{m=1}^{M} A_{TEM}^{(+)} J_m \right) \hat{y} \right] \mathrm{e}^{-jk_o z} \right\}^* \cdot \hat{z}\, \mathrm{d}x\mathrm{d}y \right\}$$

which reduces to

$$P_{r_{pq}} = \frac{abk_o}{2\omega\epsilon_o} \left(\left| \sum_{m=1}^{M} A_{TEM}^{(+)} J_m \right|^2 + \left| \sum_{m=1}^{M} B_{TEM}^{(+)} J_m \right|^2 \right). \tag{3.146}$$

The total aperture efficiency of the radiating element is given by the ratio of the power radiated from the analysis cell by the desired TE_{00} and TM_{00} modes to the total power input to the radiating element. This definition of aperture efficiency includes both loss and input reflection effects and is equivalent to the ability of the radiating element to direct power into the desired direction of beam scanning. The total power radiated by the radiating element also includes the power, if any, radiated into grating lobes. This power is not included in aperture efficiency by this definition because the power in the grating lobes does not contribute to the desired main beam of the antenna array. This definition of the aperture efficiency of the radiating element is

$$\eta_{ap}(\theta_o, \phi_o) = \frac{P_{r_{00}}(\theta_o, \phi_o)}{P_{inc}(\theta_o, \phi_o)} \tag{3.147}$$

where $P_{r_{00}}(\theta_o, \phi_o)$ is found with $p = q = 0$ from (3.144) or (3.146) for an antenna main beam scanned in the (θ_o, ϕ_o) direction. The power incident on the radiating element, P_{inc}, is the total power incident on the radiating element. This incident power is given by

$$P_{inc}(\theta_o, \phi_o) = \sum_{k=1}^{K} \frac{P_{in_k}(\theta_o, \phi_o)}{\left(1 - |\Gamma_{a_k}(\theta_o, \phi_o)|^2\right)} \tag{3.148}$$

where the input power to the radiating element at the $k^{\underline{th}}$ source, $P_{in_k}(\theta_o, \phi_o)$, is found from (3.140) with the antenna array scanned to (θ_o, ϕ_o) and the active reflection coefficient of the radiating element at $k^{\underline{th}}$ source, $\Gamma_{a_k}(\theta_o, \phi_o)$, is given by

$$\Gamma_{a_k}(\theta_o, \phi_o) = \frac{Z_{in_k}(\theta_o, \phi_o) - Z_{s_k}^*}{Z_{in_k}(\theta_o, \phi_o) + Z_{s_k}} \tag{3.149}$$

where Z_{s_k} is the source impedance of the $k^{\underline{th}}$ source and $Z_{in_k}(\theta_o, \phi_o)$ is the input impedance of the radiating element with the antenna array scanned to the (θ_o, ϕ_o) direction given by (3.139).

The aperture efficiency of the radiating element, (3.147), can be used to find the element pattern of the radiating element in the large phased antenna array environment. This pattern, called the active element pattern, is usually measured by exciting a single, central element in the antenna array and terminating the other elements in the source impedance [5]. The active element pattern is the correct element for pattern multiplication using ideal array theory because it is proportional to the envelope of the main beam peak gain of the antenna array as the main beam is scanned [38]. An intuitive discussion of the development of the active element pattern from both the input reflection coefficient and the aperture efficiency is presented here. While this discussion is not extremely thorough, a more complete development is not warranted by the limited use of the active element pattern in this document.

The active element pattern is also related to the input reflection coefficient of the radiating element in the fully excited antenna array [5] by

$$|\Gamma_a(\theta, \phi)| = \sqrt{1 - \frac{g_r(\theta, \phi)}{g_{ideal}(\theta, \phi)}} \tag{3.150}$$

where $\Gamma_a(\theta, \phi)$ is the input reflection coefficient of the radiating element in the fully

excited antenna array beam scanned in the (θ, ϕ) direction and $g_{ideal}(\theta, \phi)$, the ideal element pattern in a planar array with a rectangular grid with spacings of a by b, is

$$g_{ideal}(\theta, \phi) = \frac{4\pi}{\lambda_o^2} A_{proj.\,cell} = \frac{4\pi}{\lambda_o^2} ab\cos\theta \tag{3.151}$$

The ideal radiating element gain pattern is essentially the gain pattern of a uniformly excited aperture the size of the grid cell in the antenna array. The $ab\cos\theta$ term in (3.149) is the projected physical aperture of the antenna array grid cell, $A_{proj.\,cell}$, in the (θ, ϕ) direction. The active element pattern can be derived from (3.150) as

$$g_r(\theta, \phi) = \left(1 - |\Gamma_a(\theta, \phi)|^2\right) \frac{4\pi}{\lambda_o^2} ab\cos\theta. \tag{3.152}$$

This definition of the active element pattern can be intuitively justified [38] by noting that the maximum gain available from an antenna array scanned in the (θ_o, ϕ_o) direction is

$$G_{array}^{max}(\theta_o, \phi_o) = \frac{4\pi}{\lambda_o^2} A_{proj}(\theta_o, \phi_o) \tag{3.153}$$

where $A_{proj}(\theta_o, \phi_o)$ is the area of the antenna array aperture projected in the (θ_o, ϕ_o) direction given by

$$A_{proj}(\theta_o, \phi_o) = A_{array}\cos\theta \tag{3.154}$$

where A_{array} is the area of the antenna array aperture. The aperture area of the antenna array of N radiating elements is also given by

$$A_{array} = N\, A_{cell} \tag{3.155}$$

where, for a rectangular antenna array grid of dimension a by b, A_{cell} is

$$A_{cell} = ab. \tag{3.156}$$

The maximum gain of a radiating element of this antenna array in the fully excited antenna

array environment must then be

$$g_{el}^{max}(\theta_o, \phi_o) = \frac{G_{array}^{max}(\theta_o, \phi_o)}{N} = \frac{4\pi}{\lambda_o^2} ab\cos\theta. \tag{3.157}$$

The gain realized from each element is equal to the gain of the ideal radiating element multiplied by the efficiency of the actual radiating element in the fully excited antenna array beam scanned in the (θ_o, ϕ_o) direction. This relationship results in the active element pattern definition given by (3.152).

The total dependence of the active element pattern is

$$g_r(\theta, \phi) \propto \eta_{ap}(\theta, \phi) \tag{3.158}$$

where $\eta_{ap}(\theta, \phi)$ is the efficiency of the radiating element when the main beam of the antenna array is steered to the (θ, ϕ) direction given by (3.147). The gain of the active element pattern can be found by multiplying the aperture efficiency of the radiating element by the normalized area of the analysis cell. This results in the active element pattern given by

$$g_r(\theta, \phi) = \frac{4\pi ab}{\lambda_o^2} \eta_{ap}(\theta, \phi). \tag{3.159}$$

The $\cos\theta$ aperture projection term is not included separately in the aperture efficiency definition of the active element pattern, (3.159), because the this definition of the aperture efficiency already accounts for the coupling from the radiating element to a plane wave traveling the (θ_o, ϕ_o) direction. The advantage of this definition of the active element pattern over the definition of (3.152) is that the effects of dissipative loss in the radiating element are included in this result but not in (3.152). While these loss effects are generally small, significant loss may be present in some radiating element designs where the element is significantly loaded in an attempt to extend the range of beam scanning.

4. COMPUTATIONAL RESULTS

The analysis approach discussed in Chapter 3 has been implemented as a compiled Fortran executable software tool for the analysis of infinite antenna arrays. The code is called **A**nalysis **S**oftware for **I**nfinite **A**rrays (ASIA). The source code listing of ASIA consists of approximately 4500 lines in 29 different routines. ASIA was designed to be as general as possible within the constraints of the analysis approach described in Chapter 3. ASIA is currently compiled for use on MS-DOS micro-computers which are compatible with INTEL 80486 and higher architectures. ASIA uses file input and output to allow operation of the code in a batch environment. A full description of use of ASIA is available in the user's guide [39] and will not be included here. Delays in the implementation of the radiation computation sections of ASIA prevent demonstrating these features here.

This chapter begins with an examination of the convergence of the analysis approach described in Chapter 3. The convergence of the analysis with respect to the numbers of Floquet modes and sub-domain basis functions used in the solution is discussed in Section 4.1. This convergence testing allows analysis parameters for which the numerical results are apparently valid to be found. The chapter continues with the discussion of the analysis of two well-known antenna arrays in Section 4.2. The behavior of these arrays has been previously characterized and is used to validate the analysis approach. This chapter concludes with a discussion of preliminary analysis results for a new radiating element which is being investigated using ASIA. The results shown in Figure 4.3 illustrate one of the major advantages of this analysis approach as compared to the previous techniques discussed in Section 2.2.4.

4.1 Convergence of the Solution

The nature of the convergence of the solution of the analysis approach discussed in Chapter 3 must be examined before this technique can be used to characterize radiating elements in antenna arrays. In this sense, convergence is used to discuss how quickly the analysis approach can be expected to predict a correct, or at least nearly constant, result as the numbers of modes and sub-domain basis functions used in the analysis increase. The convergence of the solution with respect to the number of Floquet modes used in the analysis can be discussed directly since the Floquet series representation is convergent. The convergence of the analysis approach with respect to the number of Floquet modes used is discussed in Section 4.1.1. This discussion examines the convergence of the analysis approach for both unscanned and scanned cases. The convergence of the analysis approach must be approximated for the number of sub-domain basis functions used to describe a given radiating struture. This form of the convergence of the analysis approach cannot be determined as fully because, like many computational electromagnetics techniques, this analysis is not convergent with respect to the number of sub-domain basis functions used in the analysis. This effect will be included in the sub-domain convergence discussion of Section 4.1.2.

4.1.1 Modal Convergence of the Solution

The convergence of the analysis approach discussed in Chapter 3 was examined by characterizing the input impedance of a strip dipole radiating element for several different numbers of Floquet modes. The strip dipole radiating element was chosen for this investigation of the convergence of the analysis approach because of the relative simplicity of this radiating element geometry. The geometry of this dipole array is shown

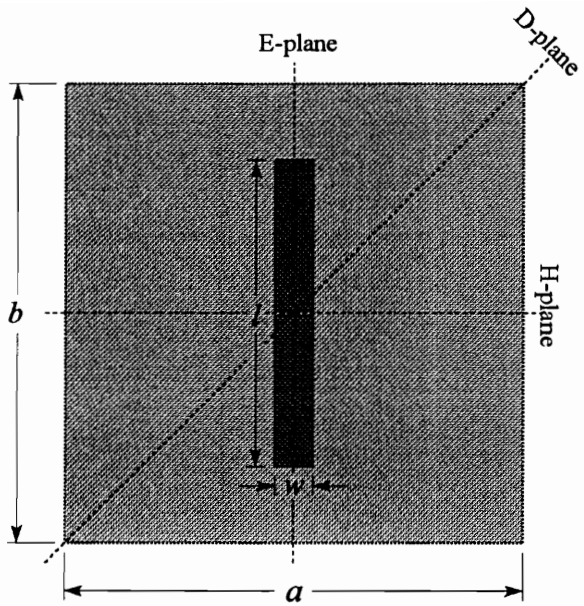

Figure 4.1. Geometry of the dipole antenna array cell used in the convergence and validation testing of the analysis algorithm presented in Chapter 3 This element cell is repeated infinitely many time in a square grid with spacings of a by b. The thickness of dielectric substrate is d.

in Figure 4.1. The analysis cell geometry shown in Figure 4.1 is used throughout Section 4.1 and Section 4.2 in the discussion of arrays of dipole radiating elements.

The parameters which describe the strip dipole and the Floquet analysis cell geometry are given in Table 4.1. The input impedance of the strip dipole radiating element was first computed for $N = 1$, 3, and 19 sub-domain basis element strip dipoles with the antenna array scanned to broadside. Figure 4.2 shows the magnitude and phase of the input impedance of the strip dipole for these analysis cases as a function of the number of Floquet modes used in the analysis. The magnitude of the input impedance for each strip dipole has been normalized by

$$|Z_{in_{norm}}| = \frac{|Z_{in}|}{|Z_{in}|\Big|_{P_9,Q_9}} \tag{4.1}$$

Table 4.1. Geometry description for the strip dipole radiating element used in the examination of the convergence of the Floquet mode based Method of Moments analysis approach. See Figure 4.1 for parameter definition.

Geometry Parameter		Value	Unit
analysis cell dimension	a	1.0	λ_o
	b	1.0	λ_o
	d	0.25	λ_o
dielectric substrate	ϵ_r'	1.000	n/a
	ϵ_r''	0.000	n/a
strip dipole dimension	l	0.3	λ_o
	w	0.02	λ_o

where $|Z_{in}|\Big|_{P_9,Q_9}$ is the input impedance magnitude computed for the same strip dipole for a number of Floquet modes given by

$$\begin{aligned} P_9 &= 9\,P_{Nyq} \\ Q_9 &= 9\,Q_{Nyq} \end{aligned} \tag{4.2}$$

where P_{Nyq} and Q_{Nyq} are the number of Floquet modes chosen to satisify Nyquist sampling in the x- and y-directions from (3.136). These results indicate that the analysis approach has substantially converged when enough modes are used to fulfill the Nyquist requirement as expected. These results also show that the convergence of the input impedance of a strip dipole composed of a single sub-domain basis function has essentially the same convergence behavior as strip dipoles composed of multiple sub-elements. This result was used to simplify the investigation of the effects of beamscanning on modal convergence.

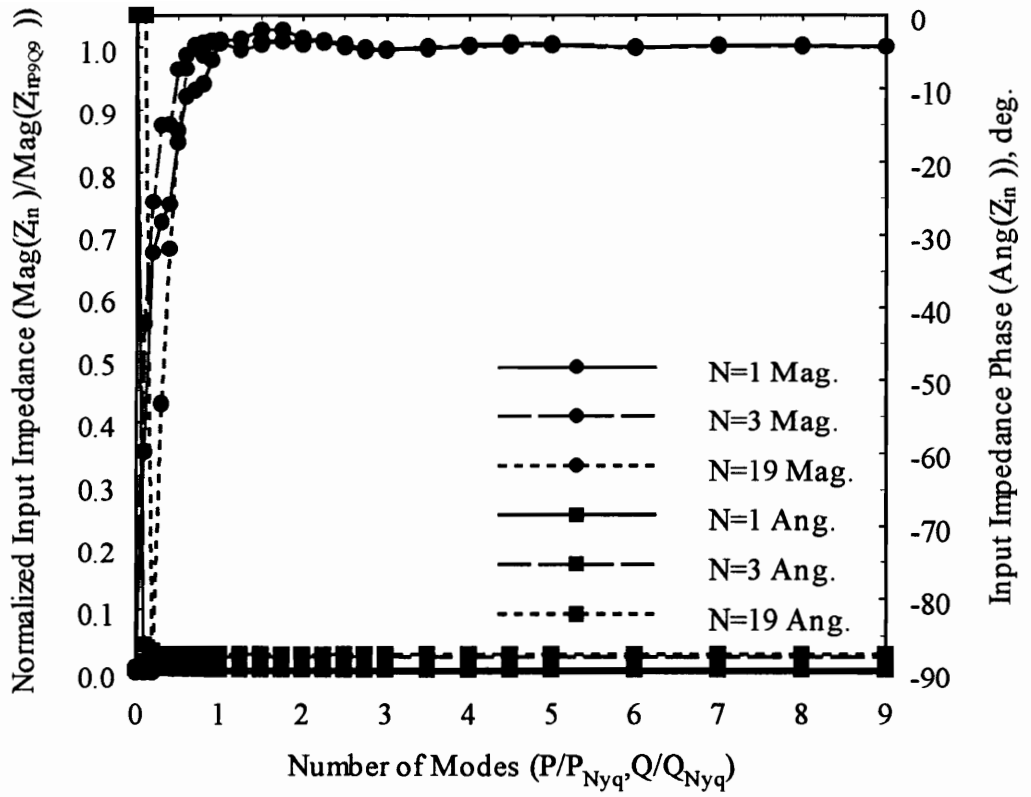

Figure 4.2. Normalized magnitude and phase of the input impedance of the three strip dipoles used in the modal convergence study at broadside.

The effect of beamscanning on the modal convergence of this analysis approach was investigated by characterizing the input impedance of a strip dipole described by a single sub-domain basis function as a function of the number of Floquet modes used in the analysis at three different angles of beam scanning. Figure 4.3 shows the normalized magnitude and phase of the input impedance of this radiating element as a function of the number of Floquet modes used in the analysis for three different angles of beamscanning. These results indicate that the modal convergence of this analysis approach is unaffected by the direction of beamscanning in the infinite antenna array.

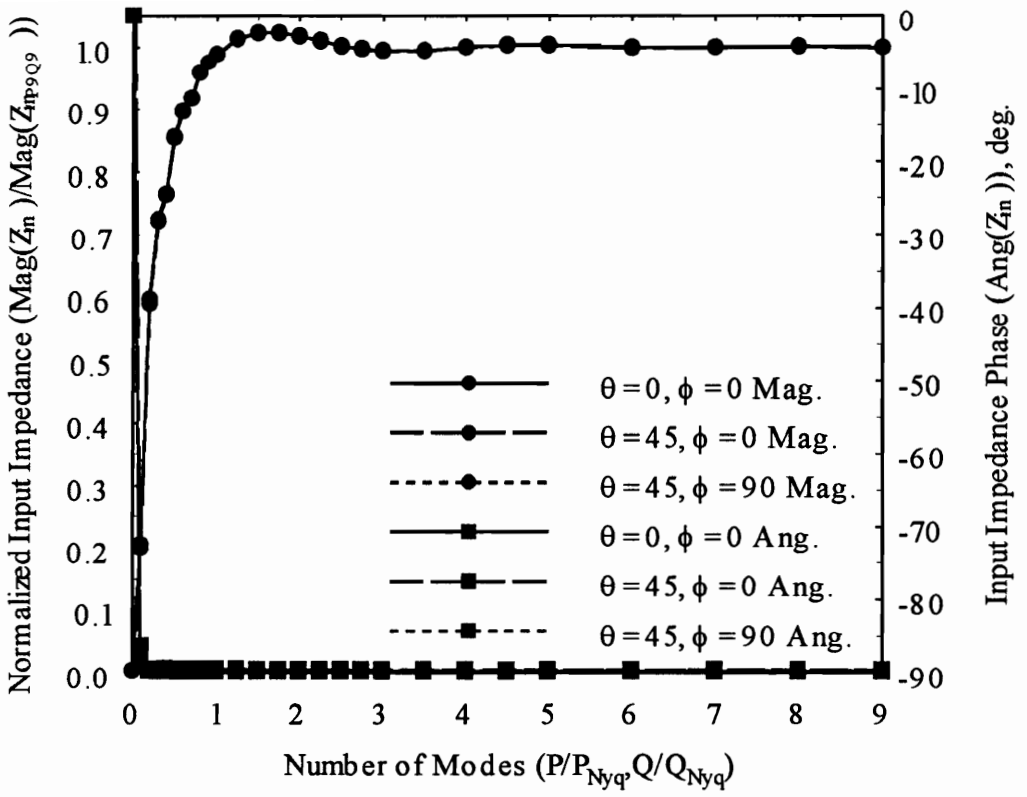

Figure 4.3. Normalized magnitude and phase of the input impedance of the single sub-domain basis function strip dipole used to study the convergence effects of beamscanning.

4.1.2 Sub-Domain Basis Function Convergence of the Solution

The second form of convergence for the analysis technique discussed in Chapter 3 is the convergence with increasing numbers of sub-domain elements in the description of the radiating element. Alternately, this form of convergence can be viewed as determining the maximum size of the sub-domain basis function elements used to model the radiating element. Computational electromagnetics techniques often impose a minimum size restriction on the sub-domain basis function elements as well. This limit is

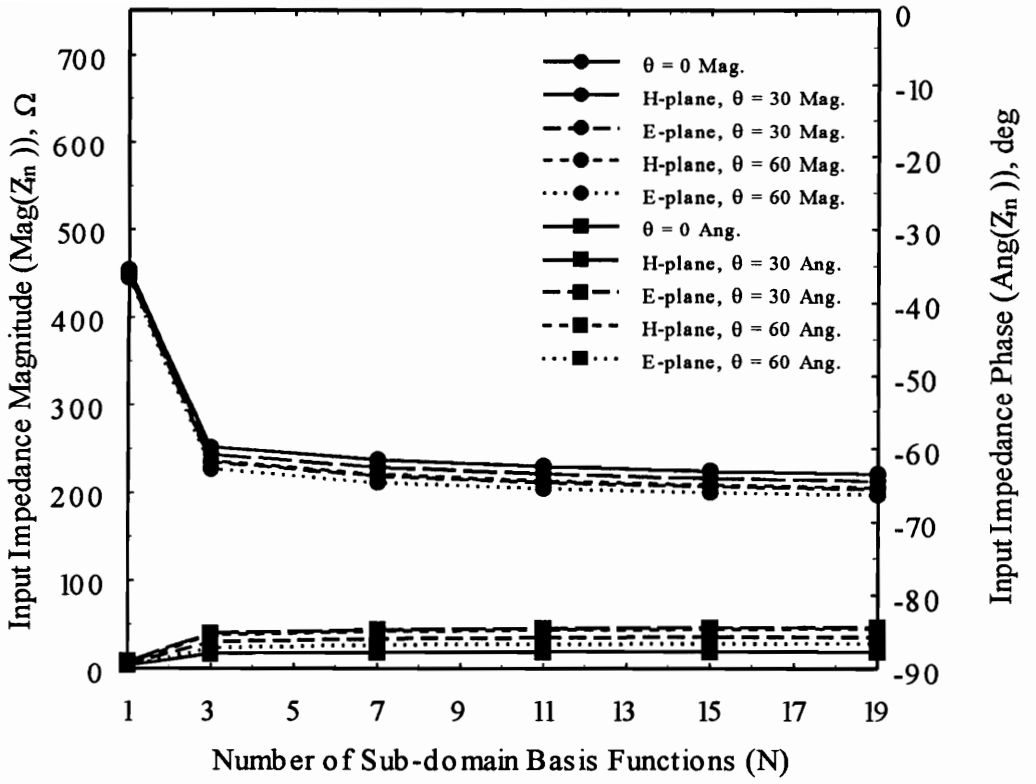

Figure 4.4. Magnitude and phase of the input impedance of the strip dipole radiating element used to determine the convergence of the analysis approach as a function of the number of sub-domain elements used in the radiating element description.

due to capacitive effects generated by the delta gap source model described in Section 3.7. These requirements usually combine to restrict the sub-domain elements to a range of allowable sizes.

The range of allowable sizes for the sub-domain elements in this analysis approach was investigated by examining the computed input impedance for the strip dipole geometry used in Section 4.1.1 as the number of sub-domain elements used in the description was varied. The analysis cell and strip dipole geometry used in this analysis is

given in Table 4.1. The input impedance was computed for this strip dipole for $N = 1, 3, 7, 11, 15$, and 19 sub-domain element descriptions. The number of Floquet modes used in this analysis was chosen so that

$$\begin{aligned} P &= 2\,P_{Nyq} \\ Q &= 2\,Q_{Nyq}, \end{aligned} \tag{4.3}$$

or double the number of modes chosen to satisfy the Nyquist criteria, to ensure essentially complete convergence as discussed in Section 4.1.1. The computed magnitude and phase of the input impedance computed for this strip dipole geometry are shown in Figure 4.4 as a function of the number of sub-elements used to describe the strip dipole. These results indicate that the allowable range of sub-domain element sizes begins at around $0.1\lambda_o$ overall sub-domain element length, $\overline{\overline{\rho_3\rho_4}}$, and extends down to at least $0.03\lambda_o$ overall sub-domain element length. No performance degradation due to source model capacitance is noticeable in these results.

4.2 Validation of the Analysis Approach

The validity of the analysis approach presented in Chapter 3 was examined by comparing computational results for the input impedance of two different analysis geometries using the ASIA code with published computational results for the same geometries. The radiating element in the infinite antenna array for each of these cases was a strip dipole. The first validation case examined was an array of these dipoles in a free-space environment. These results are discussed in Section 4.2.1. The second validation case examined was an infinite antenna array of strip dipole radiating elements printed on a dielectric support substrate backed by a PEC ground plane. The results of this investigation are discussed in Section 4.2.2.

4.2.1 Infinite Antenna Array of Dipole Radiating Elements in Free Space

The first analysis cell geometry used to validate the analysis approach presented in Chapter 3 was an infinite antenna array of infinitely thin, half-wavelength strip dipoles in a free-space environment. The input impedance for this geometry has been computed by Diamond [40] for this geometry. This geometry was modeled in ASIA by an infinite antenna array of $l = 0.4\lambda_o$ by $w = 0.02\lambda_o$ strip dipoles. The dipoles were shortened slightly to assure adequate spacing between adjacent radiating elements in the array grid. This spacing was not a concern in the grating lobe series approach used by Diamond in [40]. The free-space environment was modeled in ASIA by placing the PEC ground plane at $z = -10^6\lambda_o$ and using essentially an air dielectric with the addition of a slightly loss component. The addition of this loss effectively eliminates the wave component reflected from the ground plane which contributes to the standing wave in the dielectric region resulting in a near traveling wave electromagnetic field distribution in this region. The analysis cell and radiating element geometry for this validation case are shown in Table 4.2.

The computed input resistance for this dipole antenna array is shown in Figure 4.5 for H-, E-, and D-plane (diagonal between E- and H-) beamscanning as a function of the scan angle from broadside, θ_o, from both Diamond [40] and ASIA. These results show good overall agreement of the trends between these two results. The deviation between the exact levels of the corresponding curves is significant for the H-plane scan results only. The differences between the results of Diamond [40] and ASIA for this strip dipole antenna array geometry may be attributable to slight differences in the analysis geometries as well as the rather simpler grating lobe series analysis performed by Diamond. The overall good agreement between the trends of the input

Table 4.2. Geometry description for the strip dipole radiating element used in the first validation case for the Floquet mode based Method of Moments analysis approach. See Figure 4.1 for parameter definition

Geometry Parameter		Value	Unit
analysis cell dimension	a	0.5	λ_o
	b	0.5	λ_o
	d	10^6	λ_o
dielectric support	ϵ_r'	1.000	n/a
	ϵ_r''	-0.001	n/a
strip dipole dimension	l	0.4	λ_o
	w	0.02	λ_o

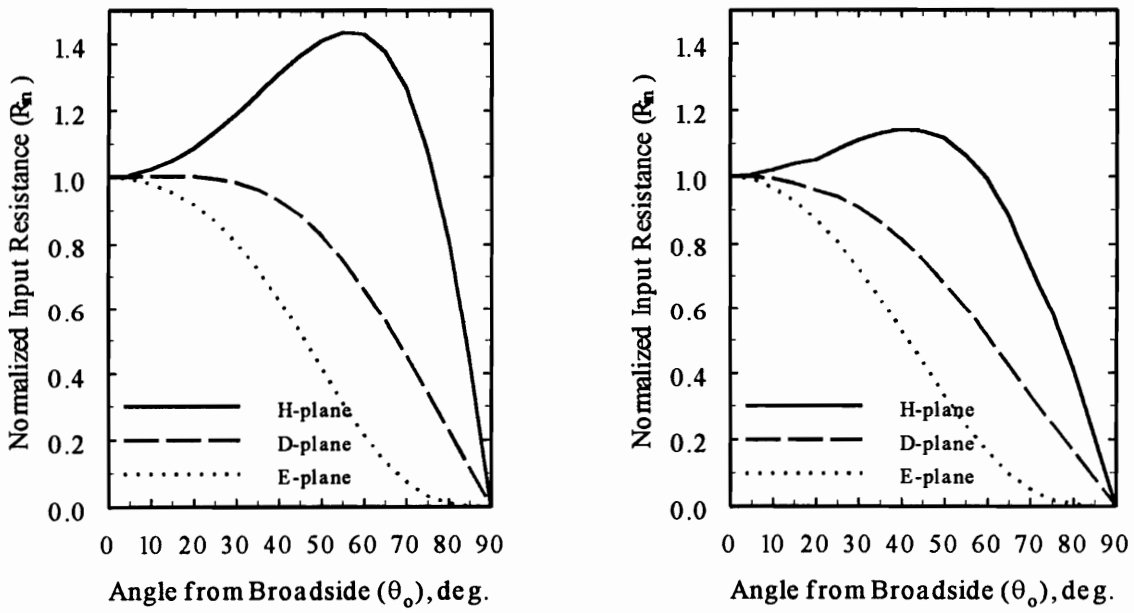

(a) ASIA (b) Diamond [40]

Figure 4.5. Normalized input resistance of an infinite antenna array of half-wave dipoles in a square half-wave array grid in a free-space environment computed using 19 unknowns in ASIA (a) and computed by Diamond (b) from [40].

resistance computed by these two analysis techniques suggests that the analysis algorithm presented in Chapter 3 and implemented in ASIA is reasonably accurate.

4.2.2 Infinite Antenna Array of Printed Dipole Radiating Elements

The second analysis geometry used to validate the analysis approach is an infinite antenna array of strip dipoles printed on a dielectric substrate backed by a PEC ground plane. The input reflection coefficient for this antenna array geometry has been calculated by Pozar [28]. This choice of geometry represents a typical large printed antenna array configuration. The analysis cell and radiating element geometry for this validation case are shown in Table 4.3. The computed input reflection coefficient for this strip dipole validation case is shown in Figure 4.6a for three different scan planes versus angle from broadside, θ_o. Figure 4.6b shows input reflection coefficient results for the

Table 4.3. Geometry description for the strip dipole radiating element used in the second validation case for the Floquet mode based Method of Moments analysis approach. See Figure 4.1 for parameter definition.

Geometry Parameter		Value	Unit
analysis cell dimension	a	0.5	λ_o
	b	0.5	λ_o
	d	0.19	λ_o
dielectric support	ϵ_r'	2.55	n/a
	ϵ_r''	-0.001	n/a
strip dipole dimension	l	0.39	λ_o
	w	0.002	λ_o

same radiating element from Pozar [28]. The extremely good agreement between the input reflection coefficient results shown in Figures 4.6a and 4.6b, including the scan blindness indicated at $\sim 45°$, suggests ASIA accurately predicts the input impedance of printed radiating elements in large phased antenna arrays.

The scan blindness which appears in the E-plane beamscanning results in Figure 4.6 is caused by the excitation of a surface wave in the dielectric support substrate. The excitation of a surface wave mode traps the majority of the power input to the radiating element in the dielectric substrate because the surface wave mode is evanescent in the air region of the analysis cell. From (2.27) and (2.28), the transcendental equation for the TM_o surface wave mode, the only surface wave mode which can be supported by this dielectric support substrate, is

$$k_z^{(d)} \sin\left(k_z^{(d)} d\right) - j\epsilon_r k_z^{(+)} \cos\left(k_z^{(d)} d\right) = 0 \tag{4.4}$$

where $k_z^{(+)}$ and $k_z^{(d)}$ are the z-directed wavenumbers in the air and dielectric regions of the analysis cell for the surface wave given by

$$\begin{aligned} k_z^{(+)} &= \sqrt{k_o^2 - \left|\overline{k}_\rho\right|^2} \\ k^{(d)} &= \sqrt{\epsilon_r k_o^2 - \left|\overline{k}_\rho\right|^2} \end{aligned} \tag{4.5}$$

where $\overline{k}_\rho$ is the wavenumber of the surface wave in the xy-plane. This transcendental equation is be found by satisfying the boundary conditions for the dielectric slab waveguide structure discussed in Section 2.1.2. Solving (4.4) shows that the transverse wavenumber required for the surface wave mode is

$$\left|\overline{k}_\rho\right| = 1.282\, k_o. \tag{4.6}$$

Since the surface wave is formed by the first Floquet mode which is outside visible space in the plane of beamscanning, the beam scanning angle for scan blindness caused by this

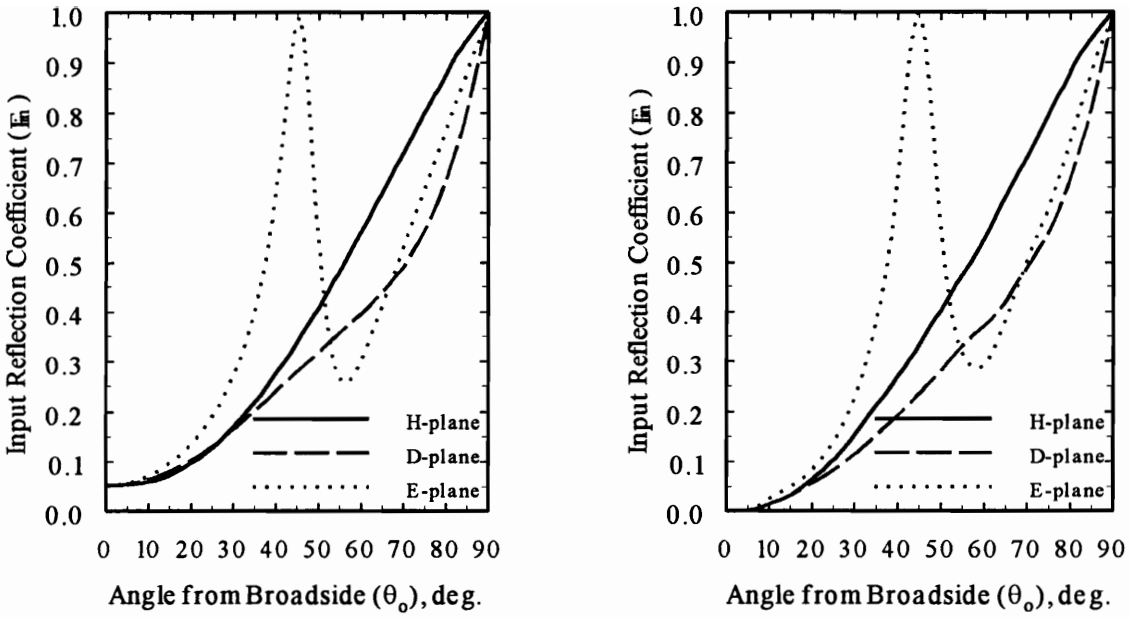

Figure 4.6. Input reflection coefficient of an infinite antenna array of printed strip dipole radiating elements computed using 19 sub-domain elements in ASIA (a) and by Pozar [28].

surface wave is given by

$$\theta_{sw} = \text{asin}\left(\frac{|\overline{k}_\rho|}{k_o} - \frac{\lambda_o}{cell}\right) \tag{4.7}$$

where *cell* is the dimension of the analysis cell in the plane of beamscanning, in this case. Equation (4.7) can be solved to give

$$\theta_{sw} = 45.85° \tag{4.8}$$

which compares very well with the computed direction of scan blindness in Figure 4.6. This suggests that the direction of scan blindness due to surface wave effects in printed antenna arrays with radiating element which are small compare to the analysis cell can be approximated by analysis of a dielectric slab waveguide structure.

4.3 Preliminary Analysis of a New Radiating Element [41]

The analysis approach presented in Chapter 3 is being used to investigate the scanning behavior of a new radiating element, the Foursquare antenna. The Foursquare radiating element is essentially an enhanced crossed-dipole antenna printed on a dielectric substrate. This radiating element was designed to provide dual-polarized radiation over an approximately 60% frequency bandwidth. The Foursquare element consists of four square patches fed in diagonal pairs. The gap, W, between the patches is the same between the patches both horizontally and vertically. This gives an overall length for the radiator, L, of twice the patch size plus the center gap width in both directions. The geometry of the Foursquare radiating element is shown in Figure 4.7.

The surface wave scan blindness directions were calculated for the Foursquare radiating element printed on a $d = 0.15\lambda_o$ dielectric support structure of $\epsilon_r = 2.55 - j0.001$ for several combinations of cell dimension and relative metallizations

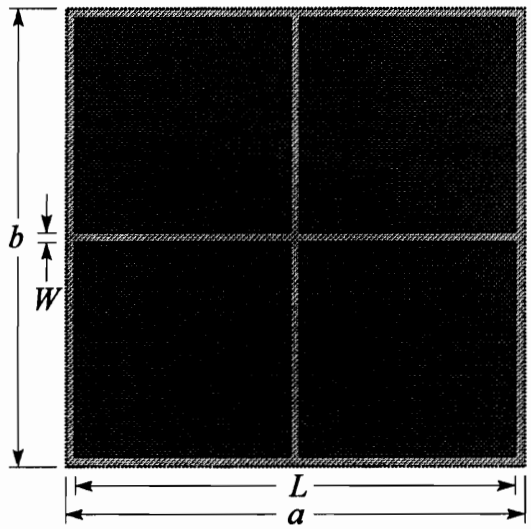

Figure 4.7. Geometry of the Foursquare radiating element showing the overall length of the element, L, and the width of the central gap, W.

of the analysis cell. The cell dimensions, a and b, were equal and varied between $0.45\lambda_o$ and $0.6\lambda_o$. The scan blindness direction for Foursquare element was computed for these cell dimensions for element sizes, relative to the analysis cell, of $\frac{L}{a} = \frac{L}{b} = 0.7$, 0.86, and 0.90. The scan blindness locations found in this preliminary characterization of the Foursquare radiating element are shown in Figure 4.8. Figure 4.8 also shows the scan blindness angles for radiating elements structures which are essentially based on parallel plate waveguide and dielectric slab waveguide structures. The scan blindness angle for the Foursquare radiating element departs the dielectric slab waveguide scan blindness curve in the direction of the parallel plate waveguide curve as the size of the radiating element increases relative to the analysis cell dimension. While this behavior is understandable when the largely metallized analysis cell of the Foursquare radiating element is considered, it is believed that this dependence has not been noted previously in the published literature.

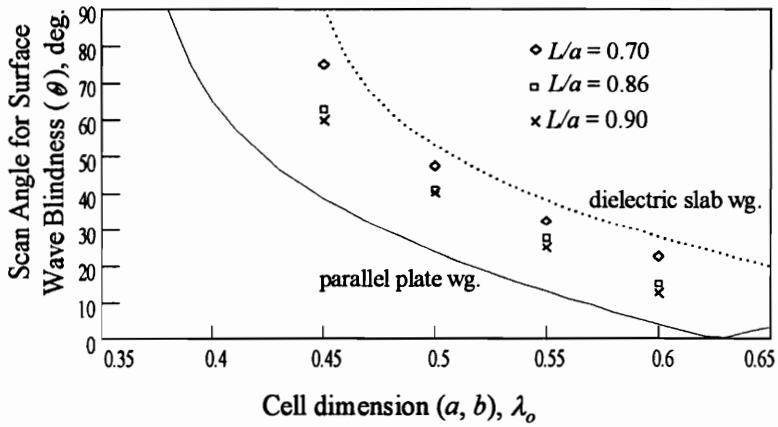

Figure 4.8. Surface wave locations for Foursquare radiating elements of different relative metallizations of the analysis cell. The solid line shows the scan blindness angle for a dielectric loaded parallel plate waveguide structure. The dotted line shows this information for a dielectric slab waveguide [41].

5. CONCLUSIONS

The development of a useful method for predicting the performance of large phased antenna arrays of complex radiating elements was the primary goal of the research which led to this document. As noted in Chapter 1, the prediction of the performance of these antennas is greatly complicated by the dominating presence of mutual coupling between the radiating elements. This complication makes ideal antenna array theory prediction of this performance effectively impossible. Current approaches to this performance prediction are limited in either the scope of allowable antenna array sizes and radiating element geometry or are not sufficiently general for non-research use.

A new approach to the characterization of complex radiating elements in large phased antenna arrays has been presented. This approach was specifically designed to address the limitations of the previous analysis techniques discussed in Chapter 2. This technique allows the analysis of a complex, arbitrarily shaped printed radiating element in a fully active infinite antenna array. The mathematical basis for this new infinite antenna array analysis approach was fully described in Chapter 3.

The characterization technique presented here has also been implemented as the computational electromagnetics code ASIA (Analysis Software for Infinite Arrays). This code has been successfully used to characterize many different radiating element geometries. These radiating element geometries include the dipole and printed dipole antennas used to validate the capability of the new characterization technique to accurately predict the performance of complex radiating elements in the fully active infinite antenna array environment. Preliminary results from the analysis of a more complex radiating element are also presented in Chapter 4. These results show a previously unreported

variation in the surface wave scan blindness direction which appears to be present for radiating elements which extend over large regions of the analysis cell. It is believed that this variation is caused by the structure changing from essentially a dielectric slab waveguide to a dielectric loaded parallel plate waveguide. While intuitively understandable, it is believed that this variation has not been previously reported in the literature.

Several paths for further development of this characterization approach for large antenna arrays are possible. The simplest enhancement of the analysis approach will be to allow multiple layered dielectrics in the support structure. This first step in this modification should be the revision of the coupling dyadic to include two layers of dielectric support between the radiating element and the ground plane and one radome dielectric layer above the radiating element. This enhancement will also allow the analysis of radiating elements printed on dielectric substrates without ground plane backing using the approach discussed in Section 4.2.1. Eventually, this modification should be able to support arbitrary multiple layered dielectrics with metallization at each dielectric interface as well as at the air/dielectric interface.

The addition of a probe feed model to the analysis algorithm would allow the performance of microstrip patch radiating elements to be characterized by this approach. This enhancement would also allow more inclusive analysis of most radiating elements since even balanced elements in a printed array are usually probe-fed. This addition to the analysis algorithm can be approached with either a lumped element probe model or a more accurate electromagnetics analysis of the probe structure. The latter of these approaches would be preferable but may require excessive computation in the analysis since the Floquet modes will no longer couple in a mode-wise sense at the horizontal interfaces in

the analysis cell. This difficulty stems from the need to allow at least one vertical interface in the dielectric region of the analysis cell to account for the electric current density on the probe structure.

Finally, it may be possible to combine these enhancements to create an analysis approach which allows the characterization of arbitrary radiating elements which do not lie solely in the plane of the infinite antenna array. Some progress towards the development of this type of computational electromagnetics code has been reported for a much less general wire based radiating element description but the research has apparently not continued as anticipated in the original paper [32]. This development can proceed by allowing sub-domain elements with finite thickness, connections between multiple layers of metallization, or sub-domain elements which are not parallel to the infinite antenna array grid. The development of an analysis algorithm which allows sub-domain elements which do not lie in the infinite antenna array grid would be preferable but the apparent discontinuation of the work mentioned above suggests this development course may be extremely difficult.

REFERENCES

[1] R.E. Collin, *Field Theory of Guided Waves*, IEEE Press, New York, NY, pp. 605-608, 1991.

[2] W. Wasylkiwskyj and W.K. Kahn, "Efficiency as a Measure of Size of a Phased-Array Antenna," *IEEE Transactions on Antennas and Propagation*, vol. AP-31, pp. 879-884, November 1973.

[3] M.D. Deshpande and M.C. Bailey, "Analysis of Finite Phased Arrays of Circular Microstrip Patches," *IEEE Transactions on Antennas and Propagation*, vol AP-37, pp. 1355-1360, November 1989.

[4] W.L. Stutzman and G.A. Thiele, *Antenna Theory and Design*, John Wiley and Sons, New York, NY, Chapter 3 "Arrays," pp. 154-160, 1981.

[5] A.A. Oliner and R.G. Malech, *Microwave Scanning Antennas*, R.C. Hansen, editor, Peninsula Publishing, Los Altos, CA, *Volume III Array Theory and Practice*, Chapter 3 "Mutual Coupling in Infinite Scanning Arrays," pp. 209-216, 1985.

[6] D.F. Kelley and W.L. Stutzman, "Array Antenna Pattern Modeling Methods That Include Mutual Coupling Effects," *IEEE Transactions on Antennas and Propagation*, vol. AP-41, pp.1625-1632, December 1993.

[7] A.K. Bhattacharyya, *Electromagnetic Fields in Multilayered Structures*, Artech House, Boston, MA, Chapter 5 "Analysis of Microstrip Antennas and Arrays," pp. 103-111, 1994.

[8] R.F. Harrington, *Time Harmonic Electromagnetic Fields*, McGraw-Hill, New York, NY, Chapter 4 "Plane Wave Functions," pp. 168-171, 1961.

[9] R.J. Mailloux, *Phased Array Antenna Handbook*, Artech House, Boston, MA, Chapter 6 "Summary of Element Pattern and Mutual Impedance Effects," pp. 343-345, 1994.

[10] D.M. Pozar and D.H. Schaubert, "Analysis of an Infinite Array of Rectangular Microstrip Patches with Idealized Probe Feeds," *IEEE Transactions on Antennas and Propagation*, vol. AP-32, pp. 1101-1107, October 1984.

[11] A.A. Oliner and R.G. Malech, *Microwave Scanning Antennas*, R.C. Hansen, editor, Peninsula Publishing, Los Altos, CA, *Volume III Array Theory and*

Practice, Chapter 3 "Mutual Coupling in Infinite Scanning Arrays," pp. 195-199, 1985.

[12] A.A. Oliner and R.G. Malech, *Microwave Scanning Antennas*, R.C. Hansen, editor, Peninsula Publishing, Los Altos, CA, *Volume III Array Theory and Practice*, Chapter 3 "Mutual Coupling in Infinite Scanning Arrays," pp. 247-256, 1985.

[13] G.J. Burke, *Numerical Electromagnetics Code - NEC4 Part I: User's Manual*, Lawrence Livermore National Laboratory, January 1992.

[14] E.H. Newman, *A User's Manual for the Electromagnetic Surface Patch Code: ESP Version IV*, ElectroScience Laboratory, The Ohio State University, August 1988.

[15] W.A. Johnson, D.R. Milton, and R.M. Sharpe, *Patch Code User's Manual*, Sandia Report SAND 87-2991, Sandia National Laboratories, May 1988.

[16] Personal communication with W.A. Davis, author.

[17] J.W. Rockway, J.C. Logan, D.W.S. Tam, and S.T. Li, *The MININEC System: Microcomputer Analysis of Wire Antennas*, Artech House, Boston, MA, 1988.

[18] Evaluation package provided to Virginia Tech by Zeland Software.

[19] SONNET Software, *User's Manual: version 3.0*, Liverpool, NY, June 1995.

[20] Communication between Antenna Laboratory and Boulder Microwave.

[21] R.F. Frazita, "Surface-Wave Behavior of a Phased Array Analyzed by the Grating-Lobe Series," *IEEE Transactions on Antennas and Propagation*, vol. AP-25, pp. 823-824, November 1967.

[22] G.F. Farrell and D.H. Kuhn, "Mutual Coupling in Infinite Planar Arrays of Rectangular Waveguide Horns," *IEEE Transactions on Antennas and Propagation*, vol. AP-16, pp. 405-414, July 1968.

[23] A.A. Oliner and R.G. Malech, *Microwave Scanning Antennas*, R.C. Hansen, editor, Peninsula Publishing, Los Altos, CA, *Volume III Array Theory and Practice*, Chapter 3 "Mutual Coupling in Infinite Scanning Arrays," pp. 322-333, 1985.

[24] B.A. Munk, R.G. Kouyoumjian, and L. Peters, "Reflection Properties of Periodic Surfaces of Loaded Dipoles," *IEEE Transactions on Antennas and Propagation*, vol. AP-19, pp. 612-617, September 1971.

[25] D.M. Pozar, "Performance of an infinite array of monopoles in a grounded dielectric slab," *IEE Proceedings*, vol. 137, part H, no. 2, pp. 117-120, April 1990.

[26] R.C. Hall and R. Mittra, " Scattering from a Periodic Array of Resistive Strips," *IEEE Transactions on Antennas and Propagation*, vol. AP-33, pp. 1009-1011, September 1985.

[27] F. Zavosh and J.T. Aberle, "Infinite Phased Arrays of Cavity-Backed Patches," *IEEE Transactions on Antennas and Propagation*, vol. AP-42, pp. 390-398, March 1994.

[28] D.M. Pozar and D.H. Schaubert, "Scan Blindness in Infinite Phased Arrays of Printed Dipoles," *IEEE Transactions on Antennas and Propagation*, vol. AP-32, pp. 602-610, June 1984.

[29] R. Chu, "Analysis of an Infinite Phased Array of Dipole Elements with RAM Coating on Ground Plane and Covered with Layered Radome," *IEEE Transactions on Antennas and Propagation*, vol. AP-39, pp. 164-176, February 1991.

[30] J.R. Bayard, "Analysis of Infinite Arrays of Microstrip-Fed Dipoles Printed on Protruding Dielectric Substrates and Covered with a Dielectric Radome," *IEEE Transactions on Antennas and Propagation*, vol. AP-42, pp. 82-89, January 1994.

[31] D.M. Pozar, "Analysis of an Infinite Phased Array of Aperture Coupled Microstrip Patches," *IEEE Transactions on Antennas and Propagation*, vol. AP-37, pp. 419-425, April 1989.

[32] H.K. Schuman, D.R. Pflug, and L.D. Thompson, "Infinite Planar Arrays of Arbitrarily Bent Thin Wire Radiators," *IEEE Transactions on Antennas and Propagation*, vol. AP-32, pp. 364-377, April 1984.

[33] W.L. Stutzman and G.A. Thiele, *Antenna Theory and Design*, John Wiley and Sons, New York, NY, Chapter 7 "Moment Methods," pp. 306-370, 1981.

[34] J. VanBladel, *Electromagnetic Fields*, McGraw Hill, New York, NY, Chapter 12 "Two-dimensional Electromagnetic Fields and Plane Boundaries," p. 402, 1964.

[35] A.W. Glisson, *On the Development of Numerical Techniques for Treating Arbitrarily Shaped Surfaces*, Doctoral Dissertation, University of Mississippi, pp. 210ff, June 1978.

[36] R.F. Harrington, *Time Harmonic Electromagnetic Fields*, McGraw-Hill, New York, NY, Chapter 8 "Microwave Networks," pp. 389-390, 1961.

[37] W.H. Press, B.P. Flannery, S.A. Teukolsky, and W.T. Vetterling, *Numerical Recipes (FORTRAN Version)*, Cambridge University Press, New York, NY, Chapter 2 "Solution of Linear Algebraic Equations," pp.31-38, 1989.

[38] D.M. Pozar, "The Active Element Pattern," *IEEE Transactions on Antennas and Propagation*, vol. AP-42, pp. 1176-1178, August 1994.

[39] J.W. LaPean, *Users guide for Analysis Software for Infinite Arrays (ASIA v2.03)*, SATCOM 96-2, Antenna Laboratory, Satellite Communications Group, Center Wireless Telecommunications, Bradley Department of Electrical Engineering, Virginia Polytechnic Institute and State University, 1996..

[40] A.A. Oliner and R.G. Malech, *Microwave Scanning Antennas*, R.C. Hansen, editor, Peninsula Publishing, Los Altos, CA, *Volume III Array Theory and Practice*, Chapter 3 "Mutual Coupling in Infinite Scanning Arrays," pp. 280, 1985.

[41] W.L. Stutzman, W.A. Davis, J.W. LaPean, R. Neally, G. Ricciardi, *A Study of Elements for Use in Wideband Array Antenna Systems: Phase 2 - Log-periodic Radiator Development*, SATCOM 96-1, Antenna Laboratory, Satellite Communications Group, Center Wireless Telecommunications, Bradley Department of Electrical Engineering, Virginia Polytechnic Institute and State University, 1996.

VITA

James William LaPean, Jr. was born in Norfolk, Virginia in 1966. He was admitted to the undergraduate program at Virginia Polytechnic Institute and State University in 1984 and received the Bachelor of Science degree in Electrical Engineering in May 1989. He then joined the graduate program at Virginia Polytechnic Institute and State University. He has been a member of the Satellite Communications Group and an advisee of Dr. Warren L. Stutzman since that time. A Master of Science degree in Electrical Engineering was awarded in December 1993 as a result of research into beamscanning in large Cassegrain reflector antenna systems. His previous research experience with the Satellite Communications Group has included planning and evaluation of earth-space communications links and earth-space propagation characterization as well as reflector antenna and phased antenna array system design, antenna synthesis, and electromagnetic analysis.